Study of CdTe/MgCdTe Double-Heterostructure Solar Cells and an Epitaxial Lift-Off Technology for Thin-Film and Tandem Applications

by

Jia Ding

A Dissertation Presented in Partial Fulfillment
of the Requirements for the Degree
Doctor of Philosophy

Approved November 2021 by the
Graduate Supervisory Committee:

Yong-Hang Zhang, Chair
Dragica Vasileska
Shane Johnson
Zachary Holman

ARIZONA STATE UNIVERSITY

December 2021

ABSTRACT

CdTe/MgCdTe double heterostructures (DHs) integrated with a heavily-doped a-Si:H layer as the hole contact was demonstrated a record open-circuit voltage (V_{OC}) of 1.11 V and an active-area efficiency of 20% in 2016. Despite this significant progress, some of the underlying device physics has not been fully understood. The first part of this dissertation reports a systematic study of the CdTe/MgCdTe DH devices.

The CdTe/MgCdTe DHs are grown on InSb(001) substrates. The vertical transport mechanisms across the CdTe and InSb heterovalent interface are investigated with N-CdTe/n-InSb and N-CdTe/p-InSb heterostructures. A transport model including tunneling through CdTe barrier and InSb interband transition is developed to explain the different temperature dependent current-voltage characteristics of these two heterostructures.

Different p-type layers are integrated with the CdTe/MgCdTe DHs to form solar cells with different V_{OC} values and efficiencies. The low V_{OC} of devices with ZnTe:Cu and ZnTe:As hole contacts is attributed to the low built-in voltage and reduced minority carrier lifetime in the CdTe absorber, respectively. The critical requirements for reaching high V_{OC} values are analyzed.

A novel epitaxial lift-off technology for monocrystalline CdTe is developed using a water-soluble and nearly lattice-matched MgTe sacrificial layer grown on InSb substrate. The freestanding CdTe/MgCdTe DH thin films obtained from the lift-off process show improved optical performance due to enhanced light extraction efficiency and photo-recycling effect. This technology enables the possible development of monocrystalline CdTe thin-film solar cells and 1.7/1.1-eV MgCdTe/Si or MgCdTe/Cu(InGa)Se_2 tandem solar cells. The monocrystalline CdTe thin-film solar cells and 1.7-eV MgCdTe DH solar

cells have been demonstrated with a power conversion efficiency of 9.8% and an active-area efficiency as high as 15.2%, respectively. Additionally, a study of the radiation effects on CdTe DHs under 68-MeV proton irradiation is performed and showed their superior radiation tolerance. All these findings indicate that the monocrystalline CdTe thin-film solar cells are reasonably expected to have low weight, high-efficiency and high power density, ideal for space applications.

Dedicated to my parents and my grandfather

ACKNOWLEDGEMENTS

I would like to thank my advisor Dr. Yong-Hang Zhang for his guidance and supervision over the last 5 years. I have benefited significantly from his knowledge in semiconductor physics and the rigorous way of thinking. I would like to thank Dr. Dragica Vasileska, Dr. Shane Johnson and Dr. Zachary Holman for their interest in my research and serving on my committee.

I am also thankful to many group alumni and current colleagues, Dr. Zhaoyu He and Dr. Jacob Becker for training me on device processing and characterizations, Dr. Cheng-Ying Tsai for the four years of collaboration, Dr. Calli Campbell and Dr. Stephen Schaefer for sample growth and proofreading this dissertation, Xin Qi, Zheng Ju, Nathan Rosenblatt, Tyler McCarthy and Allison McMinn for their supports in conducting experiments and proofreading, and many others who had provided help. I would like to thank Dr. Elizabeth Steenbergen and Dr. Preston Webster for the collaboration in the experimental study of radiation effects on CdTe solar cell materials and devices, Dr. Wyatt Metzger and Dr. Eric Colegrove from the national renewable energy laboratory for the supply of polycrystalline CdTe solar cells. I would like to thank Dr. Zachary Holman and his students, Dr. Zhengshan Yu, William Weigand and David Quispe for their help on device processing, and Dr. Stuart Bowden for the help on Suns-V_{OC} measurement.

Finally, I would like to express my deepest gratitude to my parents for their unconditional love and supports over the years, which help me get rid of negative emotions during my doctoral studies.

TABLE OF CONTENTS

Page

CHAPTER Page

LIST OF TABLES

Table Page

LIST OF FIGURES

Figure Page

Figure Page

Figure Page

Figure Page

Figure Page

Figure Page

Figure Page

Figure Page

CHAPTER 1

INTRODUCTION

1.1 Why Solar?

Global warming is happening, with the consequences of sea levels rising, loss of biodiversity and ocean acidification. To achieve carbon neutrality by mid-21st century is thus proposed to attack climate change, fix global environment and re-engineer economies. This target is also laid down in the Paris agreement signed by 195 countries. The United States, Japan and more than 110 countries have committed for carbon neutrality by 2050. China has pledged to get there before 2060.

The use of renewable energy is one of the most efficient ways to reduce the carbon footprint. Photovoltaics (PV), by converting solar energy into electricity, promises to have a prominent role in the ongoing energy transition, with a rapid growth in global cumulative PV capacity and lower levelized cost of energy (LCOE) than conventional fossil fuel generators throughout most of the world [1]. Fig. 1.1 shows the increasement of global annual and cumulative PV installation capacity in the last 10 years [2]. The PV technology would play bigger and bigger impacts for the entire world.

PV also plays a very critical role in the space applications. Space assets have electronics ICs as its brain, photodetectors and other sensors as its eyes and ears, and LEDs and lasers as its nerves systems and arms for communication and direct energy delivery. All these are powered by solar energy generated by solar cells. The development of low weight, high power-density and radiation-robust solar cells would help to reduce launching cost and enable the exploration of the universe.

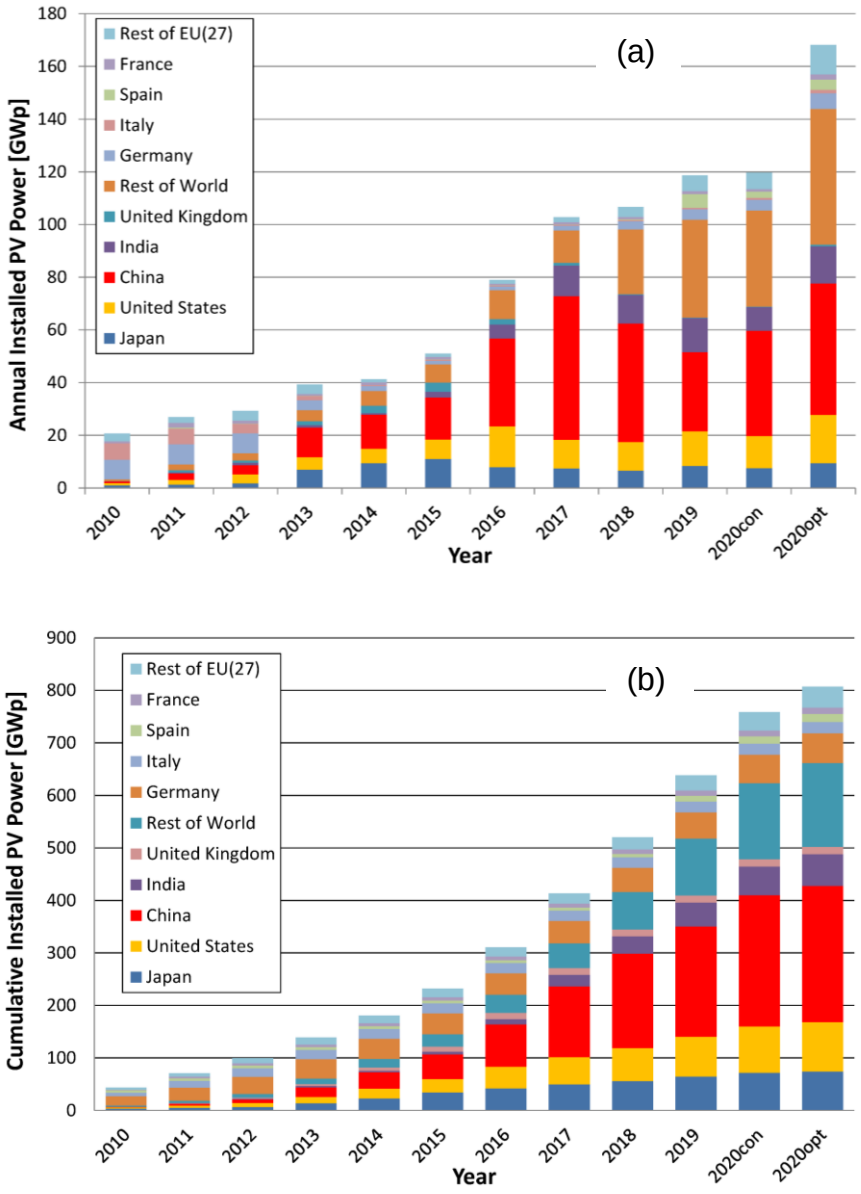

Figure 1.1 (a) Annual PV installations and (b) Cumulative PV installations from 2010 to 2020 all around the world [2].

1.2 CdTe/MgCdTe Double Heterostructures

CdTe is a good candidate for solar cell applications since it has a near optimum, 1.5-eV bandgap and a high absorption coefficient near the band edge. The CdTe/MgCdTe double heterostructure (DH) design is originally inspired by GaAs/AlGaAs DHs, which demonstrated very low interface recombination velocities and near-unity internal quantum efficiencies [3–5]. The interface recombination velocity of a high quality GaAs/$Al_{0.5}Ga_{0.5}As$ interface has been demonstrated to be as low as 18 cm/s [6], whereas the surface recombination velocity of a GaAs free surface is on the order of 10^7 cm/s [7]. Following the similar idea, since MgTe is relatively close lattice-matched to CdTe and InSb, and has a much wider band gap than CdTe with type-I band alignment [8], MgCdTe barrier is promising to provide sufficient carrier confinement and consequent low interface recombination for CdTe. Due to the high cost and small size of CdTe substrates, InSb(001) substrates are chosen because they are less expensive and have lower defect density, in comparison with CdTe substrates. Additionally, the surface oxide layer on the InSb substrates can be easily removed in a III-V MBE growth chamber. Therefore,

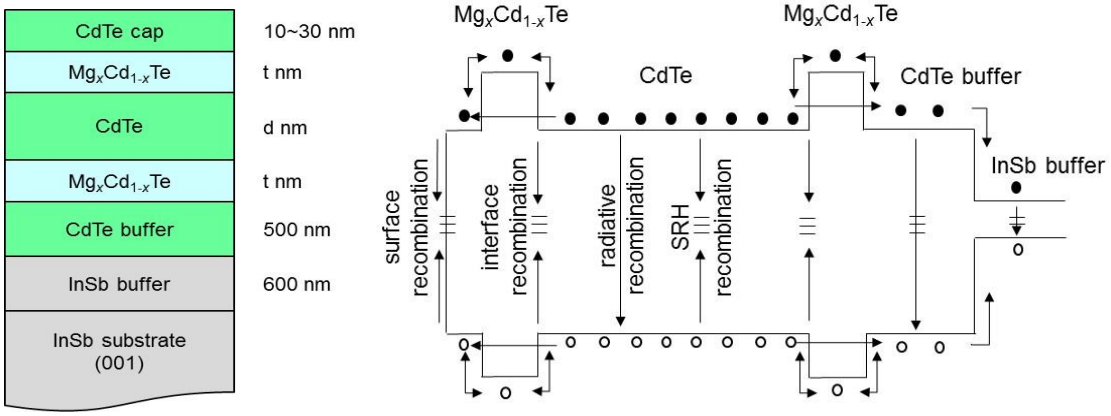

Figure 1.2 Sample structure and schematic band alignment for CdTe/MgCdTe double heterostructures. The solid and open circles represent excess electrons and holes respectively under illumination. Different recombination processes are also shown.

CdTe/MgCdTe DHs with tunable MgCdTe barrier heights are grown on InSb substrates for solar cell studies. The sample structure and schematic band alignment of CdTe DHs are shown in Fig. 1.2. Different recombination processes are also listed.

1.2.1 MBE Growth on InSb Substrate

The CdTe/MgCdTe DH samples are grown by using a dual-chamber VG V80H molecular beam epitaxy (MBE) system equipped with two separate III-V and II-VI growth chambers and an ultrahigh vacuum (UHV) transfer chamber as shown in Fig. 1.2. After growing InSb buffer layers on InSb substrates in the III-V growth chamber, samples are then transferred to the II-VI growth chamber to grow CdTe DHs. More detailed growth parameters can be found in previous publication [9].

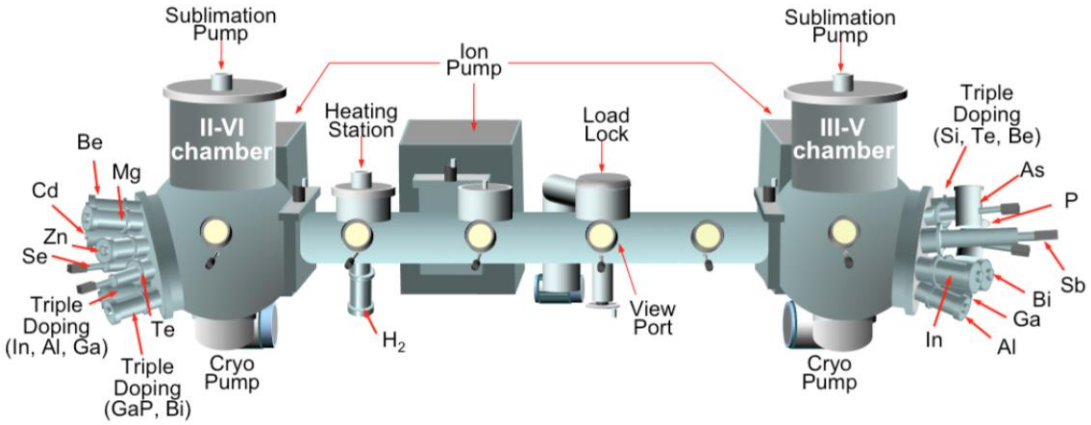

Figure 1.3 The lay-out of the dual chamber MBE system. The III-V and II-VI chambers are connected by a preparation chamber, allowing samples to be transferred under ultra-high vacuum.

M. DiNezza *et al.* demonstrated a CdTe/MgCdTe DH grown on an InSb substrate featuring a 1-µm-thick CdTe absorber sandwiched by two 30-nm-thick $Mg_{0.18}Cd_{0.82}Te$ barriers, and an undoped 1.57-µm-thick CdTe single layer grown on InSb. Room-temperature steady-state photoluminescence (PL) was conducted to characterize the optical

performance of the two CdTe samples. The CdTe DH sample exhibited over three orders of magnitude higher PL intensity compared with the CdTe bulk sample under the same excitation density. This comparison shows that the MgCdTe barriers provide successful carrier confinement and effectively reduce both surface recombination and transport of photogenerated carriers to the narrow gap (0.17 eV) InSb buffer layer.

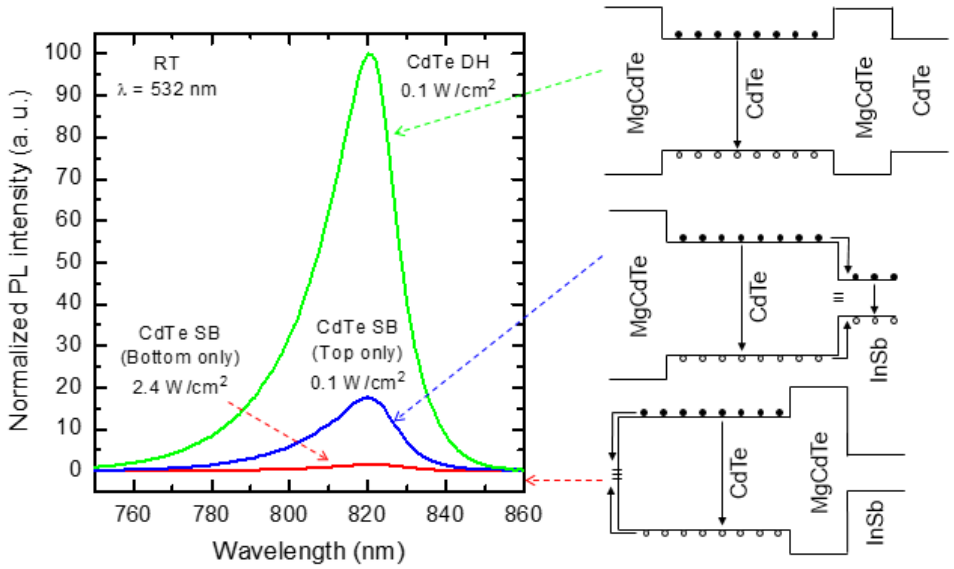

Figure 1.4 Comparison of photoluminescence spectra for the CdTe/MgCdTe double and single heterostructure samples, along with their schematic band edge diagrams showing the various recombination mechanisms [10].

M. DiNezza *et al.* designed another experiment to further demonstrate the effectiveness of MgCdTe barrier in confining carriers [10]. The result is shown in Fig. 1.4. All three samples, consist of a CdTe DH, and two single heterostructures, feature 30-nm-thick $Mg_{0.24}Cd_{0.76}Te$ barrier and a 1-μm-thick CdTe absorber. A 532 nm laser was used and the penetration depth in CdTe is 0.13 μm. The PL characterization showed that removing the bottom barrier reduces the PL intensity by a factor of 5, indicating that a significant number of carriers diffuse to the InSb layer and recombine non-radiatively or emit infrared light. Even more dramatic is the 3 order of magnitude reduction in PL

intensity for the sample without the top barrier. It can therefore be concluded that CdTe free surface recombination is the dominant mechanism when no top barrier exists. These results showed effectiveness of MgCdTe barrier layers to confine carriers and the importance of the top barrier to significantly suppress surface or interface recombination.

1.2.2 Interface Recombination Velocity

To quantitatively evaluate the interface recombination velocity (IRV) of the CdTe DHs, X.-H. Zhao, L. Shi *et al.* designed a series of DH samples with varied CdTe absorber thickness, top MgCdTe barrier thickness and Mg composition. The sample structures and different recombination mechanisms are shown in Fig. 1.2. The effective minority carrier lifetime τ_{eff} for a CdTe/MgCdTe DH can be expressed as [11]:

$$\frac{1}{\tau_{eff}} = \frac{1}{\tau_{rad}} + \frac{1}{\tau_{nr}} = \frac{1}{\tau_{rad}} + \frac{1}{\tau_{SRH}} + \frac{2S_{eff}}{d} \tag{1.1}$$

assuming low-injection situation where Auger recombination is negligible and the excess carriers distribute uniformly in CdTe absorber due to the long diffusion length of minority carriers. Here, τ_{rad} is radiative recombination lifetime, τ_{nr} is non-radiative recombination lifetime, τ_{SRH} is Shockley-Read-Hall (SRH) recombination lifetime, S_{eff} is CdTe DH effective interface recombination velocity, and d is the CdTe absorber thickness. The effective interface recombination includes the recombination happens at the interface between CdTe absorber and top MgCdTe barrier, the CdTe/InSb interface and the CdTe free surface. The latter two processes are due to the carriers that overcome the barriers through thermionic emission or tunneling. The radiative recombination lifetime τ_{rad} can be calculated as [12]:

$$\tau_{rad} = \frac{1}{(1-\gamma)Bn} \tag{1.2}$$

where B is the radiative recombination coefficient, n is the carrier concentration including background doping and excess carrier concentration, and γ is the photon recycling factor defined as the percentage of photons created by radiative recombination that are reabsorbed within the sample [13]. Since the photon recycling factor depends on the thickness and absorption coefficients of the absorber, in order to extract the effective interface recombination velocity S_{eff} more accurately, radiative lifetime has to be estimated and subtracted from the effective lifetime as:

$$\frac{1}{\tau_{nr}} = \frac{1}{\tau_{eff}} - (1-\gamma)Bn = \frac{1}{\tau_{SRH}} + \frac{2S_{eff}}{d} \tag{1.3}$$

Since the τ_{SRH} is absorber-thickness-independent, the S_{eff} can be determined by a linear fitting of $\frac{1}{\tau_{nr}}$ versus $\frac{2}{d}$. The γ can be calculated by using ray-tracing method [14] and B was determined previously from excitation-intensity-dependent PL measurements [15]. Carrier concentration was assumed to be 10^{14} ~ 10^{15} cm^{-3} range based on the capacitance-voltage measurements [16].

Table 1.1 shows the measured effective carrier lifetime and extracted IRV for all CdTe/$Mg_xCd_{1-x}Te$ DH samples studied [17]. For each set of samples, the effective carrier lifetime increases as a function of the thickness of the CdTe absorber, which implies a reduced equivalent interface recombination as the CdTe layer gets thicker. For the samples with sufficient MgCdTe barrier thickness (≥ 20 nm), the effective IRV increases significantly with lower Mg composition barriers, indicating the dominating carrier loss mechanism is attributed to thermionic emission of excess carriers over MgCdTe barriers. For samples with thinner barriers (15 nm), but still with high Mg composition (46%), the effective IRV is mainly attributed to the excess carriers tunneling through the barrier layers. When both thermionic emission and tunneling effects are suppressed, an ultralow effective

IRV of ~1 cm/s was measured at the CdTe/MgCdTe heterointerface. Such a low IRV indicates that the interface quality between CdTe and MgCdTe is close to perfection.

Table 1.1 Measured carrier lifetime of CdTe/$Mg_xCd_{1-x}Te$ double heterostructures with different designs. The effective interface recombination velocity (S_{eff}) is extracted according to Eq. (1.3) [17].

$Mg_xCd_{1-x}Te$ Barrier	Sample #	d (μm)	τ_{eff} (μs)	S_{eff} (cm/s)
t = 30 nm, 24% Mg	1	0.3	0.031	470±40
	2	0.5	0.042	
	3	1	0.086	
	4	2	0.18	
t = 30 nm, 36% Mg	5	0.2	0.24	54±32
	6	0.33	0.28	
	7	0.5	1.1	
t = 30 nm, 46% Mg	8	0.2	2.2	1.4±0.6
	9	0.25	2.2	
	10	0.33	2.8	
	11	0.5	3.6	
t = 22 nm, 46% Mg	12	0.2	2.0	1.2±0.7
	13	0.25	2.2	
	14	0.33	2.8	
	15	0.5	3.0	
t = 15 nm, 46% Mg	16	0.2	0.18	30±10
	17	0.25	0.31	
	18	0.33	0.47	
	19	0.5	0.83	
	20	1	0.75	
t = 20 nm, 36% Mg	21	0.25	0.15	61±14
	22	0.33	0.18	
	23	0.5	0.30	
	24	1	0.40	

1.2.3 Doping in CdTe Absorber

For CdTe solar cells, highly doped CdTe absorber is preferred to achieve a high built-in voltage (V_{bi}) and open-circuit voltage (V_{OC}). It has been found that p-type doped CdTe is hard to achieve. However, various studies have shown the possibility of efficient n-type

doping in CdTe by using In, grown by MBE [18–20]. Therefore, CdTe/MgCdTe DHs doped with In were demonstrated for solar cell studies.

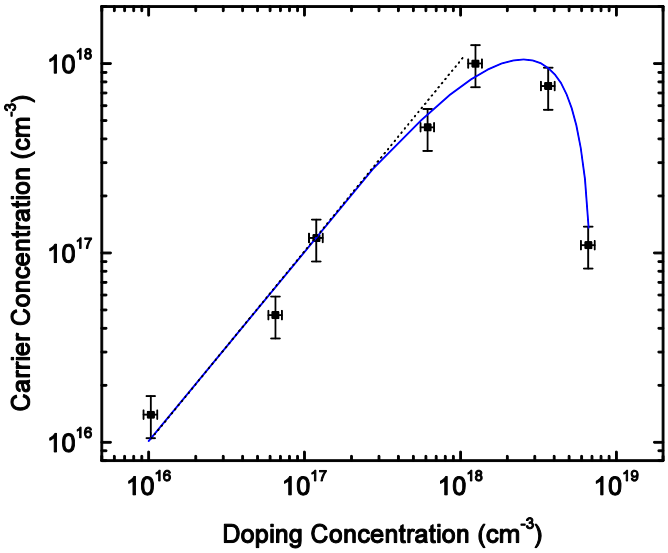

Figure 1.5 Carrier concentration versus In doping concentration in the CdTe layer [16]. The doping concentration and carrier concentration are determined by Secondary Ion-Mass Spectroscopy (SIMS) and Capacitance-Voltage (CV) measurements, respectively.

The doping vs. carrier concentrations was first studied. The carrier concentration in a semiconductor may not be necessarily equal to the doping concentration, as the dopants can be compensated by the other type of dopants or defects. Secondary Ion-Mass Spectroscopy (SIMS) and Capacitance-Voltage (CV) measurements were used to determine the doping and carrier concentrations, respectively. More experimental details can be found in the previous publication [16]. The Fig. 1.5 shows the relationship of carrier concentration vs. In doping concentration in the CdTe absorber. For the samples with In doping concentrations from 1×10^{16} to 1×10^{18} cm^{-3}, the carrier concentration is almost the same as the doping concentration, indicating the nearly 100% ionization at the room temperature. For the samples with the doping concentration higher than 1×10^{18} cm^{-3}, the carrier concentration deviates the linear relationship with doping concentration and then

reduces dramatically. This behavior indicates strong compensation in the CdTe absorber at higher doping levels. It was mentioned that Cd over pressure during the CdTe layer growth is favorable for the activation of In dopants, since it prevents the formation of Cd vacancies (p-type) when In is present [21]. Based on our observation, it is possible that below1×1018 cm−3 doping level, Cd/Te flux ratio of 1.5 is enough for the effective activation of In; however, beyond that doping level, higher Cd/Te flux ratio may be needed.

The optical properties of the CdTe/MgCdTe DHs were also studied with different In doping concentrations. Room temperature steady-state PL (SSPL) and time-solved PL (TRPL) measurements were conducted on In-doped CdTe/$Mg_{0.46}Cd_{0.54}Te$ DHs with different doping concentrations. Fig. 1.6 summaries the minority carrier lifetimes extracted from TRPL and SSPL peak intensities as a function of carrier concentrations.

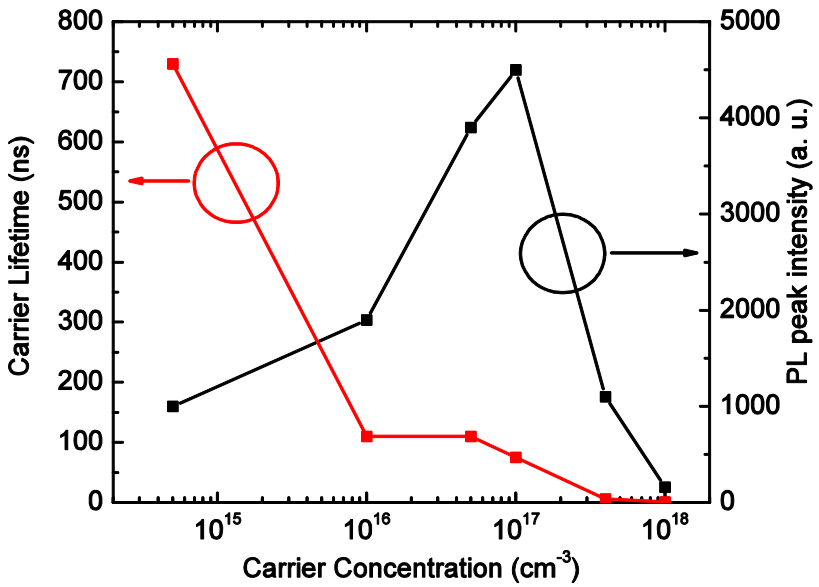

Figure 1.6 Carrier lifetime and PL peak intensity of CdTe/$Mg_{0.46}Cd_{0.54}Te$ DHs versus carrier concentration in CdTe layer [16].

As shown in equation (1.1) and (1.2), the radiative recombination lifetime would decrease with the increased carrier concentration, leading to a decreased effective carrier

lifetime. When the PL excitation is fixed, the PL intensity is proportional to the internal quantum efficiency (IQE), which is defined as the ratio of the radiative recombination rate (R_{rad}) to the total recombination rate (R_{total}) inside CdTe, as shown in equation (1.4).

$$\eta_{int} = \frac{R_{rad}}{R_{total}} = \frac{R_{rad}}{R_{rad}+R_{non-rad}} = \frac{R_{rad}}{R_{rad}+R_{SRH,b}+R_{interface}} \quad (1.4)$$

Besides the radiative recombination, the bulk SRH recombination is related to the quality of CdTe. The interface recombination is not only related to the interface quality but to the band bending at the CdTe/$Mg_{0.46}Cd_{0.54}Te$ interface region as well. With higher n-type doping concentrations, the band bending is stronger at the interface, and it is possible that the minority carrier (hole) is driven away from the interface resulting reduced effective interface recombination.

When the doping concentration is below 1×10^{17} cm^{-3}, the PL intensity increases with the carrier concentration, indicating the ratio of the radiative recombination rate and the non-radiative recombination rates increases. When the doping concentration is above 1×10^{17} cm^{-3}, non-radiative recombination rate starts to increase faster than the radiative recombination rate. Thus a weaker PL intensity is observed at higher doping concentrations. The dramatic increase in non-radiative recombination may be due to the formation of In-related deep defect states located near the middle of the bandgap. The relative constant carrier lifetime in the doping range of 1×10^{16} cm^{-3} ~ 1×10^{17} cm^{-3}, is probably due to the reason that interface recombination may have decreased with stronger band bending, which offsets the effect of increasing bulk SRH and radiative recombination processes.

The optical performance of these CdTe DH samples can be further quantitatively evaluated by photoluminescence quantum efficiency (PLQE) measurements. Considering the complementary physical action of solar cells and light emitting diodes (LEDs), the

transformation of electrical energy into light and transformation of radiation energy into electricity, a reciprocity relation between PLQE and electroluminescent emission of solar cells can be connected based on detailed balance theory as [22,23]:

$$iV_{OC} = V_{OC-ideal} - \frac{kT}{q} \ln(|\eta_{ext}|) \quad (1.5)$$

where iV_{OC} is the implied open-circuit voltage of a solar cell, or the quasi-fermi-level splitting in the absorber, $V_{OC-ideal}$ is the detailed-balance open-circuit voltage (V_{OC}) when only radiative recombination exists, η_{ext} is the PLQE measured from the front surface since the reciprocal action, light absorption, only happens at the front surface for the solar cells we discussed in this dissertation.

The PLQE measurement setup is shown in Fig. 1.7. By using a Spectralon Lambertian

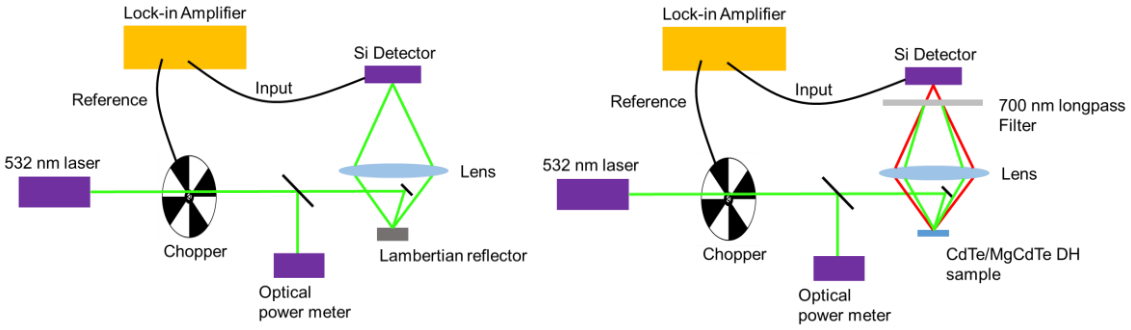

Figure 1.7 Photoluminescence Quantum Efficiency measurement setup [24]. (left) shows the measurement of a Lambertian reflector with calibrated reflectance. (right) shows the measurement of a CdTe/MgCdTe DH sample.

reflector with calibrated reflectance as a reference, the PL from the CdTe DH samples at exactly the same position can be quantitatively calculated. More details about the setup and measurement procedure can be found in the previous publication [24]. The measurement results are summarized in Table 1.2. The In doping concentration of 1×10^{17} cm^{-3} gave the highest iV_{OC} of 1.13 V under one-sun condition, which also indicates the promising

applications in high efficiency solar cells. Such a high iV_{OC} is due to the ultralow effective interface recombination velocity and the optimized trade-off of high doping concentration and relatively low bulk SRH recombination rate.

1.2.4 "Remote Junction" CdTe DH solar cells

Table 1.2 Measured minority carrier lifetime, photoluminescence quantum efficiency and calculated implied V_{OC} for CdTe/$Mg_{0.46}Cd_{0.54}Te$ DHs with different doping concentrations [24].

CdTe Absorber Doping Concentration (cm^{-3})	τ_{eff} (ns)	η_{ext} (%) at 1 sun	iV_{OC} (V)
Unintentionally doped	730	0.68	1.09
1×10^{16}	110	1.2	1.11
6×10^{16}	110	2.3	1.12
1×10^{17}	75	3.1	1.13
6×10^{17}	6	0.65	1.09
1×10^{18}	7	0.10	1.04

Based on the CdTe/MgCdTe DHs with ultralow IRV and high iV_{OC}, a "remote junction" concept has been proposed and used to demonstrate CdTe/MgCdTe DH solar cells with record high V_{OC} [25,26]. The basic idea of the remote junction design is shown in Fig. 1.8, in which unintentionally-doped intrinsic and n-type MgCdTe layers are used as the barriers for holes and electrons, and p-type a-Si:H is used as hole contact layer respectively. The intrinsic MgCdTe barrier prevents electrons to reach the pn junction and the defective p-region so that nonradiative recombination at the interface and in the bulk is substantially reduced. Since the quality of "remote" hole contact layers and the interfaces between hole contacts and the MgCdTe barrier layers make little impact on the performance of the solar

cells, such a “remote junction” structure offers an opportunity to use heavily-doped hole contacts on the CdTe devices to improve the built-in voltage (V_{bi}) while simultaneously maintaining the long minority carrier lifetime in the absorber.

Based on this concept, a CdTe/MgCdTe DH solar cell with an a-Si:H hole contact was demonstrated with V_{OC} over 1 V and efficiency of 17% [25]. The sample structure is shown in Fig. 1.9 (a). The 1.4-μm-thick absorber is In-doped with concentration of 1×10^{16} cm^{-3} for the top 1 μm and 5×10^{17} cm^{-3} for the bottom 0.4 μm. The solar cell structure was further optimized, as shown in Fig. 1.9 (b), with a thicker and higher i-MgCdTe barrier and an extra SiO_x anti-reflection coating (ARC) layer. The design and optimization of ARC is discussed in W.-Q. Yang’s paper [27]. The optimized CdTe DH solar cell achieved a V_{OC} of 1.1 V and an active-area efficiency of 20.3% measured under AM1.5G illumination [26]. More details about device mesa design and design logic can be found in J. J. Becker’s dissertation [28].

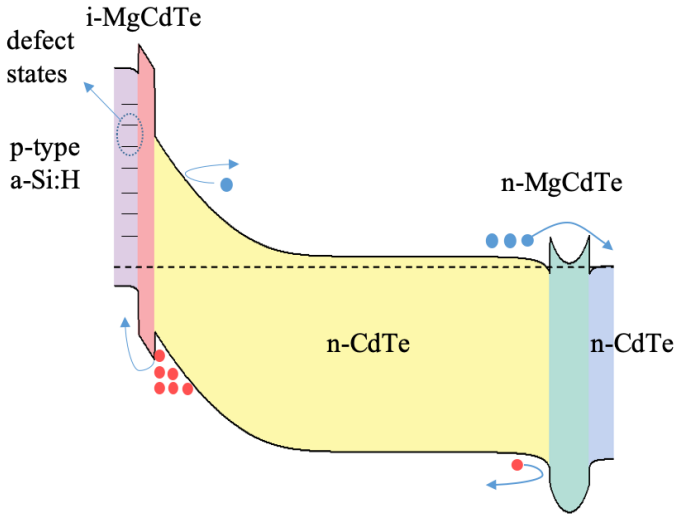

Figure 1.8 Band diagram of “remote junction” design [25], which is CdTe/MgCdTe DH solar cell with a p-type hole contact.

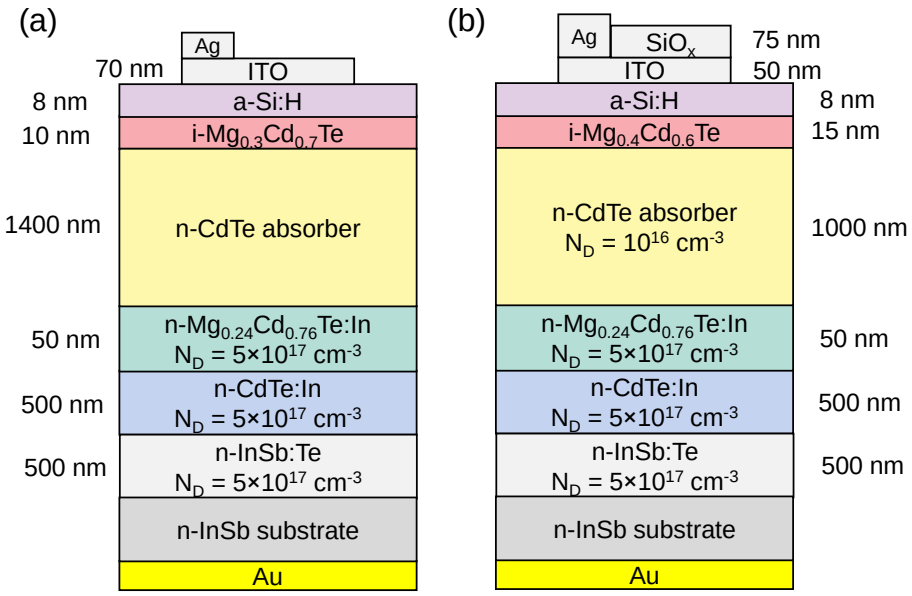

Figure 1.9 (a) Layer structure of CdTe/MgCdTe DH solar cells with V_{OC} over 1 V and efficiency of 17% [25]. (b) Optimized layer structure of CdTe DH solar cells with V_{OC} of up to 1.11 V and efficiency of 20.3% [26].

Based on the previous studies [17,25,26], thicker and higher Mg composition of i-MgCdTe layer would suppress the tunneling and thermionic emission of electrons, reduce the a-Si/i-MgCdTe interface recombination velocity and finally increase the V_{OC} of the solar cells. However, there's a trade-off of carrier transport and carrier confinement for the i-MgCdTe layer. The increased Mg composition in i-MgCdTe layer would also increase the valence band offset between i-MgCdTe and CdTe absorber, which would block the hole transport through thermionic emission and reduce the fill factor (FF) of the solar cells.

1.3 Organization of the Dissertation

This dissertation contains two parts. The first part is the systematic study of the monocrystalline CdTe DH solar cells, as discussed in Chapter 1 – 3.

Chapter 1 reviews the previous studies of CdTe/MgCdTe DHs and the "remote junction" design for CdTe DH solar cells. Some of the mentioned characterization method, formulas and conclusions will be directly used in the following chapters.

Chapter 2 studies the vertical carrier transport across CdTe and InSb heterovalent interface. The N-CdTe/n-InSb heterojunction is the electron contact of the CdTe DH solar cells. Understanding the transport mechanisms of the electron contact promises the good electrical performance of the CdTe devices grown on InSb substrates.

Chapter 3 gives an explanation that why different hole contacts led different values of V_{OC} and efficiencies based on the "remote junction" solar cell structure. This chapter also gives a guide to the selection of hole contacts for CdTe DHs.

The second part of this dissertation is the thin-film and tandem applications of the CdTe DHs based on a novel ELO technology.

Chapter 4 introduces this ELO technology for CdTe material using a nearly lattice-matched and water-soluble MgTe sacrificial layer grown on InSb substrates. The freestanding CdTe DH thin films are obtained with the enhanced optical performance. A fabricated monocrystalline CdTe thin-film solar cell demonstrates a power conversion efficiency of 9.8%.

This ELO technology also enables the fabrication of 1.7/1.1-eV MgCdTe/Si or MgCdTe/CIGS tandem solar cells. Chapter 5 demonstrates a monocrystalline 1.7-eV MgCdTe solar cells with an active-area efficiency as high as 15.2%. Loss analysis of V_{OC} and J_{SC} is discussed.

Chapter 6 reports the proton radiation study for the CdTe DHs. The CdTe DHs show superior radiation hardness, indicating the monocrystalline CdTe thin-film solar cells with light weight, high-efficiency and high power density are ideal for space applications.

Finally, the conclusion and outlook of the present work are included in Chapter 7.

CHAPTER 2

TRANSPORT ACROSS CDTE/INSB HETEROVALENT INTERFACE

II-VI/III-V heterovalent structures have attracted considerable attention due to the unique physical properties at their interfaces and viability of their use in monolithically-integrated electronic and optoelectronic devices. The CdTe/InSb material system is particularly interesting due to the close lattice match ($\Delta a/a < 0.05\%$ at 25 °C) which allows high quality CdTe layers with very low defect density to be grown on large area InSb substrates [29], and possible applications including solar cells, multiple-quantum-well lasers [30], multicolor photodetectors [31] and HEMT structures with exceptionally high electron mobilities [32]. Some of the applications take advantage of the bandgap of CdTe and InSb while other applications utilize the unique properties at the CdTe/InSb interface.

One of the applications of the CdTe/InSb system is in CdTe solar cells grown on InSb substrates, as discussed in Chapter 1. Even though previous experimental results indicated that there is very small resistance between a CdTe/MgCdTe DH and InSb substrate, the interfacial composition profile and transport processes are still relatively unclear. A better understanding of the nature of transport across the CdTe/InSb heterovalent interface not only helps to fully understand the junction between CdTe/MgCdTe DHs and InSb substrates but also reveals the unique physical properties of the II-VI/III-V heterovalent interface.

2.1 Characterizations of CdTe/InSb Heterojunction and Heterovalent Interface

Two samples, N-CdTe/n-InSb and N-CdTe/p-InSb heterojunctions, as shown in Fig. 2.1, are grown on commercially-obtained n-type single crystal InSb(001) substrates (doped with Te at ~5×10^{17} atoms/cm^3). CdTe layers are doped n-type with indium (In) at ~ 1×10^{18} cm^{-3} and InSb layers are doped n-type (p-type) with Te (Be) at ~5×10^{18} cm^{-3} (1×10^{19} cm^{-3}). The InSb and CdTe epitaxial growth processes are performed in a dual-chamber molecular beam epitaxy system which consists of separate II–VI and III–V growth chambers connected by an ultrahigh vacuum (UHV) preparation chamber. The InSb buffer layer and doped InSb layer are grown in the III-V growth chamber and samples are then transferred to the II-VI growth chamber to grow CdTe layers. Detailed growth conditions have been reported previously [9].

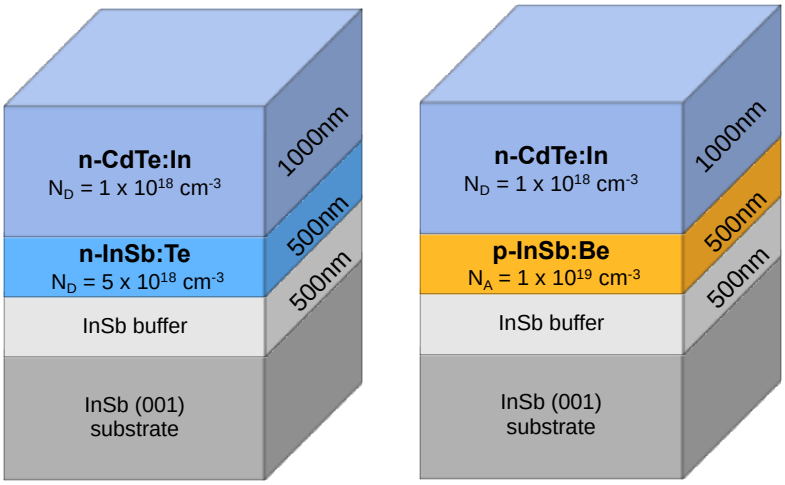

Figure 2.1 Schematic layer structure of N-CdTe/n-InSb (left) and N-CdTe/p-InSb (right).

The indium out-diffusion from the InSb layer to the CdTe layer is examined by Secondary Ion Mass Spectrometer (SIMS) measurements carried out at Evans Analytical Group. The indium out-diffusion profiles in N-CdTe/n-InSb and N-CdTe/p-InSb

heterojunctions are illustrated in Fig. 2.2. For both N-n and N-p samples, there is obvious indium out-diffusion across CdTe/InSb interface. Based on the indium atom density, a

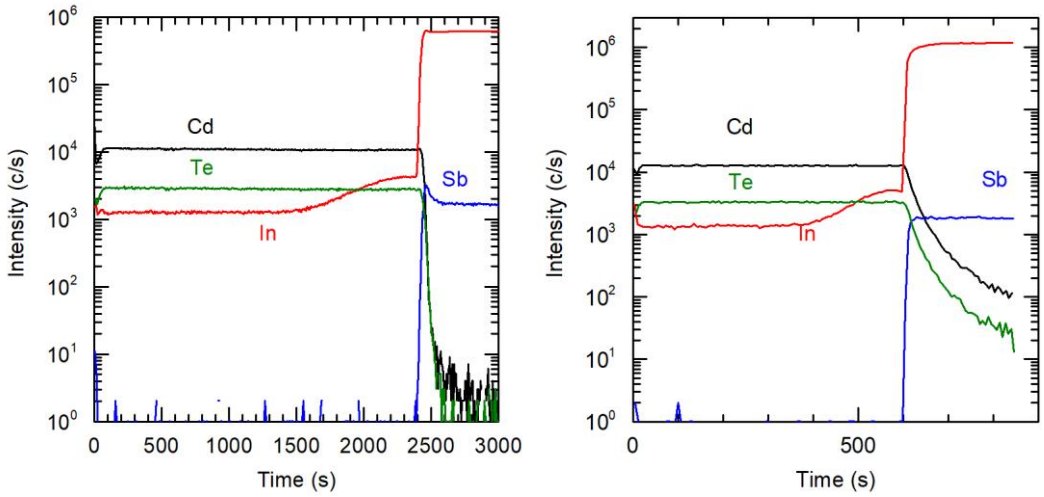

Figure 2.2 Dopant profiles of N-CdTe/n-InSb (left) and N-CdTe/p-InSb (right) heterojunctions. An obvious higher In doping density in CdTe side near the interface is observed for two samples.

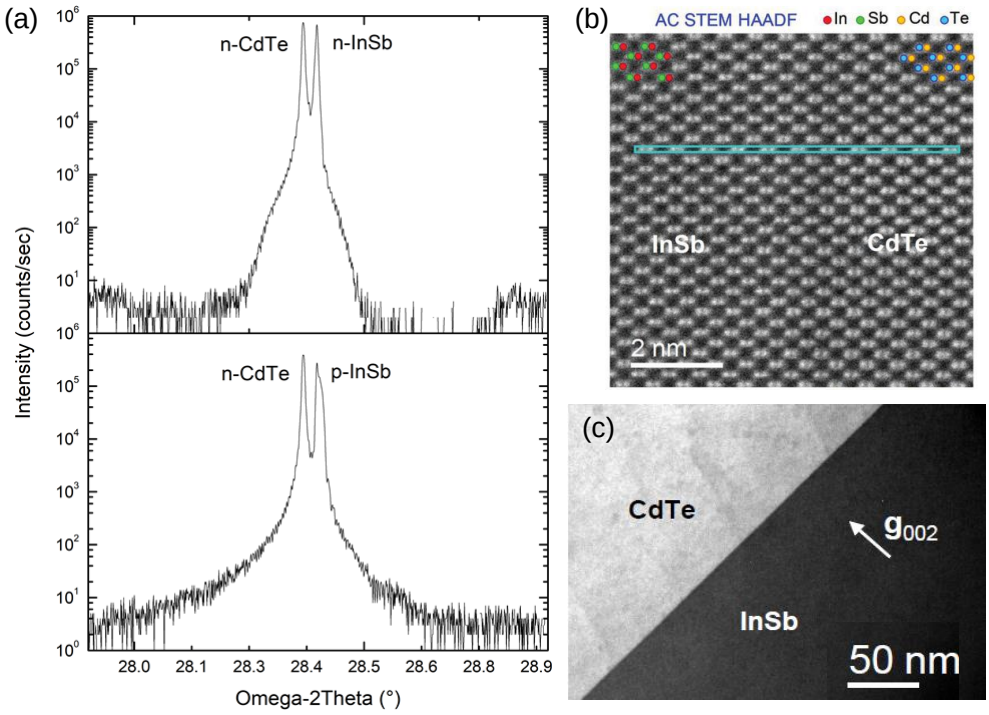

Figure 2.3 (a) High-resolution (004) XRD profiles of N-CdTe/n-InSb (left top) and N-CdTe/p-InSb (left bottom). (b) Aberration-corrected bright field STEM image and (c) chemically sensitive g_{002} dark-field TEM image of CdTe/InSb heterojunctions [33].

rough estimation is given that the doping density of the CdTe layer near the interface is five times larger than that of bulk region. This phenomenon increases the effective doping density near the interface, and further increases the built-in electric field at the interface.

High-resolution X-ray diffraction (HRXRD) measurements are performed to examine the crystalline quality of the two samples, as shown in Fig. 2.3 (a), HRXRD measurements indicate the high crystalline order of CdTe and InSb layers with two sharp, narrow peaks corresponding to the CdTe and InSb lattice constants. An aberration-corrected bright field STEM image, illustrated in Fig. 2.3 (b), and a chemically-sensitive g_{002} dark-field TEM image, shown in Fig. 2.3 (c), demonstrate a coherent and defect-free CdTe/InSb interface, and the clear boundary at the CdTe/InSb interface, respectively [33].

Unintentional-doped CdTe/InSb heterojunction samples are characterized by Monochromatic X-ray photo-emission spectroscopy (XPS) and ultraviolet photoemission spectroscopy (UPS) [34]. From the results, In-Te bonding is observed at the interface, as shown in Fig. 2.4 (a). The "III-VI" bond formation is not only present in the CdTe/InSb system. It is a general tendency to form III-VI bonds at a II-VI/III-V interface. Other material systems, like GaAs/ZnSe, GaSb/ZnTe, CdS/InP and AlSb/ZnTe [35–38], have

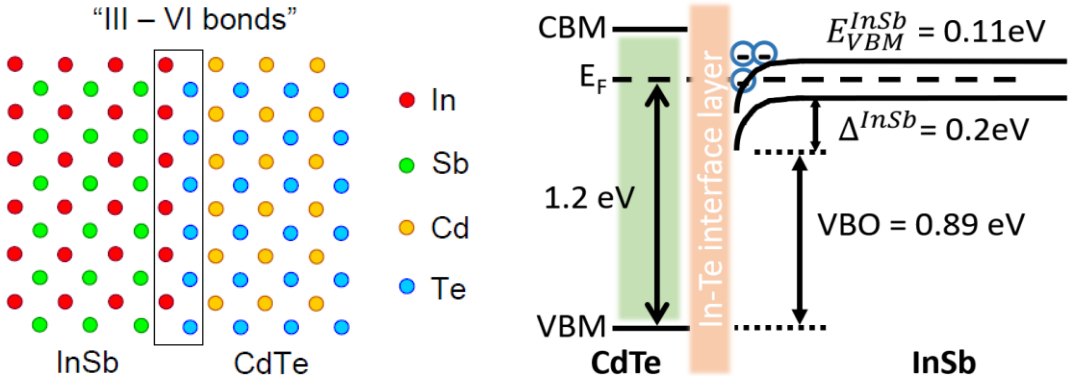

Figure 2.4 (a) In-Te bonds at the interface of CdTe/InSb heterojunctions. (b) Schematic band alignment of unintentional-doped CdTe/InSb heterojunctions [34].

reported the formation of III-VI bonds at their interfaces. Then, in a single “III-VI” bond, there are nine valence electrons. Eight electrons form a stable structure and the one excess electron can move freely. Due to the lower potential energy of the InSb side, the excess electrons would flow to the InSb side and accumulate. Thus, a downward band bending at the InSb side near the interface would appear. XPS and UPS results showed that a 0.2eV downward band bending exists at the InSb side. 0.89eV valence band-offset between unintentional-doped CdTe and InSb is observed. The schematic band alignment of unintentional-doped CdTe/InSb sample is shown in Fig. 2.4 (b). The XPS and UPS measurements demonstrated accurate band-offset information. However, the band diagram of the N-CdTe/n-InSb and N-CdTe/p-InSb are still unclear. With additional information provided by electron affinity values for CdTe and InSb, a schematic band diagram of N-n and N-p CdTe/InSb heterojunctions is plotted, as shown in Fig. 7. For doped CdTe/InSb heterojunctions, there are four main points to be noted:

1) A potential barrier on the CdTe side
2) A ~1.5 nm In-Te interfacial layer
3) Downward band bending on the InSb side
4) An inversion region on p-InSb side

Due to the smaller electron affinity of CdTe compared with InSb, there is a potential barrier at CdTe side in a CdTe/InSb heterojunction. There is also an In-Te interfacial layer at the interface, acting as barrier as well. Thus, an effective barrier consisting of a CdTe barrier and an In-Te interfacial layer is introduced in the transport analysis. As discussed above, downward band bending at the InSb side, caused by accumulated electrons, is at

least 0.2 eV. Compared with the 0.17 eV bandgap of InSb, the 0.2 eV downward band bending would cause an inversion region at the p-InSb side.

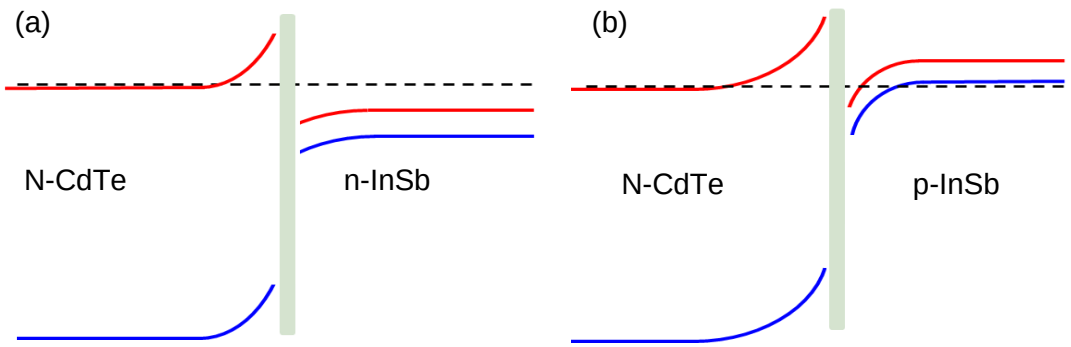

Figure 2.5 Schematic band diagrams of (a) N-CdTe/n-InSb heterojunction and (b) N-CdTe/p-InSb heterojunctions.

2.2 Measurement of Temperature-Dependent *J-V* Characteristics

To investigate the transport properties, devices are processed from the doped CdTe/InSb heterojunctions. The device structures are shown in Fig. 2.6. For both devices, the CdTe layer and part of InSb layer are etched, and the mesa size is 0.2 mm × 0.2 mm. In is deposited on the top surface of CdTe as the top contact. the bottom contact is Ti/Pt/Au,

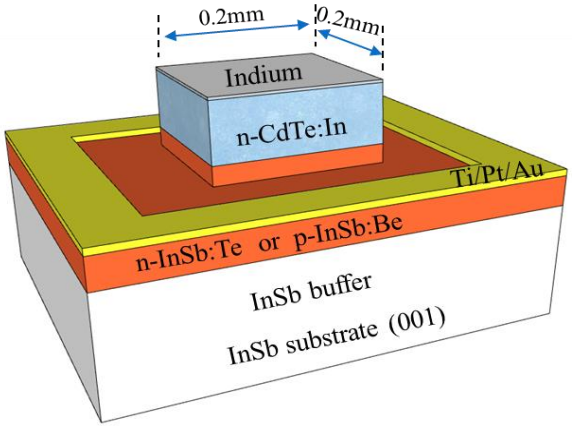

Figure 2.6 Device structures of the N-CdTe/n-InSb and N-InSb/p-InSb heterojunctions.

depositing on the surface of InSb layers. During the measurements, the current is forced to flow through the p-InSb (n-InSb) layer to the n-CdTe layer. TLM patterns reveal the contact resistance of the In/n-CdTe is 1.2×10^{-4} Ω·cm^2. The contact resistance of Ti/Pt/Au/n-InSb is 1.1 $\times10^{-6}$ Ω·cm^2 and the resistance of Ti/Pt/Au/p-InSb is 6.9 $\times10^{-5}$ Ω·cm^2. The resistances of all these contacts are small enough to take accurate current-voltage (*J-V*) measurements of the CdTe/InSb heterojunctions.

The *J-V* measurements are carried out in a cryogenic probe station. The temperature of the substrate holder can be cooled down to 77 K by liquid nitrogen. The temperature-dependent *J-V* curves are shown in Fig. 2.7. The voltage range is from -0.1 V to 0.1 V and the current density range is -20 A/cm^2 to 20 A/cm^2. First, all the *J-V* curves of N-n junction and N-p junction show ohmic behavior at different temperatures, which indicates the

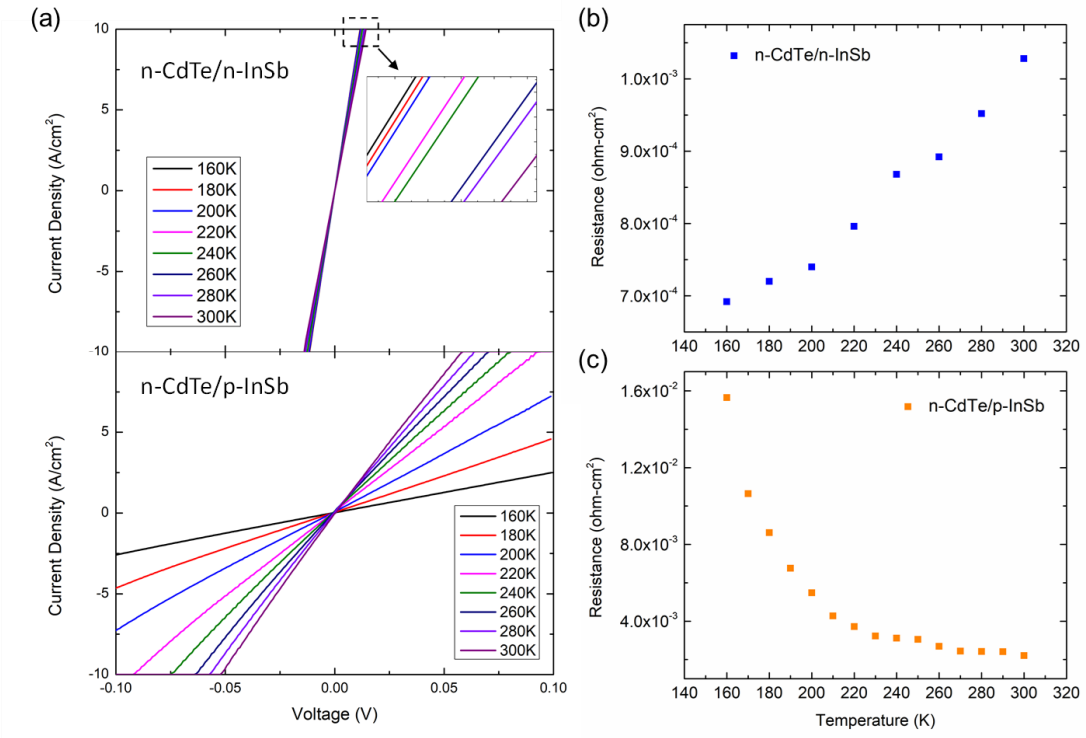

Figure 2.7 (a) Temperature-dependent *J-V* characterization of N-CdTe/n-InSb and N-CdTe/p-InSb heterojunctions. (b) Resistance versus temperature of N-CdTe/n-InSb and (c) Resistance versus temperature of N-CdTe/p-InSb heterojunctions.

tunneling nature of transport across the CdTe/InSb interface. Second, the total resistance of the N-n junction increases with temperature while resistance of the N-p junction decreases with the temperature. The different trends of resistance versus temperature of N-n and N-p junctions suggest differences in the dominant transport processes across the CdTe/InSb interface.

2.3 Interface Transport Analysis

For the heavily-doped N-CdTe/n-InSb heterojunction, both of the two sides are degenerate. The transport across the N-n heterojunction is dominated by the majority carrier, electrons. When the bias is applied, electrons would transport from one side, overcoming the CdTe barrier into the other side. The ohmic behavior of *J-V* characteristic indicates electron transport through the CdTe barrier is a tunneling process. The resistance of the N-CdTe/n-InSb heterojunction mainly comes from three parts: contact resistance, bulk resistance and interface resistance. The total resistance can be estimated from *J-V* characteristics. The contact resistance is measured from TLM patterns and the bulk resistance can be calculated from carrier density, mobility [39,40] and device size. Thus, interface resistance equals total resistance minus contact resistance and bulk resistance. The results, detailed in Table 2.1 below, show that interface resistance is much larger than contact resistance and semiconductor resistance, and as such it dominates the transport process in the N-CdTe/n-InSb heterojunction.

Table 2.1 Resistance analysis for N-n device (Unit: $\Omega \cdot cm^{-2}$)

Total Resistance	$\rho_{contact}$	ρ_{bulk}	$\rho_{interface}$
1×10^{-3}	1.2×10^{-4}	1.05×10^{-6}	$\sim 9 \times 10^{-4}$

The increase in resistance of N-n heterojunctions as temperature increases has been reported previously in tunneling diodes [41,42], and is attributed to smaller thermal tails as the temperature drops, allowing a greater percentage of all carriers to have low enough energy to be within the region of band overlap and thus able to tunnel.

For the N-CdTe/p-InSb heterojunction, according to the band diagram, there is a CdTe potential barrier and an inversion region at the InSb side near the interface due to the extra electron accumulation. Carrier transport across the CdTe side is similar to that of the N-n heterojunction. At the InSb side, there is a p-n junction between the n-type inversion region and the p-InSb. Due to the ohmic behavior of the N-p heterojunction, there are three possible processes in the InSb interband transport:

1) Band-to-band tunneling
2) Trap-assistant tunneling
3) Generation-Recombination processes

The schematic transport process is shown in Fig 2.8 below. Assuming a neutral center and a uniform electric field in the depletion region, the band-to-band tunneling (BTBT) current, trap-assisted tunneling (TAT) current and generation-recombination (G-R) current can be expressed as [43–45]:

$$J_{BTBT} = \frac{\sqrt{2m_n^*}q^3EV}{4\pi^2\hbar^2E_g^{1/2}}\exp\left(-\frac{4\sqrt{2m_n^*}E_g^{3/2}}{3qE\hbar}\right) \tag{2.1}$$

$$J_{BTBT} = J_{G-R} = \frac{qn_iW}{\tau_{eff}}\left[1-\exp\left(-\frac{qV}{2kT}\right)\right] \propto \frac{qn_iW}{\tau_{eff}}\cdot\frac{qV}{2kT} \tag{2.2}$$

$$J_{TAT} = \frac{q^3m_n^*EM^2WN_T}{8\pi\hbar^3(E_g-E_T)}\exp\left(-\frac{4\sqrt{2m_n^*(E_g-E_T)}}{3qE\hbar}\right) \tag{2.3}$$

where n_i is the intrinsic carrier concentration, m_n^* is the effective electron mass, q is the electron charge, E is the neutral region electric field, k_B is the Boltzmann constant, T is the temperature, V is the bias voltage, W is the depletion width, τ_{eff} is the effective carrier lifetime, N_t is the activated trap density, E_t is the trap energy location, measured from the valence band edge, and M^2 is a matrix element associated with the trap potential, assumed to be 1×10^{-23} eV^2 cm^3. The intrinsic carrier concentration and bandgap are also dependent on temperature, which can be expressed as:

$$n_i(T) = \sqrt{N_C(T)N_V(T)}\,\exp\left(-\frac{E_g}{2kT}\right) \tag{2.4}$$

$$E_g(T) = E_{g0} - \frac{\alpha T^2}{T+\beta} \tag{2.5}$$

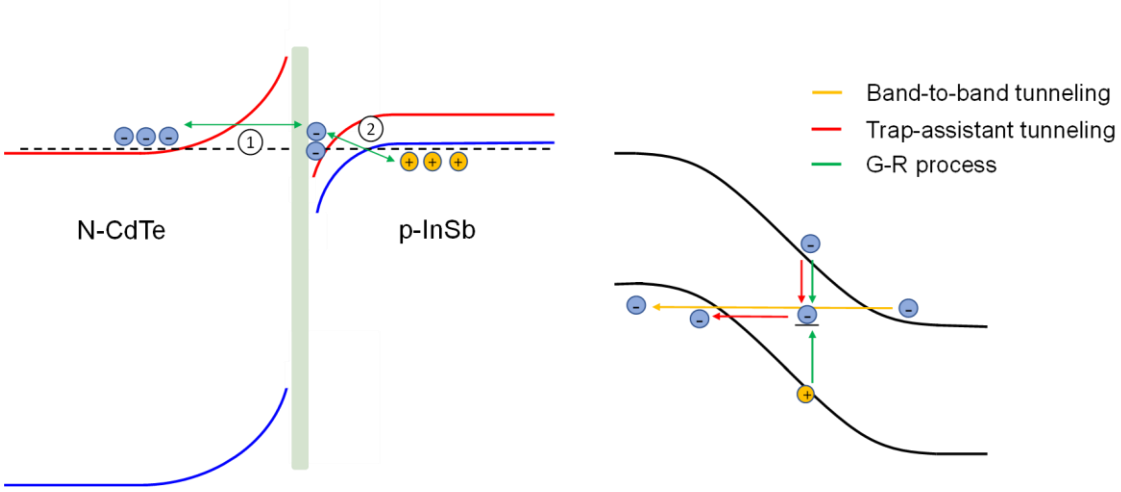

Figure 2.8 (a) Schematic carrier transport process of N-CdTe/p-InSb heterojunction. It can be divided into two processes. First one is transport across CdTe barrier and the second is InSb interband transport. (b) Schematic InSb interband transport processes. Yellow line represents band-to-band tunneling. Red line represents trap-assistant tunneling and green line represents generation-recombination process.

Seen from the formulas, the temperature-dependent factor in tunneling current, including band-to-band tunneling and trap-assistant tunneling, only comes from bandgap changing, which is slightly dependent on temperature. The generation-recombination

current is nearly proportional to the n_i under small bias, which is an exponential relationship with temperature. Based on the formula, a current (log scale) versus 1/*kT* diagram is plotted, as shown in Fig 2.9 (a).

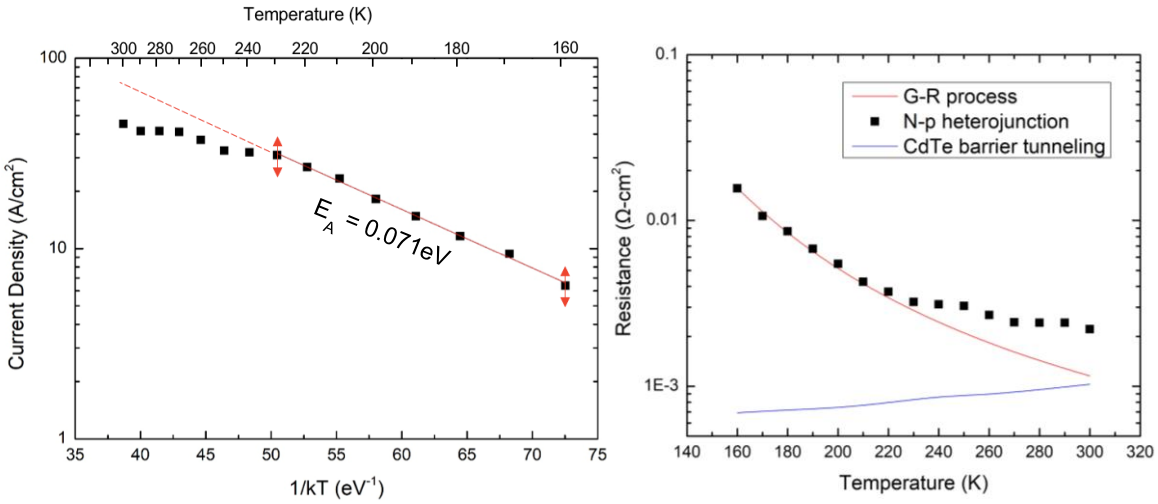

Figure 2.9 (a) Current density (log scale) of N-p heterojunction versus *1/kT*. The black dots are experimental results. The red line is linear fitting. (b) Resistance of N-p heterojunction versus temperature. Black dots are resistance from measurement. Red line is resistance from InSb interband transport (G-R process). Blue line is resistance from CdTe barrier tunneling.

From the linear fitting of the resistance versus 1/*kT* diagram, the activation energy extracted is about 0.071 eV. Considering the bandgap narrowing effect of InSb under heavily doped conditions (N_A=1×10^{19} cm^{-3}), the bandgap of InSb is about 0.138 eV [46]. The activation energy is just half of the bandgap, which indicates $J \propto \exp\left(-\frac{E_g}{2kT}\right)$. This is consistent with the G-R process, suggesting the G-R process dominates the InSb interband transport. In Fig 2.9 (a), the linear fitting deviates from the experimental results from 230 K to room temperature. In other words, near room temperature, the measured resistance is gradually larger than the G-R resistance from InSb interband transport. The reason is probably that when temperature increases, CdTe barrier tunneling becomes a more and

more important factor for the whole transport process. Fig 2.9 (b) shows the resistance of the G-R process and the CdTe barrier versus temperature.

CHAPTER 3

CDTE DOUBLE-HETEROSTRUCTURE SOLAR CELLS WITH DIFFERENT HOLE CONTACTS

A "remote junction" concept has been proposed and used to demonstrate CdTe/MgCdTe DH solar cells with record high V_{OC}. The basic idea of the "remote junction" design is introduced in Section 1.2.4, in which unintentionally-doped intrinsic and n-type MgCdTe layers are used as the barriers for holes and electrons, respectively, and a p-type a-Si:H is used as hole contact. Despite success in demonstrating high V_{OC} and efficiency, this design has drawbacks such as the doped a-Si:H layer has considerable parasitic light absorption due to the moderate bandgap (1.7 eV). Therefore, other alternative materials, such as ZnTe with a wider bandgap of 2.27 eV, are tested and show promise as hole contacts for the CdTe DH solar cells [47]. In this chapter, we present the results of an in-depth study of the CdTe/MgCdTe DH solar cells with three different "remote junction" designs, which use p-type a-Si:H, ZnTe:As and ZnTe:Cu hole-contact layers [48].

3.1 Device Structure and Performance

Fig. 3.1 shows the layer structure of the studied solar cells with three different kinds of hole contacts using a-Si:H, ZnTe:As and ZnTe:Cu p-type layers, respectively. For CdTe solar cells with a-Si:H, detailed descriptions of the growth and processing is discussed in an earlier publication [26]. The p-type a-Si:H with estimated doping level of 10^{18} cm^{-3} is 8 nm thick and deposited by plasma-enhanced chemical vapor deposition (PECVD). Two different approaches are used to create heavily doped ZnTe hole contacts. In the case of arsenic doping, the top 20-nm-thick p-ZnTe layer is grown in a custom-designed metal-

organic chemical vapor deposition (MOCVD) system at 300 °C with a carrier concentration of 2×10^{18} cm^{-3} determined from Hall measurements [49]. In the case of copper doping, the 15-nm-thick ZnTe contact layer is grown by MBE. Then a 1-nm-thick layer of copper is sputtered on this layer first, where it then diffused into the ZnTe. The average carrier concentration is 4×10^{18} cm^{-3} determined by Hall measurements. More details can be found in previous work [47].

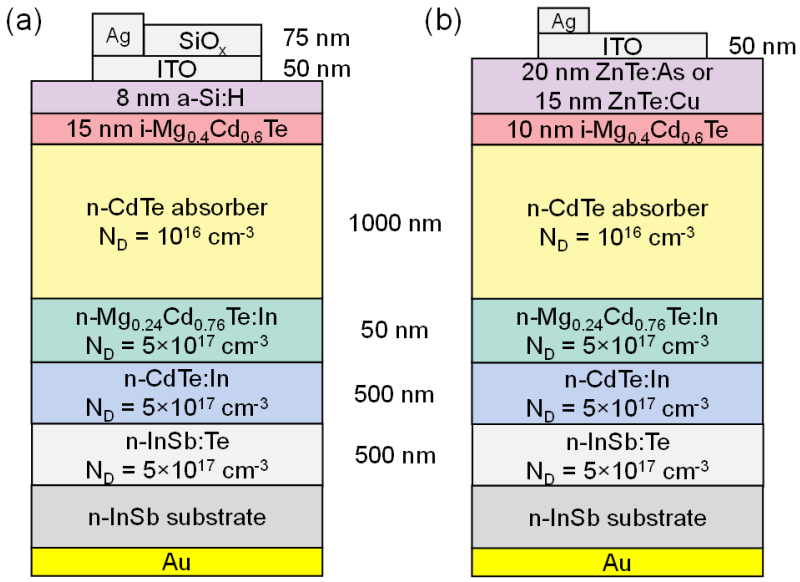

Figure 3.1 Layer structure of the CdTe/MgCdTe DH solar cells with three different hole contacts, a-Si:H, ZnTe:As and ZnTe:Cu [27,47,49].

The device performance of these three CdTe solar cells under AM1.5G illumination are summarized in Table 3.1. The device parameters of CdTe device with a-Si:H are extracted from previous work [26]. Solar cells with p-type ZnTe:As layers exhibit higher short-circuit current (J_{SC}) compared with hole contacts of a-Si:H. Although the J_{SC} is improved, the V_{OC} is lower. CdTe solar cells with ZnTe:Cu hole-contact layers, show both lower V_{OC} and J_{SC}.

Table 3.1 Maximum device parameters for various contact materials

Parameter	a-Si:H/ MgCdTe/CdTe	ZnTe:As/ MgCdTe/CdTe	ZnTe:Cu/ MgCdTe/CdTe
J_{SC} (mA/cm^2)	24.5	25.46	19.85
V_{OC} (V)	1.096	0.853	0.894
FF (%)	75.57	73.66	63.66
η (%)	20.3	15.99	11.30

3.2 The Maximum Achievable V_{OC}

3.2.1 Built-in Voltage Limited

To determine the built-in voltage (V_{bi}) between p-type hole contacts and n-CdTe, capacitance-voltage (C-V) measurements are conducted on the three devices with different hole contacts. The measurement results are shown in Fig. 3.2. With a constant doping concentration, the capacitance is related to the applied reverse-bias voltage V through the formula of (the influence of i-MgCdTe thin layer is neglected)

$$C = A\sqrt{\frac{qK_s\varepsilon_o N_D}{2(V_{bi}+V)}} \tag{3.1}$$

where A is the area of the junction, $K_s\varepsilon_o$ is the dielectric constant of the semiconductor, and N_D is the donor concentration [50].

The V_{bi} values determined from 1/C^2-V plots are 1.20 V, 1.23 V and 0.90 V for the hole contacts of a-Si:H, ZnTe:As and ZnTe:Cu, respectively. The low V_{OC} of devices with ZnTe:Cu is mainly due to the low V_{bi} across the p-ZnTe:Cu/n-CdTe junction. In contrast, a ZnTe:As layer offers a higher V_{bi} than that of ZnTe:Cu or even a-Si:H.

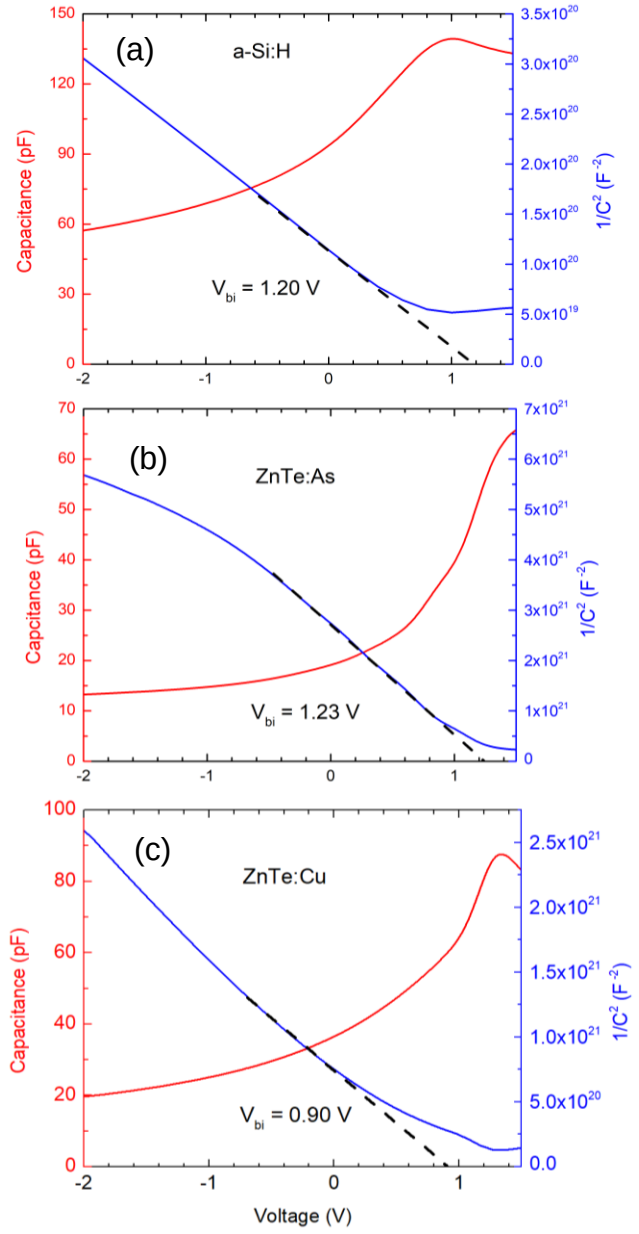

Figure 3.2 Capacitance-Voltage measurement results for CdTe solar cells with (a) a-Si:H, (b) ZnTe:As and (c) ZnTe:Cu hole contacts. $1/C^2$ – V profiles are shown on the right *y*-axis. V_{bi} can be estimated from the intercept of $1/C^2$ on the *x*-axis.

To further confirm the V_{bi} limited V_{OC} in the devices with ZnTe:Cu hole contact, temperature-dependent and excitation-dependent V_{OC} measurements of the devices are conducted, as shown in Fig. 3.3. The quasi-Fermi level splitting (ΔE_F) in the CdTe absorber under illumination can be expressed as:

$$\Delta E_F = E_g - (E_c - E_{Fn}) - \left(E_{Fp} - E_V\right) = E_g - kTln\frac{N_C N_V}{n_n p_n} \quad (3.2)$$

where E_g, E_C, E_V, E_{Fn} and E_{Fp} represent bandgap, conduction band, valence band, electron quasi-Fermi level and hole quasi-Fermi level of the CdTe absorber, respectively. N_C, N_V, n_p and p_p are effective density of state of conduction band and valence band, electron density and hole density in the p-type CdTe layer, respectively. Assuming the photo generation rate per unit volume G is uniform across the whole absorber region, the electron and hole densities can be replaced by $G\tau + n_i^2/N_A$ and $G\tau + N_A$, where τ, n_i and N_A are minority carrier lifetime, intrinsic carrier concentration and acceptor concentration in the p-type CdTe layer, respectively. When the built-in voltage (V_{bi}) of the solar cell is larger than the ΔE_F and no voltage is dropped on Schottky contacts, (3.2) can be revised to:

$$V_{oc} \approx E_g - kTln\frac{N_C N_V}{G\tau(G\tau + N_A)} \quad (3.3)$$

Considering the N_C and N_V decrease with decreasing temperature [43] and the SRH carrier lifetime and the bandgap of CdTe increase with decreasing temperature [17,51], the V_{OC} of a CdTe solar cell should increase almost linearly or with even higher increasing rate as temperature goes down until reaching the V_{bi} limit or the donors and acceptors are incompletely ionized. From the Fig. 3.3, the V_{OC} of the device with the ZnTe:Cu hole contact keeps increasing with decreasing temperature under low excitation. Under 1 sun illumination, the V_{OC} is pinned at the 0.9 V, i.e., the V_{bi} with decreasing temperature. The V_{OC} limitation from the temperature-dependent V_{OC} measurement matches the low V_{bi} from the C-V measurement very well, further confirming the low V_{bi} limits the V_{OC} in the CdTe DH solar cells with a ZnTe:Cu hole contact.

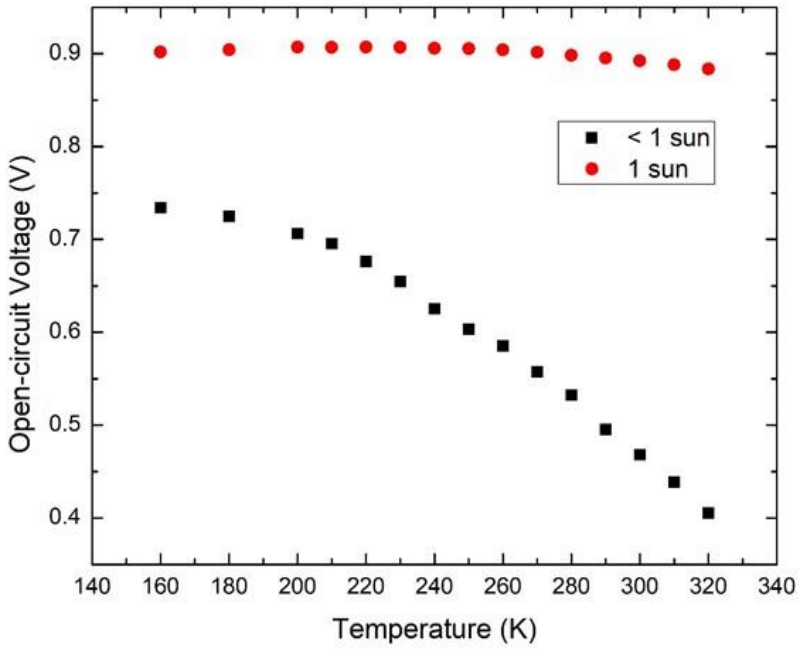

Figure 3.3 Temperature-dependent and excitation-dependent V_{OC} measurement of the CdTe DH solar cells with the ZnTe:Cu hole contact.

Based on previous studies mentioned in Section 3.1, all of the three hole contacts demonstrated relatively high doping concentration (> 10^{18} cm^{-3}). The possible reason for the low V_{bi} of the device with ZnTe:Cu contact is that the copper atoms in the ZnTe layer may further diffuse into the CdTe absorber and serve as dopant. The copper diffusion induced doping compensation would reduce the n-type doping concentration in the CdTe absorber, reducing the V_{bi} and further limiting V_{OC} of the device.

For the devices with a-Si:H and ZnTe:As hole contacts, the carrier concentration of both p-type and n-type layers are known. The V_{bi} only depends on the valence band-offset between hole contacts and CdTe absorber (ΔE_V) and can be expressed as:

$$V_{bi} = E_{g,CdTe} - \Delta E_V - (E_{Cn} - E_{Fn}) - \left(E_{Fp} - E_{Vp}\right) \tag{3.4}$$

where E_{Fn}, E_{Fp} are quasi-Fermi levels of electrons and holes in absorber and hole contact, respectively; E_{Cn} is the conduction band edge of n-type CdTe absorber and E_{Vp} is the valence band edge of hole contact. The schematic band diagram is shown in Fig. 3.4.

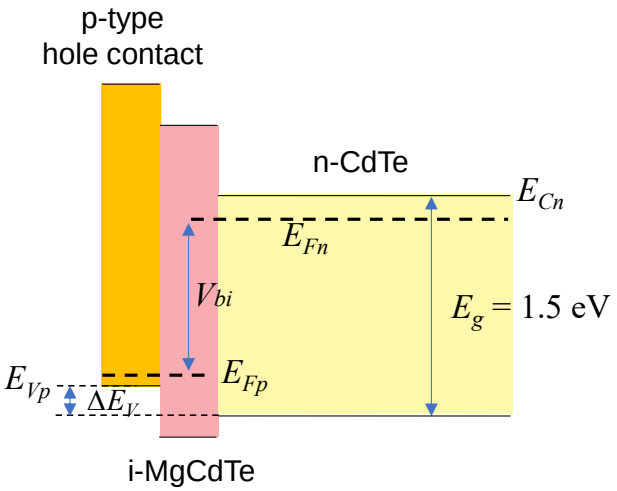

Figure 3.4 Schematic band alignment of the CdTe/MgCdTe DH with a p-type hole contact. The V_{bi} can be determined based on the carrier concentration of n-type and p-type layers, bandgap of absorber and the valence band offset between hole contact and absorber.

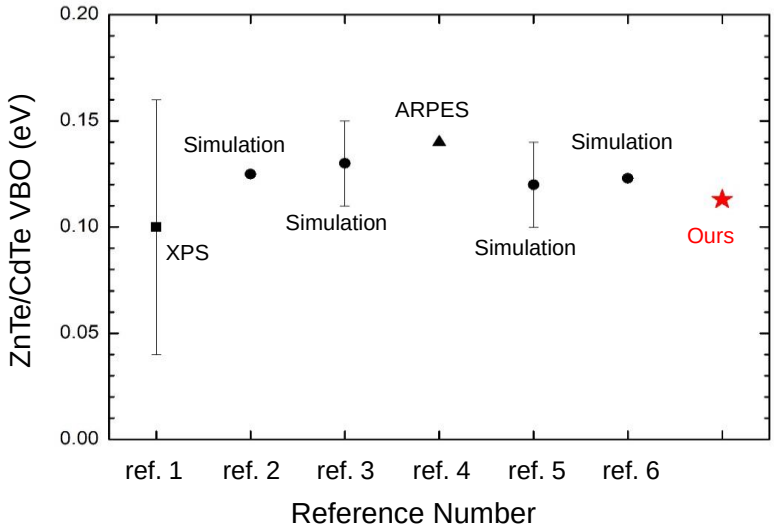

Figure 3.5 Comparison of ZnTe/CdTe valence band offset extracted using different methods.

Based on the doping concentration of ZnTe:As, a-Si:H and CdTe absorber from the previous studies, and the corresponding V_{bi} values extracted from the C-V measurements, the valence band offset of ZnTe/CdTe and a-Si/CdTe are 0.113 eV and 0.121 eV, respectively. We further compare our valence band offset data of ZnTe/CdTe with published results [52–57], including X-ray photoelectron spectroscopy (XPS), angle-resolved photoemission spectroscopy (ARPES) and first principle calculations, as shown in Fig. 3.5.

3.2.2 Carrier Lifetime Limited

The next possible factor which limits the maximum achievable V_{OC} is minority carrier lifetime. If the carrier lifetime is short due to high recombination rate, the quasi-fermi-level splitting decreases and thus reduces the V_{OC}.

To determine the minority carrier lifetime, time-resolved photoluminescence (TRPL) measurements are conducted for the three types of devices under open circuit condition, and the results are plotted in Fig. 3.6. The TRPL decay time is referred to as the effective minority carrier lifetime. From fitting the tails of the PL decay curves, the minority carrier lifetime are 300 ns, 170 ns and 52 ns for devices with a-Si:H, ZnTe:As and ZnTe:Cu, respectively. Earlier work shows the minority carrier lifetimes in doped CdTe/MgCdTe DHs are on the order of hundreds of nanoseconds. After depositing hole contact of a-Si:H on the top of CdTe/MgCdTe DH, minority carrier lifetime maintains the same level. However, there are obvious degradations of minority carrier lifetime in CdTe devices with p-ZnTe hole contacts. Due to the large lattice mismatch of ZnTe (6.10 Å) and CdTe (6.48 Å), it is anticipated that some misfit dislocations are generated at the ZnTe/MgCdTe interface and they may penetrate into the absorber region, serving as SRH recombination

centers and affecting the minority carrier lifetime. For devices with a-Si:H, due to the lower deposition temperature and amorphous condition, the defects generated by small lattice mismatch may not penetrate into the absorber region. Therefore, CdTe/MgCdTe DHs with p-type a-Si:H demonstrate longer minority carrier time and thus higher V_{OC} compared with ZnTe hole contacts at the end.

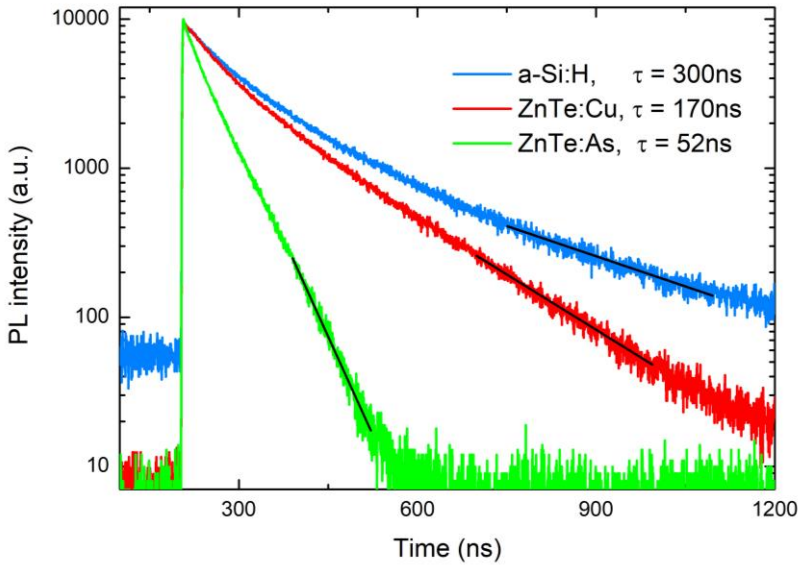

Figure 3.6 Normalized time-resolved photoluminescence measurement at room temperature for CdTe devices with a-Si:H, ZnTe:As and ZnTe:Cu.

To distinguish the majority recombination process happens at the interface or in the bulk, temperature-dependent V_{OC} measurements are conducted. Based on the previous studies, which are mentioned in Section 1.2, the radiative recombination, R^{rad} in the CdTe absorber, the SRH recombination in the depletion region R^{d}, in the quasi-neutral region R^{b} and the interface recombination R^{int} at the p-contact/i-MgCdTe interface are considered as the main recombination mechanisms. The recombination at the i-MgCdTe/n-CdTe interface is neglected due to the nearly lattice-matched and high-quality MgCdTe/CdTe interface [17]. Fig. 3.7 shows the band diagram of a CdTe DH device with

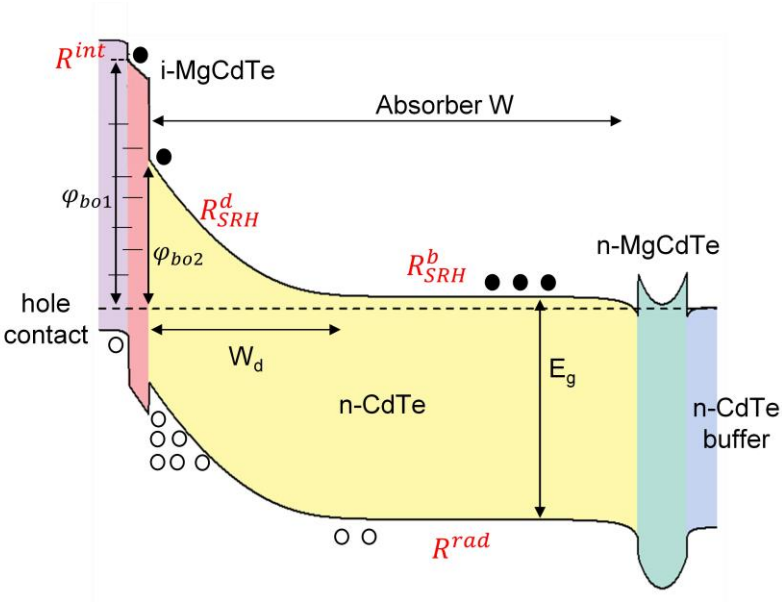

Figure 3.7 Energy band diagram of a CdTe DH solar cell with different recombination processes, including SRH recombination in the depletion region (R^d) and the quasi-neutral region (R^b), radiative recombination in the CdTe absorber (R^{rad}) and interface recombination (R^{int}) at the p-contact/i-MgCdTe interface.

different recombination mechanisms. Each recombination rate is expressed as the product of a voltage-independent recombination coefficient and an exponential an exponential function of voltage as follows [43,58]:

$$R^{int} = (R_0^{int,therm} + R_0^{int,tunnel})e^{\frac{qV}{k_BT}} \tag{3.4a}$$

$$R^{d} = R_0^{d} e^{\frac{qV}{2k_BT}} \tag{3.4b}$$

$$R^{b} = R_0^{b} e^{\frac{qV}{k_BT}} \tag{3.4c}$$

$$R^{rad} = R_0^{rad} e^{\frac{qV}{k_BT}} \tag{3.4d}$$

where k_B is the Boltzmann constant, R_0^{int}, R_0^{d}, R_0^{b} and R_0^{rad} are bias-independent (V = 0) recombination coefficients at the p-contact/i-MgCdTe interface, in the depletion region, in

the quasi-neutral region, and the CdTe absorber, respectively. The mathematical formula for these recombination coefficients can be expressed as follows:

$$R_0^{int,therm} = S_e N_{C,MgCdTe} \cdot e^{-\frac{q\varphi_{bo1}}{k_B T}} \tag{3.5a}$$

$$R_0^{int,tunnel} = S_e N_{C,CdTe} P_{tunnel} \cdot e^{-\frac{q\varphi_{bo2}}{k_B T}} \tag{3.5b}$$

$$R_0^{d} = \frac{W_d}{\tau_e + \tau_h} n_i \tag{3.5c}$$

$$R_0^{b} = \frac{W - W_d}{\tau_h} \frac{n_i^2}{N_D} \tag{3.5d}$$

$$R_0^{rad} = (1 - \gamma) B W n_i^2 \tag{3.5e}$$

where S_e is the interface recombination velocity, $N_{C,MgCdTe}$ and $N_{C,CdTe}$ are the effective density of state of conduction band in the i-MgCdTe layer and CdTe absorber, respectively; φ_{bo1} and φ_{bo2} are the potential barrier for electrons at the p-contact/i-MgCdTe and i-MgCdTe/n-CdTe interfaces, as labeled in Fig. 3.7. P_{tunnel} is the tunneling possibility of electron from CdTe absorber to the hole contact layer, which is dependent with the i-MgCdTe barrier height and thickness, and the defect state energy distribution in the a-Si:H hole contact layer. W and W_d represent the width of absorber and depletion region, respectively. The τ_e and τ_h are time constants related to the trap density (N_t) and capture cross-section for electrons (σ_e) and holes (σ_h) as $\tau_e = (N_t \sigma_e \nu_{th})^{-1}$ and $\tau_h = (N_t \sigma_h \nu_{th})^{-1}$. The ν_{th} refers to the usual average thermal velocity of charge carriers. N_D and n_i are the n-type doping concentration and intrinsic carrier concentration in the CdTe absorber, respectively. γ and B are photon recycling factor and radiative recombination coefficient, as mentioned in Section 1.2.

Under the open-circuit condition, at which all photon-generated carriers recombine, total generation across the absorber G_aW should equal to the total recombination rate ΣR, leading to the following equation:

$$(R_0^{int,therm} + R_0^{int,tunnel} + R_0^b + R_0^{rad})e^{\frac{qV_{oc}}{k_BT}} + R_0^d e^{\frac{qV_{oc}}{2k_BT}} = G_aW \tag{3.6}$$

By solving the equation (3.6), the V_{OC} is given by [59,60]:

$$V_{oc} = \frac{2k_BT}{q} ln \left[\frac{1}{2} \frac{R_0^d}{R_0^{int,therm} + R_0^{int,tunnel} + R_0^b + R_0^{rad}} \cdot \left(\sqrt{4G_aW \frac{R_0^{int,therm} + R_0^{int,tunnel} + R_0^b + R_0^{rad}}{(R_0^d)^2} + 1} - 1 \right) \right] \tag{3.7}$$

By assuming $4G_aW \frac{R_0^{int,therm} + R_0^{int,tunnel} + R_0^b + R_0^{rad}}{(R_0^d)^2} \gg 1$, which is reasonable under open-circuit condition, equation (3.7) can be simplified to:

$$V_{oc} = \frac{k_BT}{q} ln \left[\frac{G_aW}{R_0^{int,therm} + R_0^{int,tunnel} + R_0^b + R_0^{rad}} \right] \tag{3.8}$$

and the activation energy of recombination E_a can be obtained using the formula $V_{oc} = \frac{E_a}{q} + T \cdot \frac{dV_{oc}}{dT}$. Therefore based on the equation (3.8), the E_a is expressed by the following:

$$E_a = \frac{R_0^{int,therm} \varphi_{bo1} + R_0^{int,tunnel} \varphi_{bo2} + (R_0^b + R_0^{rad}) E_g}{R_0^{int} + R_0^b + R_0^{rad}} \tag{3.9}$$

The φ_{bo1}, φ_{bo2} and E_g are the specific recombination activation energies at the p-contact/i-MgCdTe interface through thermionic emission and tunneling, respectively, and in the CdTe absorber/quasi-neutral region. From this point of view, the recombination activation energy E_a is the average activation energy of different recombination processes weighted by respective recombination rates at V = 0.

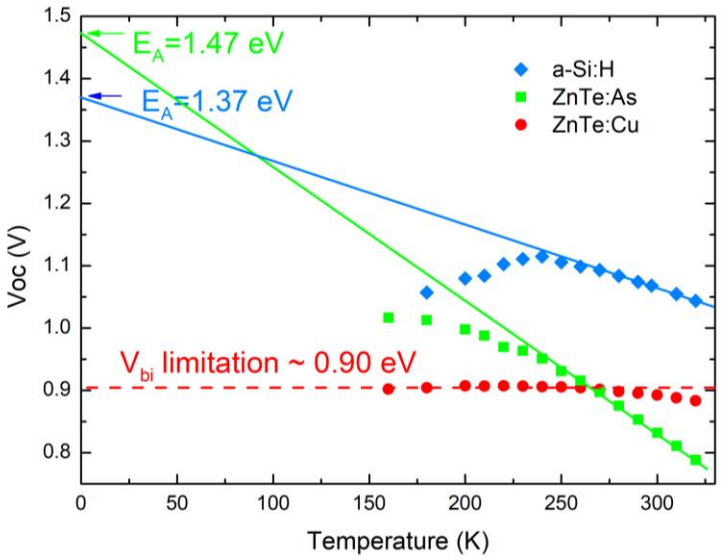

Figure 3.8 Temperature-dependent V_{OC} measurement of CdTe solar cells with a-Si:H, ZnTe:As and ZnTe:Cu under 1 sun illumination. Linear fitting curves are draw based on the V_{OC} near the room temperature.

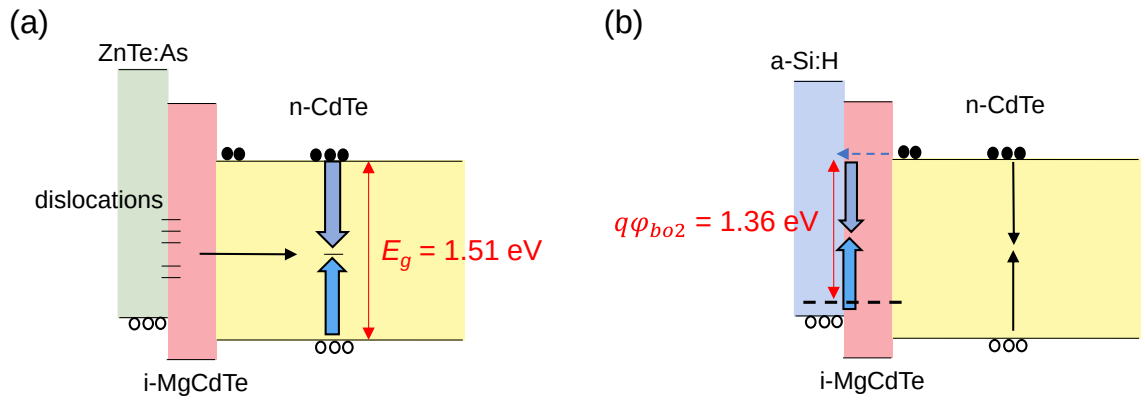

Figure 3.9 Schematic band alignment of CdTe DH solar cells with (a) a ZnTe:As hole contact and (b) an a-Si:H hole contact. The majority recombination mechanisms are illustrated using blue arrows, with corresponding recombination activation energies.

A plot of measured V_{OC} vs. temperature of CdTe DH solar cells at 1 sun illumination is shown in Fig. 3.8. From the measurement, activation energies of CdTe devices with different hole contacts are extracted by using the linear fitting of V_{OC} from near room temperature to 0 K. The schematic band alignment of CdTe DH solar cells with ZnTe:As and a-Si:H hole contacts is depicted in Fig. 3.9. As discussed before, the CdTe DH device

with ZnTe:Cu hole contact is limited by the low V_{bi} of 0.9 V. For devices with ZnTe:As, the activation energy, 1.47 eV, is close to the bandgap of CdTe absorber (1.51 eV), which indicates the recombination in bulk region dominates, further confirms the assumption that interface dislocations introduced by ZnTe layer diffuse into CdTe absorber. For the CdTe devices with a-Si:H, the activation energy, 1.37 eV is close to the energy gap of the tunneling assistant interface recombination, $q\varphi_{bo2}$. This is due to the electron tunneling through the i-MgCdTe barrier, recombing at the a-Si/MgCdTe interface.

3.2.3 Light Intensity Limited

Now it can be concluded that the V_{OC} of CdTe devices with a-Si:H, ZnTe:As and ZnTe:Cu hole contacts are limited by interface recombination, bulk SRH recombination and low V_{bi}, respectively. For CdTe devices under low-injection condition, if the V_{OC} is limited by radiative recombination, it is hard to further optimize V_{OC}, except for increasing light intensity. In this situation, the V_{OC} of solar cells is limited by light intensity.

Actually the radiative recombination dominated CdTe device can be achieved by using a CdTe/$Mg_{0.46}Cd_{0.54}Te$ DH with 30 nm barriers and a heavily-doped p-contact such as a-Si:H. Xin-Hao Zhao *et al*. did temperature-dependent TRPL measurement of a series of CdTe DHs with different MgCdTe barrier height [17]. The results are plotted in Fig. 3.10. Based on the fitting for the samples with 46% Mg in the barrier, the recombination is dominated by radiative recombination at all temperatures. The SRH recombination behaviour is not seen from the fitting, suggesting the very high matieral qualities (at bulk and interfaces). However, the devices based on the CdTe/$Mg_{0.46}Cd_{0.54}Te$ DHs would demonstrate a relatively low FF since the hole thermionic emission overcoming large-bandgap MgCdTe barrier would be blocked. Therefore, even though the larger Mg

composition in the barrier would improve carrier lifetime of the CdTe DHs, there's a trade-off between high V_{OC} and high FF from the device aspect.

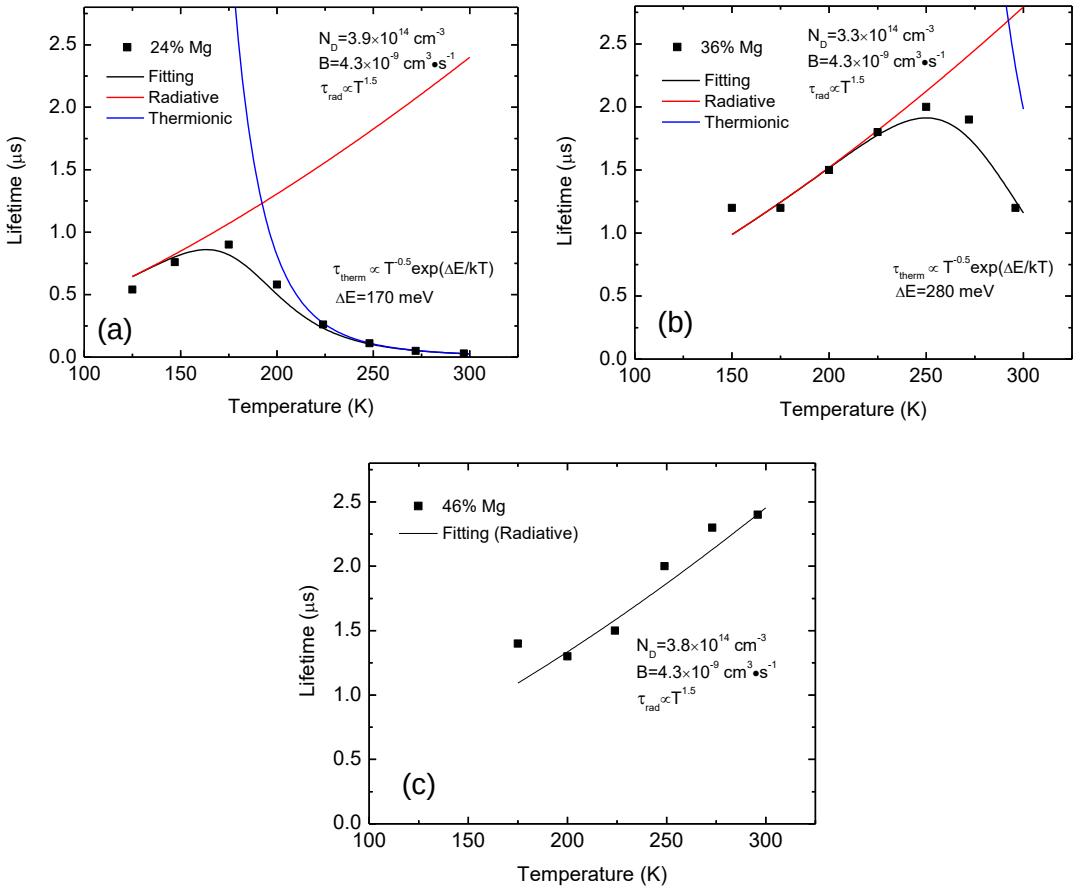

Figure 3.10 Fitting of temperature-dependent carrier lifetime of (a) CdTe/$Mg_{0.24}Cd_{0.76}Te$ DH, (b) CdTe/$Mg_{0.36}Cd_{0.64}Te$ DH and (c) CdTe/$Mg_{0.46}Cd_{0.54}Te$ DH. All the DHs feature 0.5-μm-thick CdTe absorber and 30-nm-thick MgCdTe barriers [17].

CHAPTER 4

EPITAXIAL LIFT-OFF CDTE DOUBLE-HETEROSTRUCTURE THIN FILMS

This chapter reports an improved epitaxial lift-off (ELO) technology for monocrystalline CdTe/MgCdTe double-heterostructure (DH) thin films using water-soluble and nearly-lattice-matched MgTe as a sacrificial layer. Employing hard-baked photoresist as the superstrates with appropriate surface tension, the lift-off thin films show smooth and flat surfaces, confirmed by atomic-force microscopy (AFM) profiles. Photoluminescence (PL) measurements reveal further enhancement of the light extraction from the ELO thin films with a coated Ag back reflective mirror. The increased PL intensity also confirms that the CdTe/MgCdTe DHs maintain high optical quality after ELO. External luminescence quantum efficiency (η_{ext}) is quantitatively measured and used to calculate the implied open-circuit voltage (iV_{OC}). A 0.5-μm-thick lift-off CdTe/MgCdTe DH with a back mirror demonstrates a η_{ext} of 5.35% and an iV_{OC} of 1.152 V. The devices based on this structure are also expected to have an improved fill factor (*FF*) and a short-circuit current density (J_{SC}) of 24.7 mA/cm^2 according to the simulation results, promising to achieve CdTe solar cells with a record power conversion efficiency.

4.1 ELO Process and Sample Structure Design

Flexible thin-film solar cells with a high power density and specific power are highly desirable for both terrestrial and space applications. Epitaxial lift-off (ELO) technology, which enables the development of flexible thin-film solar cells, has been successfully demonstrated for III-V materials and ZnSe based II-VI semiconductors [77–79], using highly selective etchants and sacrificial layers. For the ELO applications to thin film

photovoltaics, like polycrystalline CdTe and $CuIn_xGa_{1-x}Se_2$ (CIGS) solar cells, following the sacrificial layer approach, devices were made on polyimide films by constructing a glass/NaCl/polyimide/CdTe (CIGS) stack and then dissolving the NaCl in water [80,81]. Another ELO method was demonstrated by depositing polycrystalline CdS/CdTe films on Si/SiO_2 substrate, showing a fast lift-off process in water [82]. Even though the thin films can be delaminated automatically, these methods are limited to polycrystalline systems due to the large lattice-mismatch between substrates or sacrificial layers and the epitaxial thin films. Besides the sacrificial layer approach, several mechanical or thermomechanical lift-off methods were reported, such as delaminating CIGS films on a Mo layer and lifting-off CdTe films with a controlled stressor of polymeric handled in liquid nitrogen [83–85]. Although these methods demonstrated novel approaches to delaminate high-quality polycrystalline thin films, there is no report on the ELO process of high-quality monocrystalline CdTe devices.

Recently, a new ELO method for monocrystalline CdTe thin films was reported using MgTe as a sacrificial layer [86–88]. High-quality CdTe/MgCdTe double-heterostructure (DH) and MgTe can be grown on nearly-lattice-matched InSb substrate by using molecular-beam epitaxy (MBE). The sacrificial layer, MgTe, is water-soluble, while both the DH and the substrate have extremely low etching rates in deionized (DI) water. Therefore, this ELO method is promising to obtain high-quality monocrystalline DH thin films. Since only water is used during the ELO process, the substrate is intact and can be reused almost indefinitely, without the need for repolishing. Furthermore, the wide-bandgap MgCdTe barriers serve as carrier selective barriers and passivation layers to the CdTe absorber. Therefore, the lift-off MgCdTe surface is expected to have little impact on

the effective minority carrier lifetime of the CdTe DH [11]. To enhance the light extraction and photon-recycling effect, a back reflective mirror can be added. With a back mirror, the necessary absorber thickness can be reduced to approximately half of the original value, leading to decreased total SRH recombination current density, increased V_{OC}, and nearly the same J_{SC}. A similar approach has been successfully used to demonstrate thin-film GaAs solar cells with a record efficiency of 29.1% [89]. For the previous study of MgTe-based ELO [88], Kapton tape was used as the superstrate, attaching to the top surface of the sample. By submerging the sample in DI water, the thin film was lifted off with the tape. Although the process was successful, the Kapton tape is not an ideal superstrate since the tape makes the thin film develop wrinkles and defects during the ELO process, and thus giving much lower PL intensity in the center area and broadened CdTe peak in the XRD pattern. The strong PL signals observed at the lift-off thin film edges are attributed to the luminescence concentration as the film acts as an efficient waveguide. In this work, hard-baked photoresist is used as superstrate to supply more rigid support to the thin film during the ELO process, as well as needed surface tension that enables the reaction products of the thin MgTe with DI water to diffuse out from the etching fronts and let the etching continue.

The basic process of MgTe-based ELO conducted in this study is depicted in Fig. 4.1. Upon removal from MBE chamber, each sample is coated with photoresist and then moved to a hot plate for hard bake. Several layers of photoresist are coated to achieve appropriate amount of tension. The sample is then immersed in DI water. MgTe is dissociated, and the

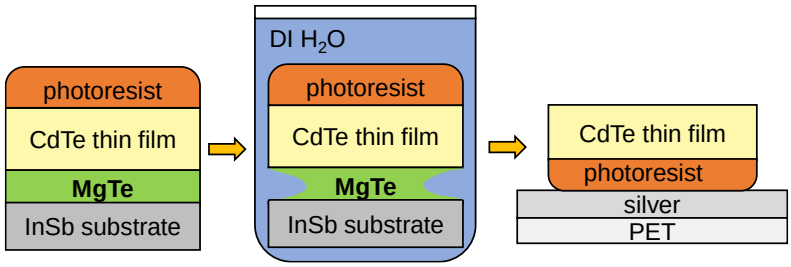

Figure 4.1 Schematic ELO process of CdTe/MgCdTe DH, using photoresist as the superstrate.

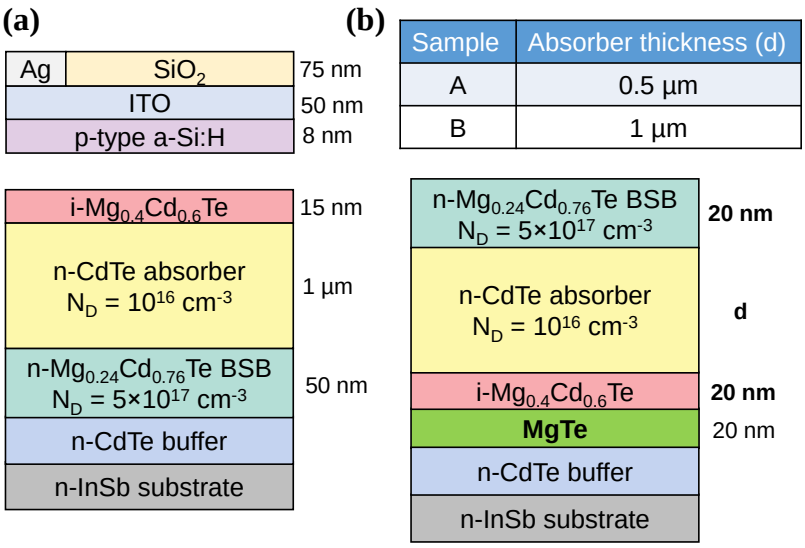

Figure 4.2 (a) Layer structure of the conventional CdTe/MgCdTe DH solar cells design. (b) Layer structures of newly designed CdTe lift-off samples with MgTe sacrificial layers.

CdTe thin film with photoresist is lifted off. Typically, the process takes about 15 minutes to lift off a 1 cm × 1 cm thin film from the substrate in 55˚C DI water. The free-standing thin film is then transferred to a foreign substrate, a polyethylene terephthalate (PET) coated with Ag as a reflective mirror. To fabricate thin-film solar cells in the future, it is planned to use indium to bond the CdTe lift-off samples with conductive PET substrates before the lift-off process [27], or to use an elastomer, like PDMS, as the superstrate to lift off, transfer and print the thin films [90,91].

Fig. 4.2 (a) shows the layer structure of a conventional CdTe/MgCdTe DH solar cell design, which exhibits a record V_{OC} up to 1.11 V [25,26]. The CdTe lift-off samples in this study, which is shown in Fig. 4.2 (b), are designed with a reversed layer sequence to be compatible with the ELO process mentioned above. Except for the layer sequence, the changes of the new designs are i) the thickness of i-$Mg_{0.4}Cd_{0.6}Te$ barrier was increased from 15 nm to 20 nm to minimize electron tunneling and consequent p-contact/i-$Mg_{0.4}Cd_{0.6}Te$ interface recombination [17,48]; ii) the thickness of n-$Mg_{0.24}Cd_{0.76}Te$ barrier was decreased from 50 nm to 20 nm to reduce the parasitic absorption considering the light reflection from the back mirror; iii) two structures A and B feature the different absorber thickness of 0.5 μm and 1 μm, respectively.

4.2 Characterization of Structural and Surface Properties

To illustrate the crystalline properties of the lift-off thin films and the successful ELO process, (004) ω-2θ XRD scans of structure A both pre-ELO (top) and post-ELO (bottom) are shown in Fig. 4.3. Compared to the pre-ELO scan, the post-ELO scan shows that both the MgTe peak at 29° and the InSb substrate peak are absent while the CdTe absorber peak and the features corresponding to the $Mg_{0.24}Cd_{0.76}Te$ and $Mg_{0.4}Cd_{0.6}Te$ barriers remain. Full width at half maximum (FWHM) of the CdTe absorber peak does not change significantly after the ELO. These findings indicate a successful ELO of the CdTe DH thin films with the assistant of photoresist.

After the ELO, the i-$Mg_{0.4}Cd_{0.6}Te$ layer, which passivates the CdTe absorber and serves as an electron blocking layer, is exposed to the air. If this layer reacts with DI water due to the 40% composition of Mg in MgCdTe during the ELO process, the enhanced

surface recombination would lead to low optical performance of the thin film, even though the crystalline quality remains unchanged [9,17]. To confirm the DH, especially the i-$Mg_{0.4}Cd_{0.6}Te$ layer is intact after the ELO, the i-$Mg_{0.4}Cd_{0.6}Te$ surface morphology of post-ELO thin film with structure B is characterized by atomic-force microscopy (AFM). A 5 μm × 5 μm range image is shown in Fig. 4.4, with a root mean square (RMS) roughness of 6.69 Å, similar to that obtained on an epitaxial layer surface, suggesting the extremely low etching rate of i-$Mg_{0.4}Cd_{0.6}Te$ in DI water.

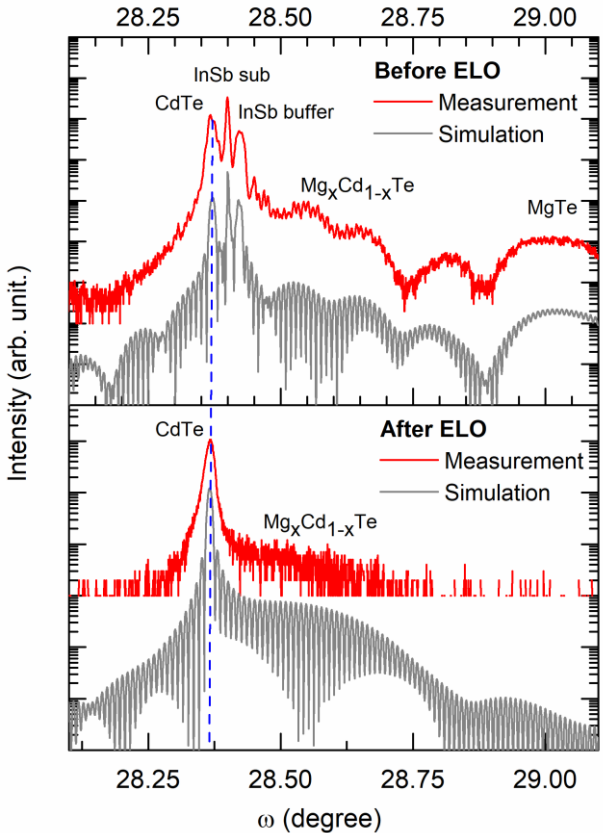

Figure 4.3 Omega-2θ (004) scans of (top) as-grown sample A on an InSb(001) substrate and (bottom) the free-standing CdTe/MgCdTe DH thin film after ELO.

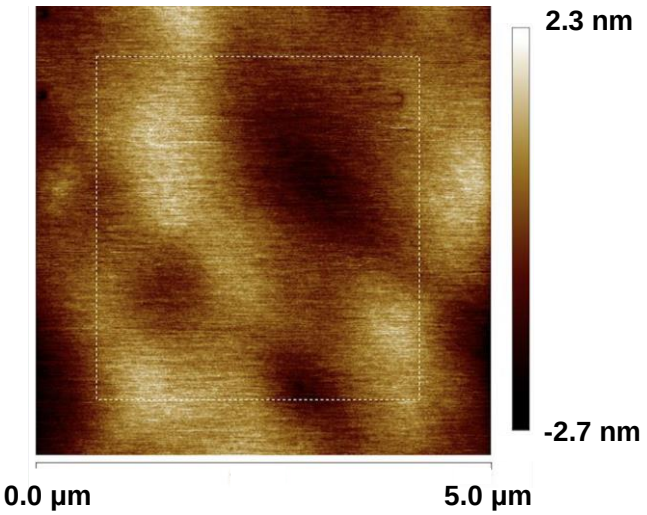

Figure 4.4 AFM image of i-$Mg_{0.4}Cd_{0.6}Te$ surface morphology of post-ELO thin film with structure B in 5 µm × 5 µm range.

4.3 Characterization and Simulation of Optical Performance

The optical performance of the as-grown samples and post-ELO thin films is firstly characterized by using room-temperature PL spectroscopy. The laser wavelength is 532 nm, with a penetration depth in CdTe absorber smaller than 0.1 µm. Fig. 4.5 (a) compares the PL of a conventional CdTe DH sample and the lift-off samples with structures A and B before ELO. Compared with the conventional CdTe DH sample, the lift-off samples give stronger PL signals because the thicker i-$Mg_{0.4}Cd_{0.6}Te$ barrier further suppresses the tunneling of the photogenerated carriers from the absorber to the surface to recombine non-radiatively [17,48]. With a thinner absorber, the lift-off sample with structure A shows even higher PL intensity than structure B due to a higher photon-generated carrier density per unit volume and lower total SRH non-radiative recombination rate per unit area. In Fig. 4.5 (b), stronger PL intensities in the post-ELO films than those in the as-grown lift-off samples are observed. This shows that the light extraction and photon-recycling effect of

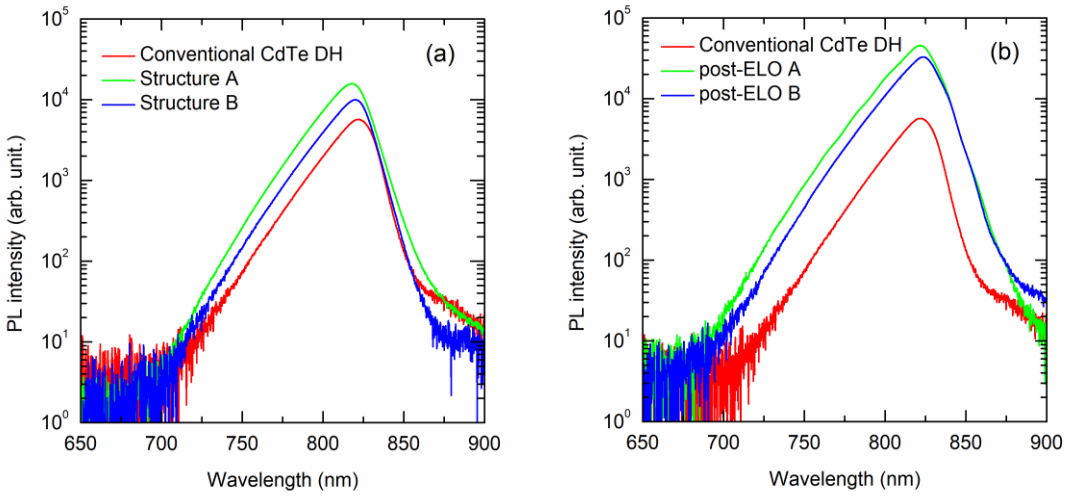

Figure 4.5 (a) Comparison of the PL spectra between conventional CdTe DH sample and as-grown CdTe lift-off samples with structure A and B. (b) Comparison between conventional CdTe DH sample and free-standing thin films of structure A and B with Ag back mirror.

the CdTe thin films have been enhanced by replacing absorptive substrate with a reflective back mirror. Increased PL intensity is observed across the sample areas of the post-ELO films.

In addition to PL spectra, photoluminescence quantum efficiency (PLQE) measurements are performed, and external luminescence quantum efficiency (η_{ext}) are quantitatively measured. More details about the experimental procedures and theoretical analysis can be found in previous publication [24]. Through the formula [22,23]

$$iV_{OC} = V_{OC,ideal} - \frac{kT}{q}|\ln(\eta_{ext})| \tag{5.1}$$

the implied open-circuit voltage (iV_{OC}) of a solar cell, or the quasi-fermi-level splitting in the absorber region, can be measured, where η_{ext} is the ratio of photons that escape from the front surface to the electron-hole pairs generated in the solar cell absorber; $V_{OC,ideal}$ is the V_{OC} of a solar cell when the recombination is purely radiative, emittance to the back-

surface is zero, and zero voltage loss due to carrier transport. The results are summarized in Table 4.1.

Table 4.1 Summary of PLQE measurement results. SC design represents conventional monocrystalline CdTe DH solar cell design.

Sample	η_{ext} at 1 sun	iV_{OC} (V)	V_{OC} (V)
SC design	1.54%	1.119	1.11 [27]
structure A	3.65%	1.141	-
structure B	1.80%	1.123	-
ELO A	5.35%	1.152	
ELO B	3.39%	1.139	

One of the key factors to make a precise calculation of the iV_{OC} is the accurate estimation of light absorption, i.e., the number of carriers optically injected into the CdTe absorber. Different structures with different smooth/textured surfaces, absorptive/reflective substrates, and reflective index, etc. would have different absorption. A total of 12 kinds of statistical ray tracing models are presented in the previous studies [92,93], assuming the maximal scattering case with an angular Lambertian distribution. For the MBE grown samples and post-ELO thin films with smooth surfaces and interfaces, the absorption of CdTe absorber at the laser wavelength can be accurately simulated by wave optics, taking into account of the optical constants (refractive index, n, and extinction coefficient, k) and the thickness of each layer. One example is that the measured iV_{OC} of the conventional CdTe DH samples was in excellent agreement with the V_{OC} of the processed solar cells [26]. In the light absorption simulation of the ELO thin films above, however, the absorption of photoresist is ignored. Therefore, the calculated iV_{OC} values of the ELO films are underestimated. Based on the measurements, ELO thin films with 0.5-μm-thick

absorber (ELO A) demonstrated a η_{ext} of 5.35% and an iV_{OC} of 1.152 V. Using the same processing flow of the conventional CdTe DH solar cells, the CdTe thin-film solar cells based on structure A would achieve a V_{OC} of 1.15 V or even higher.

Compared with the conventional CdTe DH solar cell design, a thin-film solar cell with 0.5-μm-thick absorber would maintain a similar J_{SC} by incorporating a 150-nm-thick Ag layer as back mirror. The simulated structure is SiO_2/ITO/a-Si:H/CdTe DH (structure A)/Ag/PET. Fig. 4.6 depicts the simulated absorption of the thin-film solar cells with a calculated photo-current density of 24.7 mA/cm^2 using wave optics. By optimizing the p-contact to reduce the parasitic absorption, such as depositing a thinner a-Si:H layer with higher doping density, or replacing the a-Si:H with a wider-bandgap material, the J_{SC} of thin-film solar cells can be further improved.

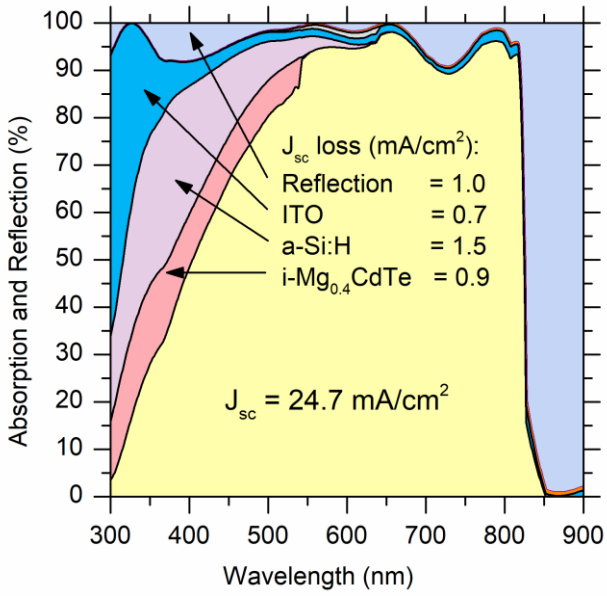

Figure 4.6 Simulated absorptance spectrum for CdTe thin-film solar cells with a calculated photo-current density of 24.7 mA/cm^2. The simulated device (structure A) has a 75-nm-thick SiO2 anti-reflection coating layer, a 55-nm-thick ITO layer, an 8-nm-thick a-Si:H hole-contact layer and a 150-nm-thick Ag back contact.

In summary, a photoresist-assisted ELO method is demonstrated to obtain high-quality monocrystalline CdTe DH thin films with smooth lift-off surface and enhanced optical performance. A maximum η_{ext} of 5.35% is extracted from a newly designed, 0.5-μm-thick CdTe/MgCdTe DH after ELO process, corresponding to an iV_{OC} of 1.152 V, which is only 0.35 V below the bandgap of monocrystalline CdTe. By incorporating the back reflective mirror to increase the optical thickness and photo-recycling effect, the J_{SC} of a processed 0.5-μm-thick CdTe thin-film solar cell is 24.7 mA/cm^2 according to simulation.

4.4 Roadmap and Demonstration of CdTe Thin-Film Devices

Due to the lack of the lift-off samples, the monocrystalline CdTe thin-film solar cells have not been developed yet. This section introduces some preliminary results and gives a summary of the envisioned possibility methods to fabricate the monocrystalline CdTe DH thin-film solar cells.

4.4.1 Device Processing Prior to ELO

One of the methods is growing lift-off samples with normal CdTe DHs. As shown in Fig. 4.7, p-type hole contact, ITO and Ag layers are deposited on top of the lift-off samples. Then do the ELO after the device processing. When the lift-off sample with the hole contact, ITO and Ag is immersed into water, the thin film can be automatically lifted off. The obtained freestanding thin films are flipped over and deposited indium contact on the other side. By laying the p-type hole contact and ITO layers down to the bottom, the parasitic absorption of these layers can be avoided. The Ag layer can serve as a back reflective mirror to increase the photon-recycling effect and the light extraction efficiency.

Another advantage is that depositing p-contact on the MBE-grown CdTe DH surface is better than that on the lift-off surface in the wafer scale.

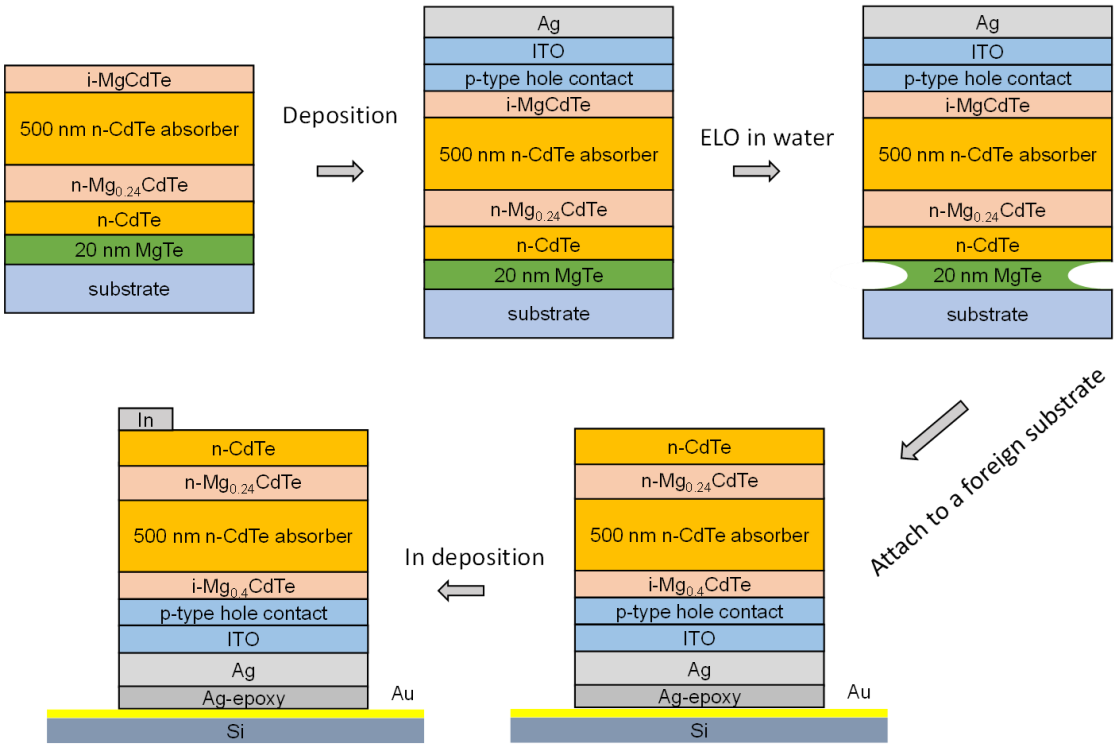

Figure 4.7 Monocrystalline CdTe thin-film solar cell processing flow using a normal structure CdTe lift-off sample. The deposition of the p-type hole contact, ITO and Ag are done before the ELO process.

However, this method does not work when the p-type a-Si:H is used as the hole contact. The reason is that the a-Si:H layer can not form a tight bonding with the CdTe DHs. During the ELO process, the a-Si:H with the ITO and Ag layers would be first separated with the CdTe DH. The obtained freestanding thin film does not have PL signals in the visible light range, while the PL peak corresponding to the CdTe absorber can be observed from the substrate after the ELO. By attaching a Kapton tape on the substrate, a second ELO can be done. After the second ELO, another layer of thin film is separated from the substrate, and no PL signal can be observed on the substrate. The spectra of the

as-grown sample, the freestanding thin film after first ELO, the substrate after the first and the second ELO are plotted in Fig. 4.8. To use this method in the future, other p-type hole contacts with tight bonding with the CdTe DHs should be deposited on the lift-off samples.

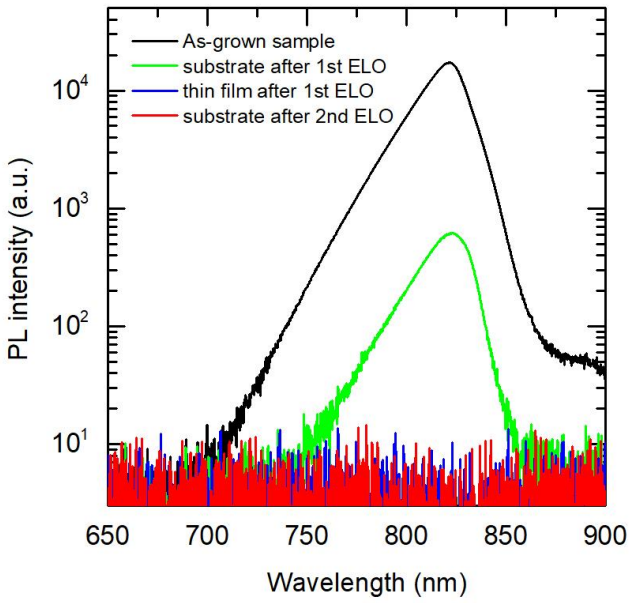

Figure 4.8 Photoluminescence spectra of the as-grown CdTe lift-off sample, freestanding thin film after the first ELO and the substrate after the first and the second ELO.

4.4.2 Device Processing Post ELO

Another idea is growing reversed structure of the lift-off samples, as shown in Fig. 4.2 (b), and doing the device processing after the ELO process. The schematic processing flow is demonstrated in Fig 4.9. Using this method, the key is finding a conductive and adhesive layer to bond the reversed lift-off structure to a superstrate. Several promising bonding technologies will be discussed. During the a-Si:H deposition via PECVD, the samples will stay in the chamber at 220 ˚C for 4 ~ 5 minutes. To be compatible with the device processing, the conductive bonding layer and the superstrate are required to withstand the

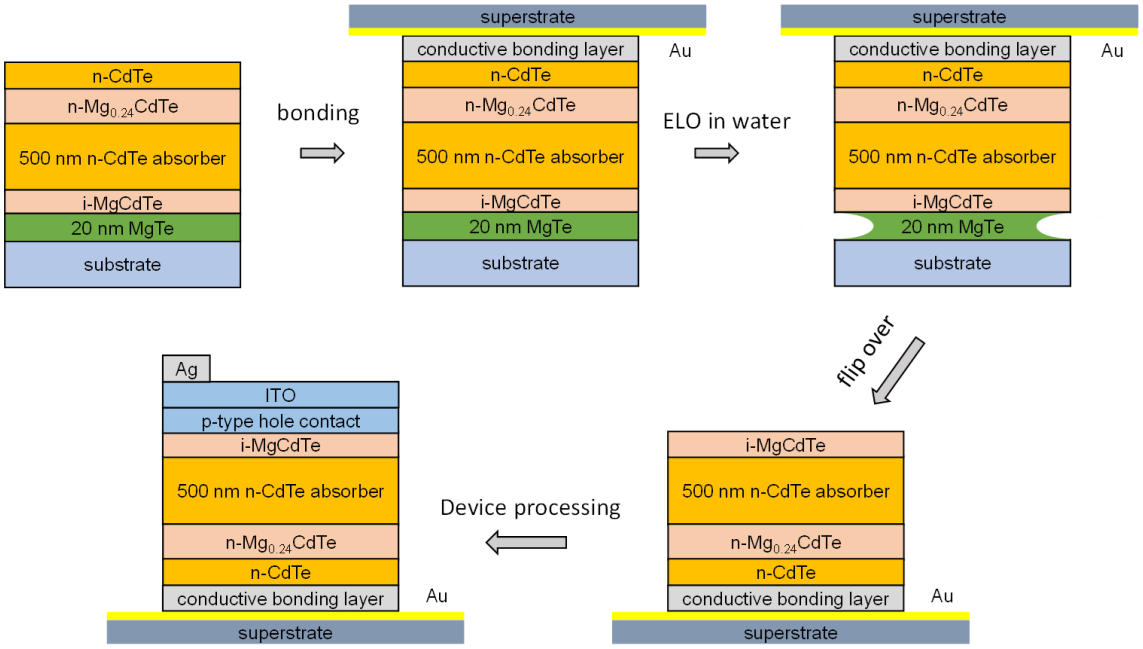

Figure 4.9 Monocrystalline CdTe thin-film solar cell processing flow using a reversed structure CdTe lift-off sample. The deposition of the p-type hole contact, ITO and Ag are done before the ELO process.

temperature of 220 ˚C. For the flexible polymer superstrate, polyimide is a good candidate which is commercially available and can withstand temperatures ranging from -269 ˚C to 400 ˚C.

For the bonding technology, one promising method is using Ag epoxy to form In/Ag-epoxy/Au contact. As mentioned in Chapter 2, In can make good ohmic contact to n-CdTe with resistance of 1.2×10^{-4} Ω·cm^2. A previous study is reported using Ag-epoxy agent to bring InAs/GaAs quantum dot solar cell wafer and polyimide film into contact [94]. No degradation was observed of the bonding layer and the plastic film after annealing at 150 – 200 ˚C in ambient air and selective chemical etching with H_3PO_4/H_2O_2 followed by 50% citric acid/H_2O_2.

Indium bonding is a promising method as well. Weiquan Yang *et al.* demonstrated an ultra-thin GaAs single-junction solar cell by using indium as bonding medium to secure the GaAs wafer to the Si carrier in 2014 [27]. After the chemical etching of the GaAs substrate using HF/H_2O solution, the indium bonding layer keeps good electrical property and the fabricated GaAs thin-film solar cell demonstrated a *FF* of 77.8% and a power conversion efficiency of 19.1%. One potential problem is the low melting point of indium (156 ˚C). The stability of the indium bonding layer during the deposition of a-Si:H layer at 220 ˚C should be further investigated.

Another promising bonding method is cold-weld bonding [95]. A previous study demonstrated an ELO technology for single-crystal InP thin-film solar cells by mounting the InP sample to a flexible plastic superstrate [96]. The sample and the plastic sheet were deposited a 60 nm Au contact layer. By mounting the InP wafer Au-side down on the plastic sheet and applying a pressure of 10 MPa for 60 s, a cold-weld bond is formed between the wafer and the superstrate. After that, a selective chemical etching was used to remove the InP substrate and the InP thin film was obtained with the conductive bonding layer and the flexible superstrate.

4.4.3 CdTe DH thin-film solar cells

After removal from the MBE chamber, the CdTe ELO sample is deposited a 900 nm indium layer on top surface by thermal evaporation. Ti/Pt/Au layers are deposited onto a 127 μm Kapton polyimide film with 30 nm, 20 nm and 150 nm thickness, respectively, by electron-beam evaporation. A 900 nm indium layer is then deposited on the polyimide film by thermal evaporation.

After metal deposition, the ELO sample is mounted indium-side down on the polyimide film and a indium bonding layer is formed by applying pressure through a flat stage for several minutes at room temperature. Then, the CdTe ELO sample with the polyimide superstrate is immersed into 65 ˚C DI water. The lift-off process takes about 2 minutes to lift off a 5 mm × 5 mm thin film without any external force.

After obtaining the CdTe DH thin film with the polyimide film, a 50 nm thick ITO layer with 0.005 cm^2 area is sputtered onto the thin film using shadow mask. The ITO layer is considered as the current spreading layer and therefore, the device area is approximated as the area of the ITO. The device structure and the *J-V* curve are shown in Fig. 4.10. For device performance, the lift-off CdTe thin-film solar cell demonstrates an V_{OC} of 0.792 V and an efficiency of 9.8%. The low FF of 44.9% is mainly attributed to the large contact resistance between the probe and the ITO layer. In the future, a silver layer will be deposited on top of the ITO, serving as the metal contact to minimize the contact resistance.

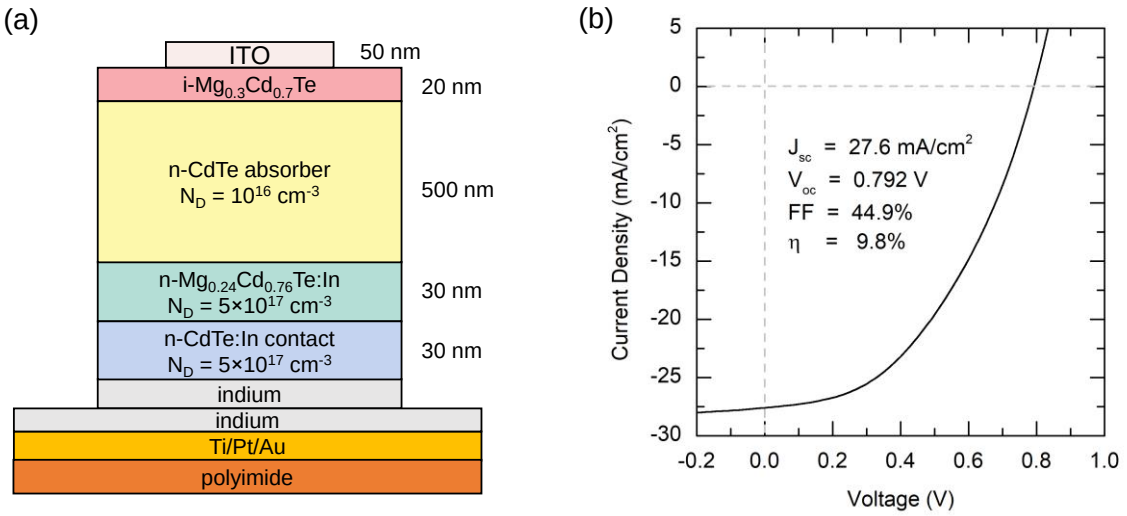

Figure 4.10 (a) Layer structure of the monocrystalline CdTe DH thin-film solar cell. (b) *J-V* curve of the processed CdTe DH thin-film solar cell.

This device structure does not employ a hole contact. The V_{OC} is believed to come from the Schottky junction between ITO and i-MgCdTe barrier due to the interface Fermi-level pinning [97,98]. This result shows a promising method to fabricate high-efficient CdTe Schottky solar cells. It also reveals a possibility for polycrystalline CdTe solar cells to achieve high V_{OC} by forming the Schottky junction.

CHAPTER 5

MONOCRYSTALLINE 1.7-EV MGCDTE SOLAR CELLS

A two-terminal, current-matched tandem solar cell combining a 1.7-eV bandgap top subcell with a 1.1-eV bandgap silicon, perovskite, or CIGS bottom subcell has a theoretical conversion efficiency up to 43% [92]. The desired top subcell bandgap of 1.7 eV can be achieved using MgCdTe alloy with 13% Mg composition. Compared with III-V semiconductors and perovskites [99–102], $Mg_{0.13}Cd_{0.87}Te$ is stable, low-cost, radiation-hard [103,104] and has a high absorption coefficient near the band edge [105], making it an excellent candidate for the top subcell. Following the "remote junction" design of monocrystalline CdTe solar cells with a p-type a-Si:H layer outside a CdTe/MgCdTe double heterostructure (DH) [25,26], high quality $Mg_{0.13}Cd_{0.87}Te/Mg_xCd_{1-x}Te$ ($x > 0.13$) DHs are designed and grown on nearly lattice-matched InSb(001) substrates using molecular beam epitaxy (MBE). The $Mg_{0.13}Cd_{0.87}Te/Mg_xCd_{1-x}Te$ DHs exhibit a minority carrier lifetime longer than 500 ns, promising to achieve a single-junction 1.7-eV solar cell with high open-circuit voltage (V_{OC}) and power conversion efficiency [106]. For tandem solar cell applications, an epitaxial lift-off (ELO) technology has recently been reported for monocrystalline CdTe DH thin films employing water-soluble MgTe as a sacrificial layer [107,108]. Incorporating the ELO technology with 1.7-eV MgCdTe DH solar cells offers the promise of MgCdTe/Si or MgCdTe/CIGS tandem solar cells with robust radiation hardness, high power conversion efficiency, and high power density.

The previous study demonstrated a 1.7-eV MgCdTe DH solar cell with an efficiency of 11.2% limited by poor carrier transport and low light absorption [106]. In this work, an anti-reflective coating (ARC) layer and a thicker absorber are employed to increase the

light absorption. Carrier transport studies are conducted on these solar cells with varying $Mg_xCd_{1-x}Te$ barrier height and thickness to optimize the trade-off between carrier confinement and carrier transport. The limiting factors of the V_{OC} and the suppression of short-circuit current density (J_{SC}) are further analyzed using temperature-dependent V_{OC} measurements and solar cell absorption simulations.

5.1 Device Structure and Characterization

The layer structure of the 1.7-eV MgCdTe DH solar cells studied in this work is shown in Fig. 5.1 and consists of a MBE-grown, unintentionally doped $Mg_{0.13}Cd_{0.87}Te/Mg_xCd_{1-x}Te$ ($x > 0.13$) DH on a n-type InSb(001) substrate, an 8 nm thick p-type a-Si:H hole contact layer with a doping concentration of approximately 1×10^{18} cm^{-3}, a 50 nm thick indium tin oxide (ITO) current spreading layer, a Ag top contact, and a 75 nm thick SiO_2 ARC layer. The unintentionally doped intrinsic $Mg_{0.13}Cd_{0.87}Te$ absorber shows n-type behavior with an electron concentration of 10^{15} cm^{-3}. More details of the device design and processing can be found in a previous publication [25]. This design takes advantage of the "remote junction" structure in which the top $Mg_xCd_{1-x}Te$ layer serves as a passivation layer for the absorber as well as a barrier for the photogenerated electrons, preventing them from reaching non-radiative recombination centers in the a-Si:H hole contact layer. The recombination rates at the nearly lattice-matched $Mg_xCd_{1-x}Te/Mg_{0.13}Cd_{0.87}Te$ interfaces are greatly suppressed as a result of very low defect density and the low electron density at the a-Si:H/$Mg_xCd_{1-x}Te$ interface. Therefore, long minority carrier lifetime and high V_{OC} have been achieved.

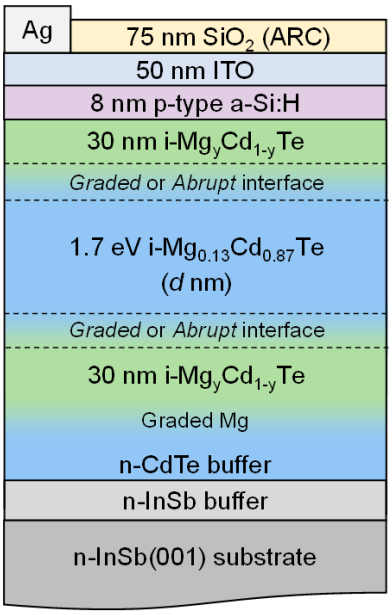

Figure 5.1 Schematic layer structure of the 1.7-eV MgCdTe DH solar cells. The details of $Mg_{0.13}Cd_{0.87}Te$ absorber thickness (d), Mg composition in the $Mg_xCd_{1-x}Te$ barrier layers, interface type between absorber and barriers, and ARC layer are listed in Table I.

Table 5.1 Barrier composition, absorber layer thickness, and absorber/barrier interface type for 1.7-eV MgCdTe DH solar cells.

Sample structures	$Mg_xCd_{1-x}Te$ barrier	Absorber thickness	Absorber interfaces	ARC layer
A	2.4 eV $Mg_{0.50}Cd_{0.50}Te$	0.50 µm	Graded	No
B	2.2 eV $Mg_{0.37}Cd_{0.63}Te$	1.2 µm	Graded	Yes
C	2.2 eV $Mg_{0.37}Cd_{0.63}Te$	1.2 µm	Abrupt	Yes
D	2.0 eV $Mg_{0.28}Cd_{0.72}Te$	1.2 µm	Abrupt	Yes

Table 5.1 lists the four $Mg_{0.13}Cd_{0.87}Te/Mg_xCd_{1-x}Te$ DHs grown and studied in this work. Structure A is a previously studied design with an absorber thickness of 0.5 µm [106]. It features two 30 nm 50% Mg (E_g = 2.4 eV) barriers with a 36 nm graded layer between the absorber and each barrier. Devices based on structure A demonstrated an V_{OC} of 1.176 V and an active-area efficiency of 11.2%. Structures B - D are newly designed structures

with a 1.2 μm thick absorber and an additional 75 nm SiO_2 ARC layer. Structures B and C feature two 30 nm 37% Mg (E_g = 2.2 eV) barriers with a 36 nm graded layer and an abrupt interface between the absorber and each barrier. Structure D features two 30 nm 28% Mg (E_g = 2.0 eV) barriers with abrupt interfaces. From structure A to D, the samples trend towards lower barrier height of the $Mg_xCd_{1-x}Te$ layers.

Current-voltage (*J-V*) measurements are performed using a AM1.5G solar simulator at room temperature for all four solar cell structures A, B, C and D. Fig. 5.2 compares the V_{OC}, J_{SC}, fill factor (*FF*), and power conversion efficiency (η) of these devices. The V_{OC} values of these samples trend down with the lowering barrier height. Higher $Mg_xCd_{1-x}Te$ barriers result in increased confinement of the photogenerated electrons and holes in the $Mg_{0.13}Cd_{0.87}Te$ absorber. Non-radiative recombination outside the DH is thus suppressed and the effective carrier lifetime, quasi-Fermi level splitting, and V_{OC} are thereby increased. Comparing structures B and C demonstrates that the abrupt interface between $Mg_xCd_{1-x}Te$ top barrier and $Mg_{0.13}Cd_{0.87}Te$ absorber gives weaker carrier confinement than the interface with graded layer and thus leads a lower V_{OC}. The increased J_{SC} in structures B, C and D in comparison to A is attributed to two factors: i) the thickness of the absorber from 500 nm (A) to 1200 nm (B-D); and ii) the addition of the 75 nm SiO_2 ARC layer. It is worth noting that the measured J_{SC}, and consequently η, of structure C has a large error bar due to the uncertainty of device area measurements.

The *FF* increases from structure A to D. This trend is inversely proportional to the barrier height and thickness of the $Mg_xCd_{1-x}Te$ layers. The barriers in the conduction band near the electron contact and in the valence band near the hole contact are thought to be responsible for restricting electron and hole transport to their respective contacts. The

reduction in barrier height and thickness leads to improved carrier transport across the barrier layers and thus a higher *FF*. The selection of $Mg_xCd_{1-x}Te$ barrier height and thickness is a trade-off between the $V_{OC,}$ associated with carrier confinement, and *FF*, associated with carrier transport. The 1.7-eV MgCdTe devices with structure C demonstrate the best performance in terms of total conversion efficiency. As discussed earlier, the measured J_{SC} has a large error bar. Therefore we report the calibrated J_{SC} for the record cell by integrating the external spectrum over wavelength. The scaled J_{SC} is used to calculate the active-area efficiency [26] of the device, which gives an efficiency of 15.2%. The corresponding *J-V* curve and EQE spectrum are shown in Fig. 5.3. It is noted

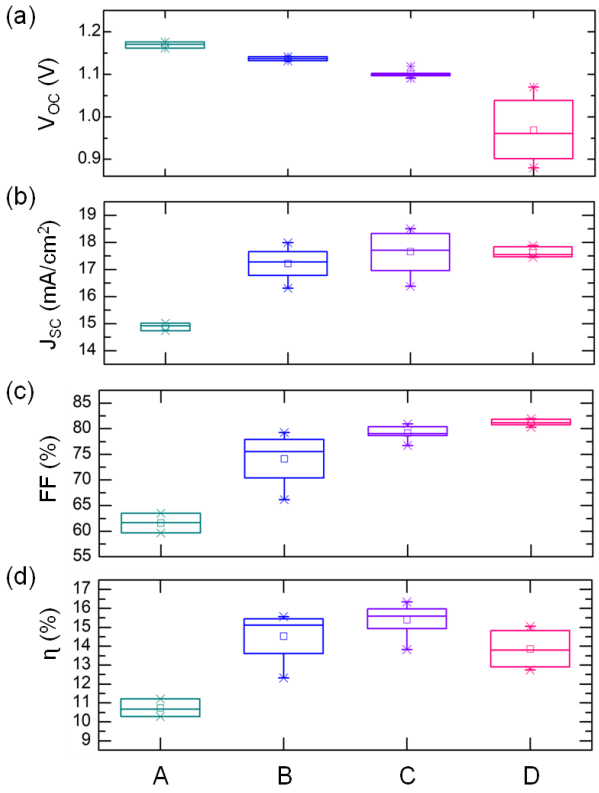

Figure 5.2 (a) Open-circuit voltage V_{OC}, (b) short-circuit current J_{SC}, (c) fill factor *FF*, and (d) power conversion efficiency η of 1.7-eV MgCdTe DH solar cell structures A – D. From structure A to D, the samples trend towards lower barrier height of the $Mg_xCd_{1-x}Te$ layers.

that if this cell is integrated with a 21.2% efficiency Si solar cell [109] by a two-terminal connection, a boost of efficiency to 24% is expected based on our simulation results shown in Table 5.2, demonstrating the great potential of two-terminal MgCdTe/Si tandem solar cells proposed in the introduction.

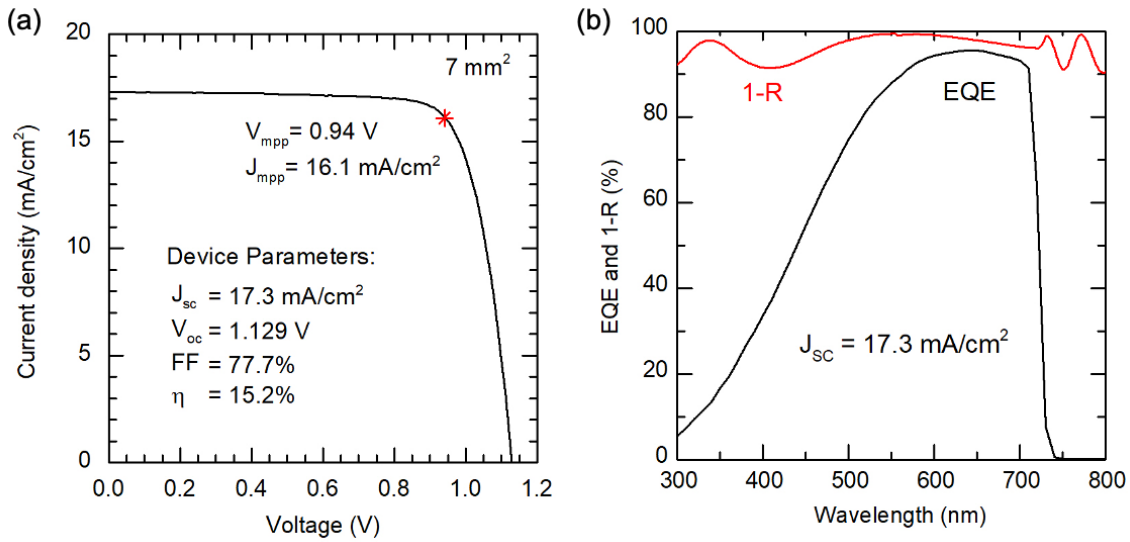

Figure 5.3 (a) *J-V* curve of the 1.7-eV MgCdTe device with structure C. The current density is scaled to match the J_{SC} calculated from the EQE spectrum. (b) Measured EQE and one minus reflectance (1-R) of the device with structure C.

TABLE 5.2 *J-V* parameters of the 1.7-eV MgCdTe solar cell, a Si subcell and a simulated two-terminal tandem solar cell of MgCdTe device and Si subcell under AM1.5G illumination. V_{mpp} and J_{mpp} refer to the maximum power point voltage and current density, respectively.

Devices	V_{OC} (V)	J_{SC} (mA/cm^2)	FF (%)	Efficiency (%)	V_{mpp} (V)	J_{mpp} (mA/cm^2)
1.7-eV MgCdTe	1.129	17.3	77.7	15.2	0.94	16.1
Si subcell [103]	0.687	38.5	80.3	21.2	0.585	36.29
Tandem				24.3	1.49	16.31

5.2 Temperature Dependent V_{OC} Study

Temperature-dependent measurements of the V_{OC} are conducted to study carrier transport and the limitations to the V_{OC}, and to determine the major recombination mechanisms in the devices. The measurement data are analyzed using a model described as follows: The radiative recombination rate (R^{rad}) in the $Mg_{0.13}Cd_{0.87}Te$ absorber, the Shockley-Read-Hall (SRH) recombination rates in the depletion region (R^{d}_{SRH}) and in the quasi-neutral region (R^{qn}_{SRH}), and the effective interface recombination rate (R^{int}) either in the a-Si:H hole contact layer (case I) or at the a-Si:H/$Mg_xCd_{1-x}Te$ interface (case II) are quantified, and these recombination processes are considered as the potential main recombination mechanisms. Recombination at the $Mg_xCd_{1-x}Te/Mg_{0.13}Cd_{0.87}Te$ interface is neglected due to the nearly lattice-matched interface with very low defect density [17]. Fig. 5.4 shows the energy band diagram of a MgCdTe DH device with different recombination mechanisms. Fig. 5.4 (a) features $Mg_xCd_{1-x}Te$ barrier layers with greater Mg composition and a higher barrier while Fig. 5.4 (b) features $Mg_xCd_{1-x}Te$ barrier layers with smaller Mg composition and lower barrier. Each recombination rate under illumination is expressed as the product of a voltage-independent recombination coefficient and an exponential function of voltage as follows [22,43,59,60]:

$$R^{int} = \begin{cases} \frac{d}{\tau_{e,p}} \frac{n_{i,p}^2}{N_A} \cdot e^{\frac{qV}{k_B T}} & \text{(case I)} \\ S_e N_C e^{-\frac{q\varphi_{bo}}{k_B T}} \cdot e^{\frac{qV}{k_B T}} & \text{(case II)} \end{cases} \cong R_0^{int} e^{\frac{qV}{k_B T}} \qquad (5.1)$$

where d, $\tau_{e,p}$, $n_{i,p}$ and N_A are the thickness, minority carrier lifetime, intrinsic carrier concentration and doping concentration of the hole contact, respectively. S_e is the interface recombination velocity, N_C is the effective density of states of the conduction band in the

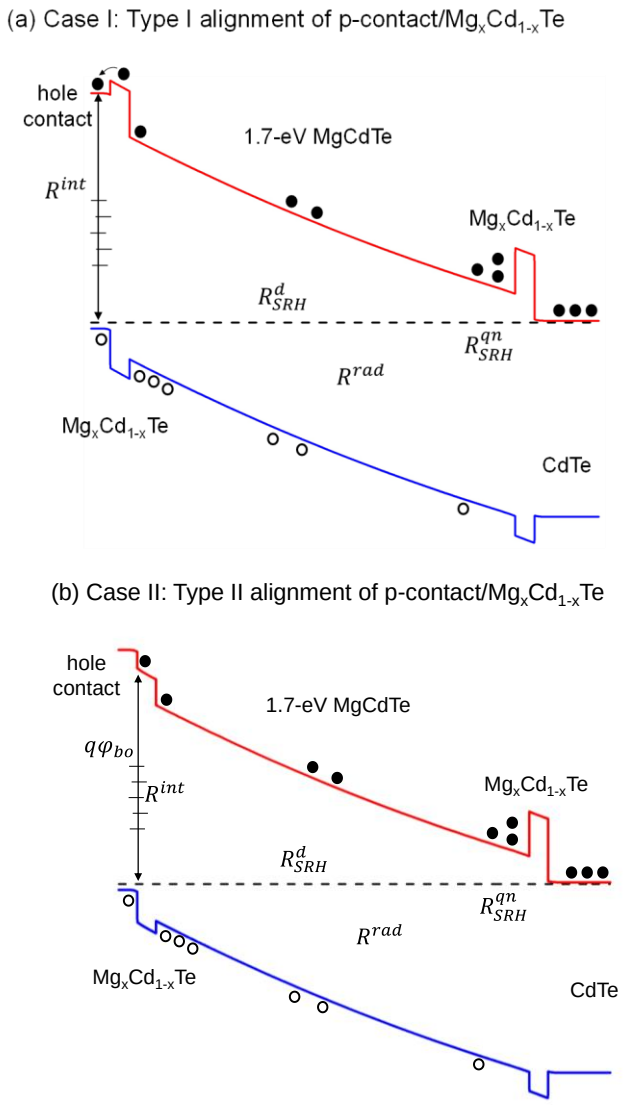

Figure 5.4 Energy band diagram of a 1.7-eV MgCdTe DH solar cell with different recombination processes. (a) Case I: Larger bandgap of i-$Mg_xCd_{1-x}Te$ barriers forms type-I alignment of p-contact/i-$Mg_xCd_{1-x}Te$. (b) Case II: Smaller bandgap of i-$Mg_xCd_{1-x}Te$ barriers forms type-II alignment of p-contact/i-$Mg_xCd_{1-x}Te$. R^{int} represents the effective interface recombination rate either in the a-Si:H hole contact layer (case I) or at the a-Si:H/$Mg_xCd_{1-x}Te$ interface (case II), R^{rad} is the radiative recombination rate in the $Mg_{0.13}Cd_{0.87}Te$ absorber, and R^{d}_{SRH} and R^{qn}_{SRH} are Shockley-Read-Hall (SRH) recombination rates in the depletion region and in the quasi-neutral region, respectively.

$Mg_xCd_{1-x}Te$ barrier layer, and φ_{bo} is the potential barrier for electrons at the interface as labeled in Fig. 5.4 (b). The SRH recombination rates in the depletion region and in the quasi-neutral region are given as:

$$R_{SRH}^{d} = \frac{W_d}{\tau_e+\tau_h} n_i \cdot e^{\frac{qV}{k_BT}} \cong R_0^d e^{\frac{qV}{2k_BT}} \tag{5.2}$$

$$R_{SRH}^{qn} = \frac{W-W_d}{\tau_h} \frac{n_i^2}{N_D} \cdot e^{\frac{qV}{k_BT}} \cong R_0^{qn} e^{\frac{qV}{k_BT}} \tag{5.3}$$

where W and W_d represent the width of the absorber and the depletion region, respectively, and τ_e and τ_h are time constants related to the trap density (N_t) and capture cross-section for electrons (σ_e) and holes (σ_h), with $\tau_e = (N_t \sigma_e \nu_{th})^{-1}$ and $\tau_h = (N_t \sigma_h \nu_{th})^{-1}$. ν_{th} is the average thermal velocity of charge carriers and N_D and n_i are the n-type doping concentration and intrinsic carrier concentration in the absorber, respectively. The radiative recombination rate in the $Mg_{0.13}Cd_{0.87}Te$ absorber is given as:

$$R^{rad} = (1-\gamma) B W n_i^2 \cdot e^{\frac{qV}{k_BT}} \cong R_0^{rad} e^{\frac{qV}{k_BT}} \tag{5.4}$$

where γ is the photon recycling factor[13] and B is the radiative recombination coefficient[15] of the absorber. The photon recycling factor describes the average fraction of radiative recombination generated photons that are reabsorbed within the absorber before escaping the DH.

Under the open-circuit condition, all photogenerated carriers recombine inside the device. The total generation $G_a W$ in the absorber is equal to the total recombination rate ΣR, leading to the following equation:

$$(R_0^{int} + R_0^b + R_0^{rad}) e^{\frac{qV_{oc}}{k_BT}} + R_0^d e^{\frac{qV_{oc}}{2k_BT}} = G_a W \tag{5.5}$$

By solving Eq. (5.5), the V_{OC} is given by:

$$V_{oc} = \frac{2k_BT}{q} ln \left[\frac{1}{2} \frac{R_0^d}{R_0^{int}+R_0^b+R_0^{rad}} \cdot \left(\sqrt{4 G_a W \frac{R_0^{int}+R_0^b+R_0^{rad}}{(R_0^d)^2} + 1} - 1 \right) \right] \tag{5.6}$$

Assuming $4G_aW\frac{R_0^{int}+R_0^b+R_0^{rad}}{\left(R_0^d\right)^2} \gg 1$, which is reasonable based on Eq. (5.5) since the V_{OC} values of these solar cells are higher than 1 V, Eq. (5.6) can be simplified to:

$$V_{oc} = \frac{k_B T}{q} ln\left[\frac{G_a W}{R_0^{int}+R_0^b+R_0^{rad}}\right] \tag{5.7}$$

Since a nearly linear relationship of the V_{OC} with T is observed near room temperature, the activation energy of recombination (E_a) can be obtained using the formula $V_{oc} = \frac{E_a}{q} + T \cdot \frac{dV_{oc}}{dT}$. Therefore, based on Eq. (5.7), E_a can be expressed as:

$$E_a = \begin{cases} \frac{R_0^{int}\varphi_{bo}+(R_0^b+R_0^{rad})E_{g,MgCdTe}}{R_0^{int}+R_0^b+R_0^{rad}} & (case\ I) \\ \frac{R_0^{int}E_{g,a-Si}+(R_0^b+R_0^{rad})E_{g,MgCdTe}}{R_0^{int}+R_0^b+R_0^{rad}} & (case\ II) \end{cases} \tag{5.8}$$

where φ_{bo}, $E_{g,a-Si}$ and $E_{g,MgCdTe}$ are the specific recombination activation energies at the p-contact/i-$Mg_xCd_{1-x}Te$ interface, in the a-Si hole contact, and in the MgCdTe absorber/quasi-neutral region, respectively. From this point of view, the recombination activation energy, E_a, is the average activation energy of the different recombination processes weighted by their respective recombination rates at equilibrium.

The V_{OC} measurements of the four devices at different temperatures are shown in Fig. 5.5. In the temperature range 250 to 300 K it is reasonable to assume that the bandgap energy and the carrier lifetimes do not change much with temperature, as observed in CdTe/MgCdTe DHs [11,15]. The V_{OC} therefore increases almost linearly as the temperature decreases due to the increased quasi-Fermi level splitting for electrons and holes under illumination at lower temperatures, as shown in Eq. (5.9),

$$qV_{oc} = E_g - (E_c - E_{Fn}) - \left(E_{Fp} - E_V\right) \approx E_g - kTln\left(\frac{N_C N_V}{G\tau(G\tau+N_D)}\right) \tag{5.9}$$

The activation energy can be obtained from extrapolating the linear fitting of the V_{OC} near room temperature to 0 K. The devices with different $Mg_xCd_{1-x}Te$ barriers (structures A, B and C) share a nearly identical activation energy of 1.89 V while the device with lower $Mg_xCd_{1-x}Te$ barrier height (structure D) demonstrates an activation energy of 1.76 V. This characteristic can be explained by the following band edge alignment analysis and the formalism of the various recombination processes described above.

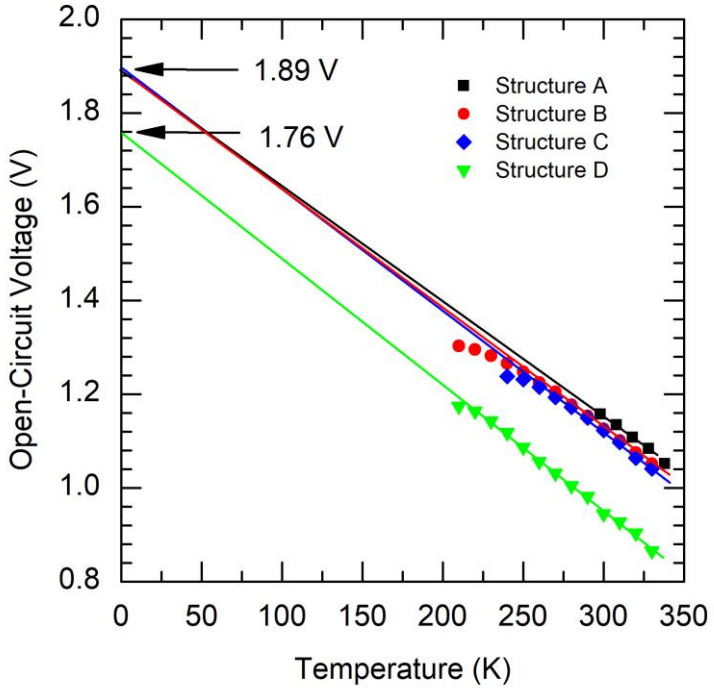

Figure 5.5 Temperature-dependent V_{OC} measurements of 1.7-eV MgCdTe DH solar cells with structures A, B, C and D. The activation energies are obtained from the linear fitting of V_{OC} near room temperature and extrapolating the fitting to 0 K.

5.3 Loss Mechanism Analysis

Schematics of the band alignment of the solar cell structures based on Anderson's rule are shown in Fig. 5.6. The electron affinity [110,111] and bandgap [8,112] of a-Si:H,

$Mg_xCd_{1-x}Te$ barriers, and the $Mg_{0.13}Cd_{0.87}Te$ absorber are summarized in Table 5.3. Fig. 5.6 (a) and Fig. 5.6 (b) represent MgCdTe devices with 2.4-eV and 2.2-eV $Mg_xCd_{1-x}Te$ barriers, respectively. For both 2.4-eV and 2.2-eV $Mg_xCd_{1-x}Te$ barriers, the band alignment with the a-Si:H layer is type-I, i.e. the conduction band edge of the $Mg_xCd_{1-x}Te$ barriers is higher than that of the a-Si:H while their valence band edge is lower than that of the a-Si:H layer. In such a band structure, the transition time of free electrons in the conduction band from the $Mg_xCd_{1-x}Te$ barrier to the a-Si:H hole contact is much shorter than that of recombination processes in the bulk or at the interface. Therefore in the MgCdTe devices with structures A – C, photogenerated electrons in the $Mg_xCd_{1-x}Te$ top barrier would first transfer to the conduction band of a-Si:H with lower energy states and then recombine in the a-Si:H layer through thermionic emission, as described in Fig. 5.6 (a) and 5.6 (b). Previous study of the CdTe/MgCdTe DHs has also confirmed that surface recombination outside the DHs by electron thermionic emission overcoming the MgCdTe barrier is the major recombination mechanism [17]. The nearly identical activation energies of structures A - C are thus attributed to the bandgap of the a-Si:H, which is independent of the $Mg_xCd_{1-x}Te$ barriers. These activation energies also indicate that the majority of recombination in the MgCdTe devices occurs in the a-Si:H layer, outside the DHs.

Fig. 5.6 (c) depicts a MgCdTe device with 2.0-eV $Mg_xCd_{1-x}Te$ barriers. In this band structure, both the conduction band edge and valence band edge of the $Mg_xCd_{1-x}Te$ top barrier are lower than the corresponding band edges of the p-type a-Si:H layer, which has type-II algnment. Therefore, most of the photogenerated electrons in the 2.0-eV $Mg_xCd_{1-x}Te$ top barrier recombine with holes at the p-type a-Si:H/i-$Mg_xCd_{1-x}Te$ interface, instead of transferring to the conduction band of the a-Si:H layer. This process is shown in Fig. 5.6

(c). The activation energy of this device with 2.0-eV $Mg_xCd_{1-x}Te$ barriers (structure D) is 1.76 V, which is very close to the energy gap from the conduction band edge of the $Mg_xCd_{1-x}Te$ top barrier to the valence band edge of the a-Si:H layer based on the band edge alignment. Therefore, the E_a extracted from the V_{OC} measurements suggests the majority of recombination in the device with 2.0-eV $Mg_xCd_{1-x}Te$ barriers occurs at the p-type a-Si:H/i-$Mg_xCd_{1-x}Te$ interface. Overall, due to the high quality $Mg_{0.13}Cd_{0.87}Te$ absorber and

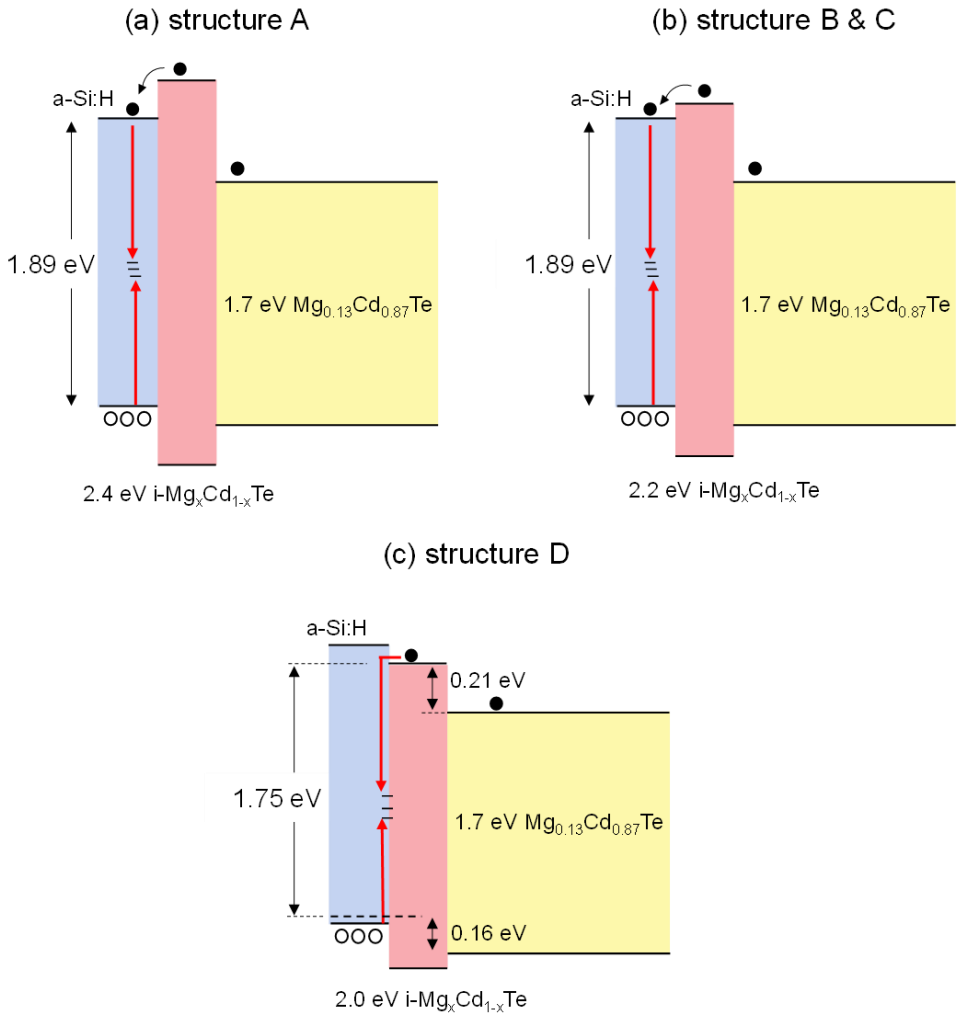

Figure 5.6 Schematic band alignment of 1.7-eV MgCdTe DH solar cells with (a) structure A (2.4-eV $Mg_{0.5}Cd_{0.5}Te$ barriers), (b) structure B and C (2.2-eV $Mg_{0.37}Cd_{0.63}Te$ barriers) and (c) structure D (2.0-eV $Mg_{0.28}Cd_{0.72}Te$ barriers). The major interface recombination mechanisms are illustrated using red arrows, with corresponding recombination activation energies.

i-$Mg_xCd_{1-x}Te$/i-$Mg_{0.13}Cd_{0.87}Te$ interface, the majority of recombination occurs outside the MgCdTe DHs in the four device types. This finding suggests a wider bandgap $Mg_xCd_{1-x}Te$ top barrier would effectively prevent the extra carriers from reaching the defective hole contact layer to recombine non-radiatively.

TABLE 5.3 Electron affinity and bandgap of each layer in the MgCdTe DH solar cells.

Material	Electron affinity (eV)	Bandgap (eV)
a-Si:H	3.90	1.89
$Mg_{0.28}Cd_{0.72}Te$	3.94	2.01
$Mg_{0.37}Cd_{0.63}Te$	3.80	2.18
$Mg_{0.5}Cd_{0.5}Te$	3.66	2.43
$Mg_{0.13}Cd_{0.87}Te$	4.15	1.74

To analyze the loss of the photocurrent in structure C, the reflectance and absorptance spectrum of each layer is calculated using the transfer matrix method and is presented in Fig. 5.7. The absorptance of the $Mg_{0.13}Cd_{0.87}Te$ absorber layer closely resembles the measured EQE, indicating that the carrier collection efficiency in the solar cell is close to unity. In the simulated result, the light absorbed outside the absorber is assumed to be lost to non-radiative recombination. The i-$Mg_xCd_{1-x}Te$ top barrier and the p-type a-Si:H layer contribute 2.4 mA/cm^2 and 1.3 mA/cm^2 J_{SC} loss, respectively. A wider bandgap p-type hole contact and $Mg_xCd_{1-x}Te$ top barrier layer are needed to reduce the parasitic absorption and further improve the J_{SC} of the MgCdTe devices. Based on the discussion above, a wider bandgap of $Mg_xCd_{1-x}Te$ top barrier is proposed to enhance both the J_{SC} and V_{OC} of the devices.

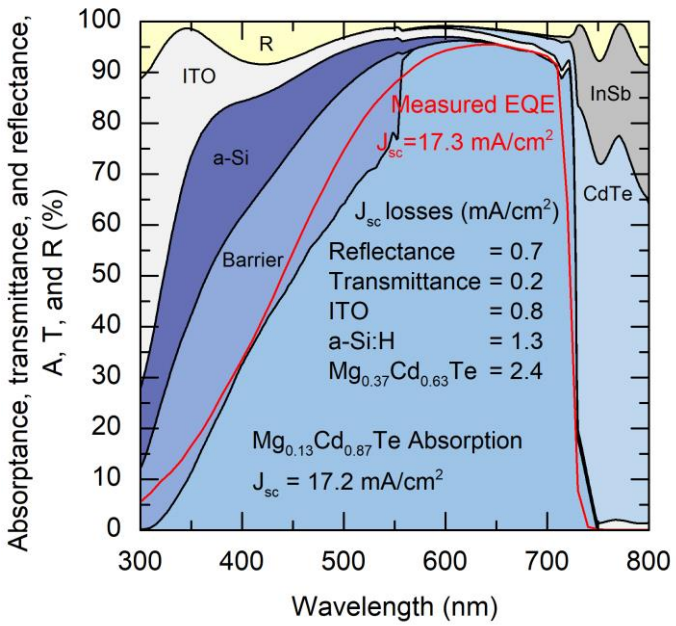

Figure 5.7 Calculated absorptance, transmittance, and reflectance spectra of a $Mg_{0.13}Cd_{0.87}Te/Mg_{0.37}Cd_{0.63}Te$ DH solar cell, with measured EQE curve. The J_{SC} losses consist of the reflectance (R) and the absorptance of each layer except 1.7-eV $Mg_{0.13}Cd_{0.87}Te$ absorber. The transmittance is attributed to the absorption of CdTe buffer layer and InSb substrate.

In summary, a set of monocrystalline 1.7-eV MgCdTe DH solar cells with varying $Mg_xCd_{1-x}Te$ barrier heights has been demonstrated, among which a peak active-area efficiency of 15.2% is measured. The $Mg_xCd_{1-x}Te$ top barrier in the DH plays an important role by confining the electrons from the absorber and enabling the high V_{OC} of the devices. The differing activation energies of the four structures reveal that the dominant recombination loss happens through electron thermionic emission in the a-Si:H layer or at the interface of the a-Si:H hole contact and $Mg_xCd_{1-x}Te$ top barrier, determined by the $Mg_xCd_{1-x}Te$ barrier height. Considering the 70:30 band offset ratio of the conduction and valence bands in MgCdTe [8], a $Mg_xCd_{1-x}Te$ bottom barrier with lower Mg composition will enhance the electron transport and increase the *FF* of the device. As demonstrated by the photocurrent loss analysis, the use of a larger-bandgap hole contact layer and a wider-

bandgap $Mg_xCd_{1-x}Te$ top barrier can further reduce the parasitic light absorption and increase the J_{SC}.

CHAPTER 6

PROTON RADIATION STUDY FOR SPACE APPLICATIONS

6.1 Introduction

High-efficiency, light-weight and radiation-hard solar cells are highly desirable for space applications, especially the LEO satellites, which need even lower-cost components with acceptable performance due to their vast demand volume, on the order of many thousands of satellites. The demand of solar panels on other satellites will also become stronger due to the increasing interest and rapid innovation in electric propulsion, which offers higher specific impulse, reduces costs and enables new types of missions. For the CdTe material, a water-soluble lift-off technology for CdTe using MgTe sacrificial layer and monocrystalline 1.7-eV MgCdTe DH solar cells with an active area power conversion efficiency over 15% are developed and demonstrated in Chapter 5 and Chapter 6, respectively. The combination of these two technologies is expected to deliver high-performance CdTe thin-film solar cells and MgCdTe/Si or MgCdTe/CIGS tandem solar cells with high-efficiency, high power density and much improved radiation hardness. Compared to the III-V devices, this approach and II-VI semiconductors have several advantages:

i) II-VI materials, especially CdTe, show better performance than the traditional III-V materials in terms of radiation hardness and radiation damage recovery through room temperature annealing [113,114]. When efficiency of III-V and Si solar cells decreased to 60% ~ 90% of the pre-irradiation value under the displacement damage dose of 5×10^{10} MeV/g, the efficiency of CdTe solar cells even slightly increased, which exhibits a superior radiation hardness of the CdTe solar cells over the other III-V and Si cells [104].

ii) CdTe single-junction solar cells have a similar theoretical limit of power conversion efficiency as that of GaAs counterpart but much smaller degradation under radiation.

iii) Since the newly invented water-soluble lift-off process only uses water to etch away the MgTe sacrificial layer, the InSb substrate is intact and can be reused indefinitely, a substantial reduction of manufacturing cost. Commercial vendors have already demonstrated the scalability of InSb substrates up to 6 inch in diameter, enabling the high throughput and much reduced processing cost.

The fundamental material physics for the difference in the radiation hardness between II-VI, and III-V and Si is because many defects in ionic materials, such as II-VI semiconductors, result in discrete energy levels in the conduction or the valence band, while the energy levels of the defects in covalent semiconductors, such as III-V and Si, are mainly in the middle of the forbidden gap and act as SRH non-recombination centers, which degrade the performance of minority carrier devices such as solar cells and photodetectors. Such behaviors have been also observed and confirmed in II-VI HgCdTe photodetectors and CdTe solar cells, both of which exhibit superior radiation hardness than conventional III-V or Si devices. The CdTe solar cells with rapid recovery through annealing can maintain the efficiency under radiation of ~ 1 MeV protons up to 10^{12} cm^{-2} fluence [115]. $Cd_{0.9}Zn_{0.1}Te$ shows even higher stability than CdTe [116].

In this chapter, the optical performance of the monocrystalline CdTe DHs under proton irradiation are demonstrated and analyzed.

6.2 Characterization of CdTe DHs After Proton Irradiation

The conventional CdTe DH, which is shown in Fig. 6.1, are bombarded with stepwise 63-MeV-protons at different fluence of 1.5×10^{11}, 3.75×10^{11}, 7.5×10^{11} and $1.5\text{x}10^{12}$ cm^{-2}, which is equivalent to ionizing dose of 20, 50, 100 and 200 kRad(Si), respectively [117]. The samples are then characterized by using steady-state PL, TRPL and excitation intensity dependent PL. The laser wavelength is 532 nm. Optical density (OD) filters are used in intensity-dependent PL measurements.

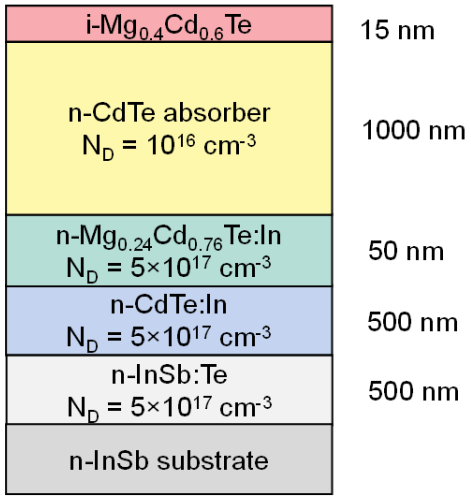

Figure 6.1 Layer structure of the conventional CdTe/MgCdTe DH design for proton radiation test.

Fig. 6.2 shows the steady-state PL and TRPL spectra of a different set of the conventional CdTe/MgCdTe DH samples with proton irradiation at different doses. Compared with the reference sample without irradiation, the samples after proton irradiation at 20, 50 and 100 kRad(Si) show increased PL intensity of 164%, 136%, 114%, and increased PL decay time of 183%, 147%, 109%, respectively; while the sample after 200 kRad(Si) radiation show decreased PL intensity and PL decay time of 12% and 40%, respectively. The PL peak intensity and the PL decay time of the samples are plotted

together with the proton total ionizing dose, as shown in Fig. 6.3. The almost identical trends of the PL peak and the PL decay time indicate that the changes of the optical performance of the CdTe irradiated samples is mainly due to the changes of the minority carrier lifetime. With the increased minority carrier lifetime, the devices based on the CdTe DHs would exhibit a increased V_{OC} and resulted a higher power conversion efficiency, under the 68-MeV proton irradiation below 100 krad(Si). This interesting finding is attributed to the effect of the additional defects generated by proton radiation. When the radiation defect density is relatively low, the increased localization and reduced mobility of photogenerated carriers would hinder the carriers from reaching to Shockley-Read-Hall (SRH) centers to recombine non-radiatively. It is also possibly because the energy levels of some of the radiation defects are inside either the conduction band or the valence band, and thus do not act as SRH centers. Similar effect has been observed in polycrystalline CdTe solar cells [104].

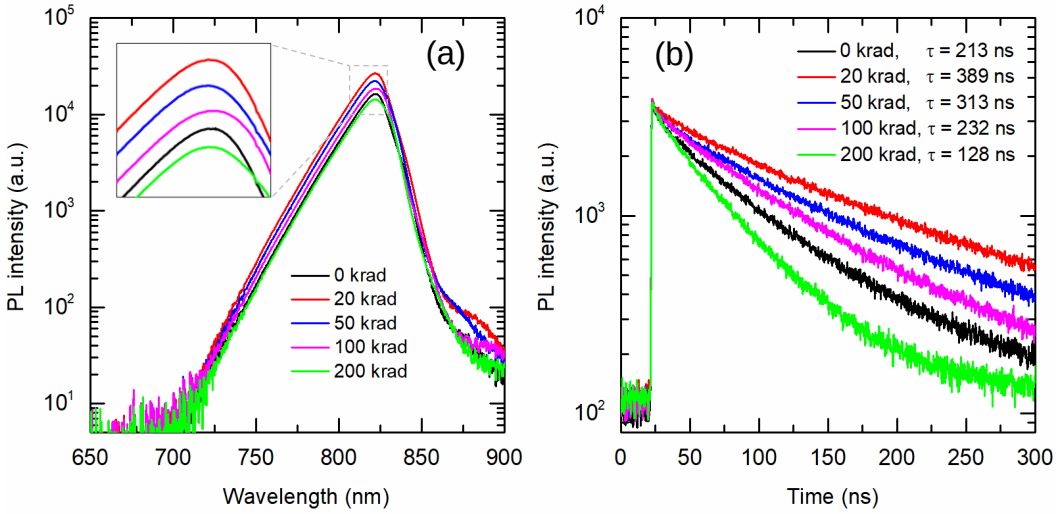

Figure 6.2 (a) Steady-state PL and, (b) TRPL spectra of CdTe/MgCdTe DH samples with proton irradiation at different doses.

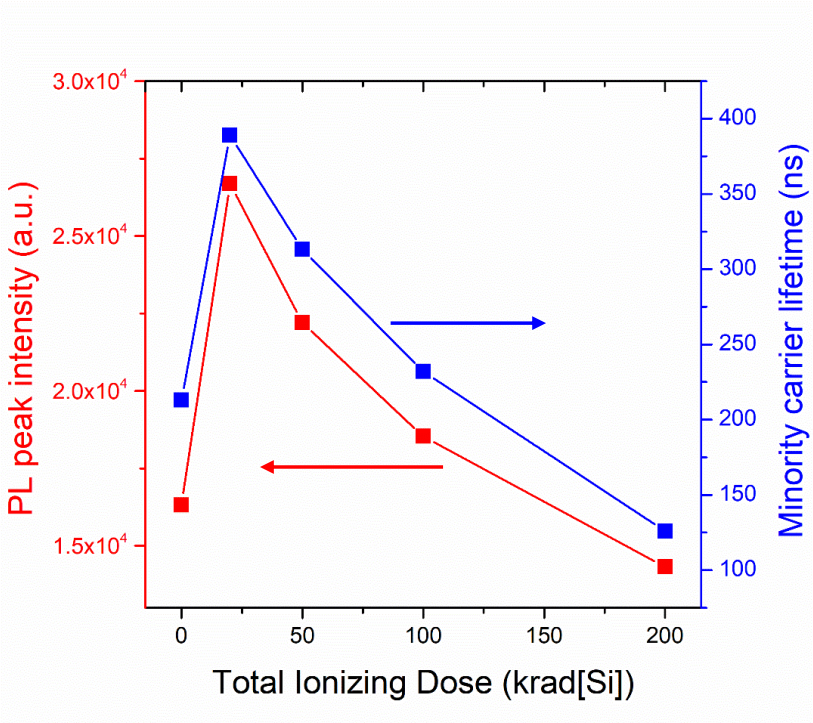

Figure 6.3 PL peak intensity and PL decay time of CdTe/MgCdTe DH samples with proton irradiation at different doses.

Excitation-density-dependent PL measurements are further carried out to study the defects generated by proton irradiation. The PL spectra of CdTe/MgCdTe DH samples with 0, 20 and 200-kRad(Si) proton irradiation are shown in Fig. 6.4 (a), 6.4 (b) and 6.4 (c), respectively. The bandgap emission intensity in the PL spectra increases as the light excitation density increases in all three samples. In addition to the bandgap emission peak, some sub-bandgap peaks are observed in the proton-irradiated samples, while these peaks are not significant in the sample without proton irradiation. In the proton-irradiated samples, the sub-bandgap peaks gradually saturate with the increased excitation density. These behaviors confirm that shallow defects energy levels are introduced by proton radiation. Furthermore, the sub-bandgap peaks move towards a longer wavelength with the increased irradiation dose, indicating that a higher dose of irradiation could cause defects at deeper

energy levels. It is worth pointing out that there is no PL observable beyond 1 μm, indicating there are fewer optically-active deep levels in the CdTe absorber, which is consistent with some theoretical predictions. Our findings have thus further confirmed that the CdTe/MgCdTe DH thin-film solar cells have superior proton radiation hardness and are suitable for space applications.

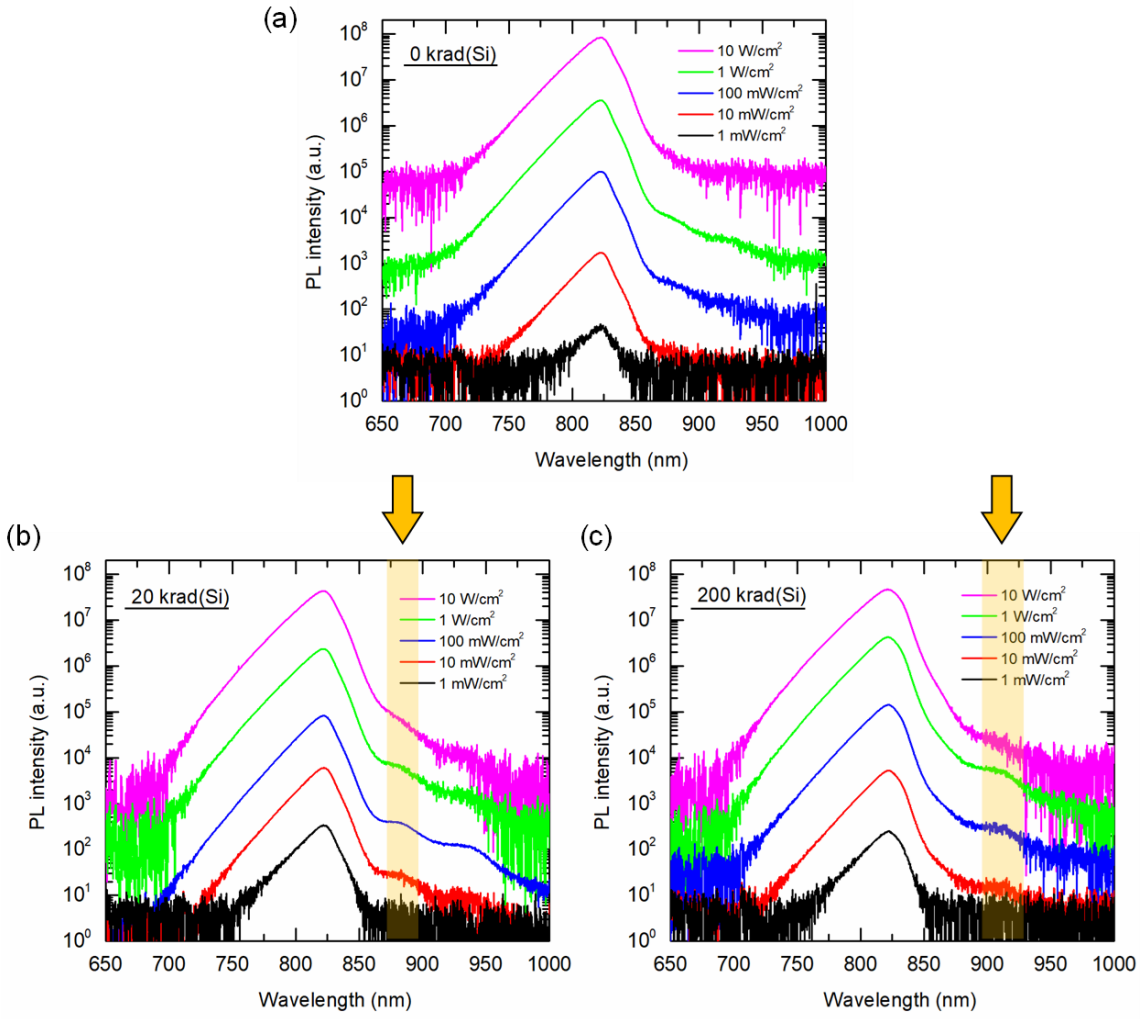

Figure 6.4 Excitation-density-dependent PL spectra of CdTe/MgCdTe DH samples with ionizing dose of (a) 0, (b) 20 and, (c) 200 kRad(Si) proton irradiation.

6.3 Future Work

Even though some hypotheses explain the reason of the better radiation hardness of II-VI materials than III-VI and Si is that many defects in ionic materials result in discrete energy levels in the conduction or the valence band, there's no experimental evidence to support the theory. This is a good opportunity to do the pressure-dependent PL measurements on the proton-irradiated CdTe DH samples.

As shown in Fig. 6.5 schematically, defect states introduced by the proton radiation in the CdTe absorber are typically above the conduction band edge under the atmospheric pressure. Under hydrostatic pressure, the bandgap energy of the CdTe layer increases, while the defect states remain at the same energy and eventually enter the forbidden gap due to their very localized wavefunctions. Then quenching of the PL happens when the defect states in the forbidden gap act as SRH recombination centers. If the assumption is correct, the integrated PL intensity is expected to increase first and then decrease with the pressure. Based on the bandgap change of the CdTe under the pressure, the energy level of

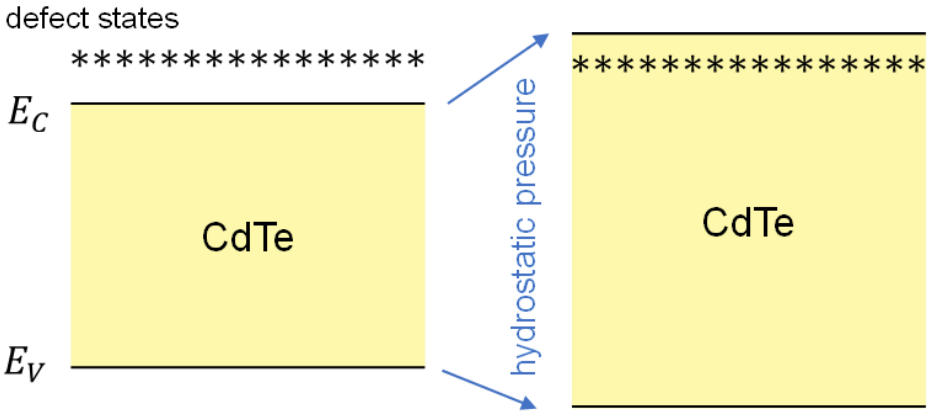

Figure 6.5 A schematic band edge diagram for a CdTe layer showing defect states above the conduction band edge. Under hydrostatic pressure the bandgap energy of the CdTe increases, while the defect states remain at the same energy and enter the forbidden gap, quenching the photoluminescence.

these defect states can also be calculated. Comparing the pressure-dependent PL measurements on the CdTe samples under different proton irradiation doses can further reveal the energy level of the defect states introduced by proton radiation. This experiment will be very informative and allow us to estimate the defect states inside conduction band and to compare that with the theoretical predictions. Similar pressure-dependent PL experiments under hydrostatic pressure up to 2.16 GPa was conducted on a Ga-free InAs/InAsSb type-II superlattice structure [118]. A defect level situated at 0.18 ± 0.01 eV above the conduction band edge of InAs at ambient pressure was detected.

Besides the pressure-dependent PL measurements, the CdTe DH solar cell performance under the proton irradiation can be studied. With the plot of V_{OC}, J_{SC}, FF and efficiency versus proton total ionizing dose, the superior radiation hardness of the CdTe devices can be further confirmed.

CHAPTER 7

CONCLUSION AND OUTLOOK

The monocrystalline CdTe DH solar cells are grown on InSb substrates. The vertical carrier transport across CdTe and InSb heterovalent interface is first studied. The N-CdTe/n-InSb heterojunctions show ohmic behavior with small resistance from the room temperature to 160 K, which is an ideal electron contact for CdTe DH solar cells. The dominated transport process is the electron tunneling through the CdTe barrier. In N-CdTe/p-InSb heterojunctions, the G-R process in the InSb depletion region is the major transport mechanism at lower temperature while the electron tunneling over the CdTe barrier starts to become a factor as temperature increases.

Despite of the "remote junction" design used for the CdTe DH solar cells, which in theory the material quality of the hole contact makes little impact on the device performance, the band edge alignment, lattice mismatch, atomic diffusion, etc. between the hole contact and the monocrystalline CdTe absorber need to be considered seriously in the real applications. For the CdTe DH with a ZnTe:Cu hole contact, the dopant Cu in the hole contact layer would diffuse into the n-type CdTe absorber, suppressing the donor concentration and reduce the V_{bi} and V_{OC}. For ZnTe:As hole contact, some misfit dislocations are generated at the ZnTe/MgCdTe interface due to the lattice mismatch and penetrate into the absorber region, serving as non-radiative recombination centers, shortening the minority carrier lifetime and leading to a low V_{OC}. The C-V, TRPL, PLQE and temperature-dependent V_{OC} measurements can be used to determine the V_{bi}, minority carrier lifetime, iV_{OC} and activation energy of the devices, respectively, which are helpful to diagnose the loss of the V_{OC}.

Besides understanding the CdTe DH solar cells, the applications in thin-film solar cells and tandem solar cells are demonstrated and discussed in this dissertation, enabled by a novel ELO technology for monocrystalline CdTe. By using a nearly lattice-matched and water-soluble MgTe as a sacrificial layer, the intact CdTe DH thin films can be obtained with the enhanced optical performance. A monocrystalline CdTe thin-film solar cell is fabricated with 9.8% power conversion efficiency. The future work is to further optimize the thin-film solar cell structure and demonstrate a CdTe thin-film device with record V_{OC} and efficiency. For tandem application, a monocrystalline 1.7-eV MgCdTe DH solar cell with an active-area efficiency of 15.2% is demonstrated. Based on the loss analysis of the MgCdTe solar cells, the performance of the MgCdTe devices can be further improved by changing the MgCdTe barriers' height and replacing the absorptive a-Si:H hole contact. By incorporating the ELO technology, a tandem solar cell consisting of a MgCdTe top subcell with a 1.7-eV bandgap and a silicon or CIGS bottom subcell with a 1.1-eV bandgap is ready to be developed. The CdTe DHs also show superior proton radiation hardness, indicating the light weight, high-efficiency and high power density monocrystalline CdTe thin-film solar cells are suitable for space applications.

REFERENCES

1. Wilson GM, Al-Jassim M, Metzger WK, Glunz SW, Verlinden P, Xiong G, Mansfield LM, Stanbery BJ, Zhu K, Yan Y, et al (2020) The 2020 photovoltaic technologies roadmap. *J Phys Appl Phys* **53**, 493001.

2. Jäger-Waldau A (2020) Snapshot of Photovoltaics—February 2020. *Energies* **13**, 930.

3. Nelson RJ, Sobers RG (1978) Minority-carrier lifetimes and internal quantum efficiency of surface-free GaAs. *J Appl Phys* **49**, 6103–8.

4. Dawson P, Woodbridge K (1984) Effects of prelayers on minority-carrier lifetime in GaAs/AlGaAs double heterostructures grown by molecular beam epitaxy. *Appl Phys Lett* **45**, 1227–9.

5. Schnitzer I, Yablonovitch E, Caneau C, Gmitter TJ (1993) Ultrahigh spontaneous emission quantum efficiency, 99.7% internally and 72% externally, from AlGaAs/GaAs/AlGaAs double heterostructures. *Appl Phys Lett* **62**, 131–3.

6. Molenkamp LW, van't Blik HFJ (1988) Very low interface recombination velocity in (Al,Ga)As heterostructures grown by organometallic vapor-phase epitaxy. *J Appl Phys* **64**, 4253–6.

7. Ahrenkiel RK, Olson JM, Dunlavy DJ, Keyes BM, Kibbler AE (1990) Recombination velocity of the $Ga_{0.5}In_{0.5}P$/GaAs interface. *J Vac Sci Technol Vac Surf Films* **8**, 3002–5.

8. Kuhn-Heinrich B, Ossau W, Heinke H, Fischer F, Litz T, Waag A, Landwehr G (1993) Optical investigation of confinement and strain effects in CdTe/(CdMg)Te quantum wells. *Appl Phys Lett* **63**, 2932–4.

9. DiNezza MJ, Zhao X-H, Liu S, Kirk AP, Zhang Y-H (2013) Growth, steady-state, and time-resolved photoluminescence study of CdTe/MgCdTe double heterostructures on InSb substrates using molecular beam epitaxy. *Appl Phys Lett* **103**, 193901.

10. DiNezza MJ (2014) Monocrystalline ZnTe/CdTe/MgCdTe Double Heterostructure Solar Cells Grown on InSb Substrates by Molecular Beam Epitaxy. Doctoral dissertation, Arizona State University.

11. Liu S, Zhao X-H, Campbell CM, Lassise MB, Zhao Y, Zhang Y-H (2015) Carrier lifetimes and interface recombination velocities in CdTe/$Mg_xCd_{1-x}Te$ double heterostructures with different Mg compositions grown by molecular beam epitaxy. *Appl Phys Lett* **107**, 041120.

12. Zhao X-H, DiNezza MJ, Liu S, Campbell CM, Zhao Y, Zhang Y-H (2014) Determination of CdTe bulk carrier lifetime and interface recombination velocity of

CdTe/MgCdTe double heterostructures grown by molecular beam epitaxy. *Appl Phys Lett* **105**, 252101.

13. Wang J-B, Ding D, Johnson SR, Yu S-Q, Zhang Y-H (2007) Determination and improvement of spontaneous emission quantum efficiency in GaAs/AlGaAs heterostructures grown by molecular beam epitaxy. *Phys Status Solidi B* **244**, 2740–51.

14. Steiner MA, Geisz JF, García I, Friedman DJ, Duda A, Kurtz SR (2013) Optical enhancement of the open-circuit voltage in high quality GaAs solar cells. *J Appl Phys* **113**, 123109.

15. Zhao X-H, DiNezza MJ, Liu S, Lin S, Zhao Y, Zhang Y-H (2014) Time-resolved and excitation-dependent photoluminescence study of CdTe/MgCdTe double heterostructures grown by molecular beam epitaxy. *J Vac Sci Technol B* **32**, 040601.

16. Zhao X-H, Liu S, Zhao Y, Campbell CM, Lassise MB, Kuo Y-S, Zhang Y-H (2016) Electrical and Optical Properties of n-Type Indium-Doped CdTe/$Mg_{0.46}Cd_{0.54}Te$ Double Heterostructures. *IEEE J Photovolt* **6**, 552–6.

17. Zhao X-H, Liu S, Campbell CM, Yuan Z, Lassise MB, Zhang Y-H (2017) Ultralow Interface Recombination Velocity (∼1 cm/s) at CdTe/MgCdTe Heterointerface. *IEEE J Photovolt* **7**, 913–8.

18. Bicknell RN, Giles NC, Schetzina JF (1986) Growth of high mobility *n*-type CdTe by photoassisted molecular beam epitaxy. *Appl Phys Lett* **49**, 1095–7.

19. Bassani F, Tatarenko S, Saminadayar K, Bleuse J, Magnea N, Pautrat JL (1991) Luminescence characterization of CdTe:In grown by molecular beam epitaxy. *Appl Phys Lett* **58**, 2651–3.

20. Karczewski G, Zakrzewski AK, Dobaczewski L, Dobrowolski W, Grodzicka E, Jaroszyński J, Wojtowicz T, Kossut J (1995) Properties of epitaxially grown CdTe layers doped with indium. *Thin Solid Films* **267**, 79–83.

21. Bassani F, Tatarenko S, Saminadayar K, Magnea N, Cox RT, Tardot A, Grattepain C (1992) Indium doping of CdTe and $Cd_{1-x}Zn_xTe$ by molecular-beam epitaxy: Uniformly and planar-doped layers, quantum wells, and superlattices. *J Appl Phys* **72**, 2927–40.

22. Rau U (2007) Reciprocity relation between photovoltaic quantum efficiency and electroluminescent emission of solar cells. *Phys Rev B* **76**, 085303.

23. Miller OD, Yablonovitch E, Kurtz SR (2012) Strong Internal and External Luminescence as Solar Cells Approach the Shockley–Queisser Limit. *IEEE J Photovolt* **2**, 303–11.

24. Zhao Y, Zhao X-H, Zhang Y-H (2017) Radiative Recombination Dominated Monocrystalline CdTe/MgCdTe Double-Heterostructures. *IEEE J Photovolt* **7**, 690–4.

25. Zhao Y, Boccard M, Liu S, Becker J, Zhao X-H, Campbell CM, Suarez E, Lassise MB, Holman Z, Zhang Y-H (2016) Monocrystalline CdTe solar cells with open-circuit voltage over 1 V and efficiency of 17%. *Nat Energy* **1**, 16067.

26. Becker JJ, Boccard M, Campbell CM, Zhao Y, Lassise M, Holman ZC, Zhang Y-H (2017) Loss Analysis of Monocrystalline CdTe Solar Cells With 20% Active-Area Efficiency. *IEEE J Photovolt* **7**, 900–5.

27. Yang W, Becker J, Liu S, Kuo Y-S, Li J-J, Landini B, Campman K, Zhang Y-H (2014) Ultra-thin GaAs single-junction solar cells integrated with a reflective back scattering layer. *J Appl Phys* **115**, 203105.

28. Becker JJ (2017) Optimization of Monocrystalline $Mg_xCd_{1-x}Te/Mg_yCd_{1-y}Te$ Double-Heterostructure Solar Cells. Doctoral dissertation, Arizona State University.

29. Williams GM, Whitehouse CR, Cullis AG, Chew NG, Blackmore GW (1988) Growth of CdTe-InSb multilayer structures on (100) InSb substrates using molecular beam epitaxy. *Appl Phys Lett* **53**, 1847–9.

30. Li CR, Tanner BK, Ashenford DE, Hogg JHC, Lunn B (1998) The effect of an interfacial layer on the relaxation of CdMnTe/CdTe multiple quantum well structures on InSb substrates. *Semicond Sci Technol* **13**, 746–9.

31. He Z-Y, Campbell CM, Lassise MB, Lin Z-Y, Becker JJ, Zhang Y-H (2019) Monolithically integrated CdTe/InSb visible/midwave-infrared two-color photodetectors. *Infrared Phys Technol* **97**, 58–62.

32. Zheng Y, Chang YH, McCombe BD, Farrow RFC, Temofonte T, Shirland FA (1986) Observation of a quasi-two-dimensional electron gas at an InSb/CdTe interface. *Appl Phys Lett* **49**, 1187–9.

33. Luna E, Trampert A, Lu J, Aoki T, Zhang Y, McCartney MR, Smith DJ (2020) Strategies for Analyzing Noncommon-Atom Heterovalent Interfaces: The Case of CdTe-on-InSb. *Adv Mater Interfaces* **7**, 1901658.

34. Wang X, Campbell C, Zhang Y-H, Nemanich RJ (2018) Band alignment at the CdTe/InSb (001) heterointerface. *J Vac Sci Technol Vac Surf Films* **36**, 031101.

35. Tu D -W, Kahn A (1985) ZnSe– and Se–GaAs interfaces. *J Vac Sci Technol Vac Surf Films* **3**, 922–5.

36. Wilke WG (1988) Valence-band offset and interface formation in ZnTe/GaSb(110) studied by photoemission using synchrotron radiation. *J Vac Sci Technol B Microelectron Nanometer Struct* **6**, 1211.

37. Wilke WG (1989) Valence-band offset and interface chemistry of CdS/InP(110). *J Vac Sci Technol B Microelectron Nanometer Struct* **7**, 807.

38. Yu ET, Phillips MC, Chow DH, Collins DA, Wang MW, McCaldin JO, McGill TC (1992) Interfacial reactions and band offsets in the AlSb/GaSb/ZnTe material system. *Phys Rev B* **46**, 13379–88.

39. Segall B, Lorenz MR, Halsted RE (1963) Electrical Properties of n-Type CdTe. *Phys Rev* **129**, 2471–81.

40. Berus T, Goc J, Nowak M, Oszwałdowski M, Zimpel M (1984) Preparation and electrical properties of InSb thin films heavily doped with tellurium, selenium and sulphur. *Thin Solid Films* **111**, 351–66.

41. Chen JF, Wu MC, Yang L, Cho AY (1990) InAs/AlSb/GaSb single-barrier interband tunneling diodes with high peak-to-valley ratios at room temperature. *J Appl Phys* **68**, 3040–3.

42. Iutzi RM, Fitzgerald EA (2015) Defect and temperature dependence of tunneling in InAs/GaSb heterojunctions. *Appl Phys Lett* **107**, 133504.

43. Sze SM, Ng KK (2007) *Physics of Semiconductor Devices*, 3rd ed, Wiley-Interscience, Hoboken, N.J.

44. Yang QK, Fuchs F, Schmitz J, Pletschen W (2002) Investigation of trap-assisted tunneling current in InAs/(GaIn)Sb superlattice long-wavelength photodiodes. *Appl Phys Lett* **81**, 4757–9.

45. Rosenfeld D, Bahir G (1992) A model for the trap-assisted tunneling mechanism in diffused n-p and implanted n/sup +/-p HgCdTe photodiodes. *IEEE Trans Electron Devices* **39**, 1638–45.

46. Jain SC, McGregor JM, Roulston DJ (1990) Band-gap narrowing in novel III-V semiconductors. *J Appl Phys* **68**, 3747–9.

47. Becker JJ, Campbell CM, Zhao Y, Boccard M, Mohanty D, Lassise M, Suarez E, Bhat I, Holman ZC, Zhang Y-H (2017) Monocrystalline CdTe/MgCdTe Double-Heterostructure Solar Cells With ZnTe Hole Contacts. *IEEE J Photovolt* **7**, 307–12.

48. Ding J, Zhang Y-H (2019) Study of Open-Circuit Voltage in CdTe/MgCdTe Double-Heterostructure Solar Cells with Different Hole Contacts. In: *2019 IEEE 46th Photovoltaic Specialists Conference (PVSC)*, IEEE, Chicago, IL, USA, pp 0021–4.

49. Ying-Shen Kuo, Becker J, Shi Liu, Yuan Zhao, Xin-Hao Zhao, Peng-Yu Su, Bhat I, Yong-Hang Zhang (2015) Monocrystalline ZnTe/CdTe/MgCdTe double heterostructure solar cells grown on InSb substrates. In: *2015 IEEE 42nd Photovoltaic Specialist Conference (PVSC)*, IEEE, New Orleans, LA, pp 1–6.

50. Schroder DK (2006) *Semiconductor Material and Device Characterization*, 3rd edn, John Wiley and Sons, Hoboken, NJ.

51. Su C-H (2008) Energy band gap, intrinsic carrier concentration, and Fermi level of CdTe bulk crystal between 304 and 1067K. *J Appl Phys* **103**, 084903.

52. Duc TM, Hsu C, Faurie JP (1987) Linearity (commutativity and transitivity) of valence-band discontinuity in heterojunctions with Te-based II-VI semiconductors: CdTe, HgTe, and ZnTe. *Phys Rev Lett* **58**, 1127–30.

53. Wei S-H, Zunger A (1987) Role of *d* orbitals in valence-band offsets of common-anion semiconductors. *Phys Rev Lett* **59**, 144–7.

54. Wei S-H, Zunger A (1988) Role of metal *d* states in II-VI semiconductors. *Phys Rev B* **37**, 8958–81.

55. Niles DW, Höchst H, Rioux D (1992) Valence band discontinuity at the ZnTe/CdTe interface: Making ohmic contact to P-type CdTe. In: *AIP Conference Proceedings*, vol 268, AIP, Denver, Colorado (USA), pp 279–84.

56. Continenza A, Massidda S (1994) Electronic properties and valence-band offset of strained ZnTe/CdTe (001) superlattices. *Phys Rev B* **50**, 11949–54.

57. Chen X, Hua X, Hu J, Langlois J-M, Goddard WA (1996) Band structures of II-VI semiconductors using Gaussian basis functions with separable *ab initio* pseudopotentials: Application to prediction of band offsets. *Phys Rev B* **53**, 1377–87.

58. Scheer R (2009) Activation energy of heterojunction diode currents in the limit of interface recombination. *J Appl Phys* **105**, 104505.

59. Grover S, Li JV, Young DL, Stradins P, Branz HM (2013) Reformulation of solar cell physics to facilitate experimental separation of recombination pathways. *Appl Phys Lett* **103**, 093502.

60. Paul S, Grover S, Repins IL, Keyes BM, Contreras MA, Ramanathan K, Noufi R, Zhao Z, Liao F, Li JV (2018) Analysis of Back-Contact Interface Recombination in Thin-Film Solar Cells. *IEEE J Photovolt* **8**, 871–8.

61. Niemegeers A, Burgelman M (1997) Effects of the Au/CdTe back contact on IV and CV characteristics of Au/CdTe/CdS/TCO solar cells. *J Appl Phys* **81**, 2881–6.

62. Demtsu SH, Sites JR (2006) Effect of back-contact barrier on thin-film CdTe solar cells. *Thin Solid Films* **510**, 320–4.

63. Koishiyev GT, Sites JR, Kulkarni, Sachin S, Dhere, Neelkanth G (2008) Determination of back contact barrier height in Cu(ln,Ga)(Se,S)$_2$ and CdTe solar cells. In: *33rd IEEE Photovoltaic Specialists Conference*, , pp 1–3.

64. Woods-Robinson R, Ablekim T, Norman A, Johnston S, Persson KA, Reese MO, Metzger WK, Zakutayev A (2020) Sputtered p-Type $Cu_xZn_{1-x}S$ Back Contact to CdTe Solar Cells. *ACS Appl Energy Mater* **3**, 5427–38.

65. Hall RS, Lamb D, Irvine SJC (2021) Back contacts materials used in thin film CdTe solar cells—A review. *Energy Sci Eng* **9**, 606–32.

66. Li J, Diercks DR, Ohno TR, Warren CW, Lonergan MC, Beach JD, Wolden CA (2015) Controlled activation of ZnTe:Cu contacted CdTe solar cells using rapid thermal processing. *Sol Energy Mater Sol Cells* **133**, 208–15.

67. Metzger WK, Grover S, Lu D, Colegrove E, Moseley J, Perkins CL, Li X, Mallick R, Zhang W, Malik R, et al (2019) Exceeding 20% efficiency with in situ group V doping in polycrystalline CdTe solar cells. *Nat Energy* **4**, 837–45.

68. Burgelman M, Nollet P, Degrave S (2000) Modelling polycrystalline semiconductor solar cells. *Thin Solid Films* **361–362**, 527–32.

69. Tarricone L, Romeo N, Sberveglieri G, Mora S (1982) Electron and hole diffusion length investigation in CdTe thin films by SPV method. *Sol Energy Mater* **7**, 343–50.

70. Thompson CP, Hegedus S, Shafarman W, Desai D (2008) Temperature dependence of V_{OC} in CdTe and Cu(InGa)$(SeS)_2$-based solar cells. In: *2008 33rd IEEE Photovolatic Specialists Conference*, IEEE, San Diego, CA, USA, pp 1–6.

71. Nogay G, Seif JP, Riesen Y, Tomasi A, Jeangros Q, Wyrsch N, Haug F-J, De Wolf S, Ballif C (2016) Nanocrystalline Silicon Carrier Collectors for Silicon Heterojunction Solar Cells and Impact on Low-Temperature Device Characteristics. *IEEE J Photovolt* **6**, 1654–62.

72. Mikolášek M, Racko J, Harmatha L (2017) Analysis of low temperature output parameters for investigation of silicon heterojunction solar cells. *Appl Surf Sci* **395**, 166–71.

73. Brandt RE, Mangan NM, Li JV, Lee YS, Buonassisi T (2017) Determining interface properties limiting open-circuit voltage in heterojunction solar cells. *J Appl Phys* **121**, 185301.

74. Glunz SW, Nekarda J, Mäckel H, Cuevas A (2007) Analyzing back contact of silicon solar cells by suns-Voc-measurements at high illumination densities. In: *22nd European Photovoltaic Solar Energy Conference and Exhibition*.

75. Gunawan O, Gokmen T, Mitzi DB (2014) Suns-V_{OC} characteristics of high performance kesterite solar cells. *J Appl Phys* **116**, 084504.

76. Nayak M, Mudgal S, Singh S, Komarala VK (2020) Investigation of anomalous behaviour in J-V and Suns-Voc characteristics of carrier-selective contact silicon solar cells. *Sol Energy* **201**, 307–13.

77. Konagai M, Sugimoto M, Takahashi K (1978) High efficiency GaAs thin film solar cells by peeled film technology. *J Cryst Growth* **45**, 277–80.

78. Yablonovitch E, Gmitter T, Harbison JP, Bhat R (1987) Extreme selectivity in the lift-off of epitaxial GaAs films. *Appl Phys Lett* **51**, 2222–4.

79. Balocchi A, Curran A, Graham TCM, Bradford C, Prior KA, Warburton RJ (2005) Epitaxial liftoff of ZnSe-based heterostructures using a II-VI release layer. *Appl Phys Lett* **86**, 011915.

80. Tiwari, A N, Krejci, M, Haug, F-J, Zogg, H (1999) 12.8% Efficiency Cu(In,Ga)Se2 solar cell on a flexible polymer sheet. *Prog Photovolt Res Appl* **7**, 393–7.

81. Tiwari AN, Romeo A, Baetzner D, Zogg H (2001) Flexible CdTe solar cells on polymer films. *Prog Photovolt Res Appl* **9**, 211–5.

82. Magginetti DJ, Aguiar JA, Winger JR, Scarpulla MA, Pourshaban E, Yoon HP (2019) Water-Assisted Liftoff of Polycrystalline CdS/CdTe Thin Films Using Heterogeneous Interfacial Engineering. *Adv Mater Interfaces* **6**, 1900300.

83. Fuertes Marrón D, Meeder A, Sadewasser S, Würz R, Kaufmann CA, Glatzel Th, Schedel-Niedrig Th, Lux-Steiner MCh (2005) Lift-off process and rear-side characterization of CuGaSe2 chalcopyrite thin films and solar cells. *J Appl Phys* **97**, 094915.

84. McGott DL, Kempe MD, Glynn S, Bosco N, Barnes TM, Haegel NM, Wolden CA, Reese MO (2018) Thermomechanical Lift-Off and Recontacting of CdTe Solar Cells. *ACS Appl Mater Interfaces* **10**, 44854–61.

85. Jovanovic SM, Devenyi GA, Kuyanov P, Carvalho JL, Meinander K, LaPierre RR, Preston JS (2018) Epitaxial thin film transfer for flexible devices from reusable substrates. *Mater Res Express* **6**, 025913.

86. Seredyński B, Król M, Starzyk P, Mirek R, Ściesiek M, Sobczak K, Borysiuk J, Stephan D, Rousset J-G, Szczytko J, et al (2018) (Cd,Zn,Mg)Te-based microcavity on MgTe sacrificial buffer: Growth, lift-off, and transmission studies of polaritons. *Phys Rev Mater* **2**, 043406.

87. Campbell, C M, Tsai, C-Y, Ding, J, McCarthy, T T, Seredyński, B, Pacuski, W, Zhang, Y-H (2018) Lift-off technology using water soluble MgTe layer for high-efficiency CdTe and MgCdTe solar cells. In: *45th IEEE Photovolt. Spec. Conf.*

88. Campbell CM, Tsai C-Y, Ding J, Zhang Y-H (2019) Epitaxial Lift Off of II-VI Thin Films Using Water-Soluble MgTe. *IEEE J Photovolt* **9**, 1834–8.

89. Green MA (2012) Radiative efficiency of state-of-the-art photovoltaic cells: Radiative efficiency of photovoltaic cells. *Prog Photovolt Res Appl* **20**, 472–6.

90. Yang W, Yang H, Qin G, Ma Z, Berggren J, Hammar M, Soref R, Zhou W (2010) Large-area InP-based crystalline nanomembrane flexible photodetectors. *Appl Phys Lett* **96**, 121107.

91. Cho SJ, Liu D, Seo J-H, Dalmau R, Kim K, Park J, Gong J, Zhao D, Wang F, Yin X, et al (2019) P-type silicon as hole supplier for nitride-based UVC LEDs. *New J Phys* **21**, 023011.

92. Ding D, Johnson SR, Yu S-Q, Wu S-N, Zhang Y-H (2011) A semi-analytical model for semiconductor solar cells. *J Appl Phys* **110**, 123104.

93. Liu S, Ding D, Johnson SR, Zhang Y-H (2012) Optimal optical designs for planar GaAs single-junction solar cells with textured and reflective surfaces. In: *Proc. SPIE, Physics, Simulation, and Photonic Engineering of Photovoltaic Devices*, San Francisco, California, USA, p 82560M.

94. Tanabe K, Watanabe K, Arakawa Y (2012) Flexible thin-film InAs/GaAs quantum dot solar cells. *Appl Phys Lett* **100**, 192102.

95. Plößl A (1999) Wafer direct bonding: tailoring adhesion between brittle materials. *Mater Sci Eng R Rep* **25**, 1–88.

96. Lee K, Shiu K-T, Zimmerman JD, Renshaw CK, Forrest SR (2010) Multiple growths of epitaxial lift-off solar cells from a single InP substrate. *Appl Phys Lett* **97**, 101107.

97. Dharmadasa IM, Samantilleke AP, Chaure NB, Young J (2002) New ways of developing glass/conducting glass/CdS/CdTe/metal thin-film solar cells based on a new model. *Semicond Sci Technol* **17**, 1238–48.

98. Dharmadasa IM, Bunning JD, Samantilleke AP, Shen T (2005) Effects of multi-defects at metal/semiconductor interfaces on electrical properties and their influence on stability and lifetime of thin film solar cells. *Sol Energy Mater Sol Cells* **86**, 373–84.

99. Grassman TJ, Chmielewski DJ, Carnevale SD, Carlin JA, Ringel SA (2016) $GaAs_{0.75}P_{0.25}$/Si Dual-Junction Solar Cells Grown by MBE and MOCVD. *IEEE J Photovolt* **6**, 326–31.

100. Essig S, Allebé C, Remo T, Geisz JF, Steiner MA, Horowitz K, Barraud L, Ward JS, Schnabel M, Descoeudres A, et al (2017) Raising the one-sun conversion efficiency of III–V/Si solar cells to 32.8% for two junctions and 35.9% for three junctions. *Nat Energy* **2**, 17144.

101. Fan S, Yu ZJ, Hool RD, Dhingra P, Weigand W, Kim M, Ratta ED, Li BD, Sun Y, Holman ZC, et al (2020) Current-Matched III–V/Si Epitaxial Tandem Solar Cells with 25.0% Efficiency. *Cell Rep Phys Sci* **1**, 100208.

102. Al-Ashouri A, Köhnen E, Li B, Magomedov A, Hempel H, Caprioglio P, Márquez JA, Morales Vilches AB, Kasparavicius E, Smith JA, et al (2020) Monolithic perovskite/silicon tandem solar cell with >29% efficiency by enhanced hole extraction. *Science* **370**, 1300–9.

103. Horowitz KAW, Fu R, Silverman T, Woodhouse M, Sun X, Alam MA (2017) *An Analysis of the Cost and Performance of Photovoltaic Systems as a Function of Module Area*.

104. Bätzner DL, Romeo A, Terheggen M, Döbeli M, Zogg H, Tiwari AN (2004) Stability aspects in CdTe/CdS solar cells. *Thin Solid Films* **451–452**, 536–43.

105. Adachi S (1999) *Optical Constants of Crystalline and Amorphous Semiconductors*, New York: Springer US.

106. Becker JJ, Campbell CM, Tsai C-Y, Zhao Y, Lassise M, Zhao X-H, Boccard M, Holman ZC, Zhang Y-H (2018) Monocrystalline 1.7-eV-Bandgap MgCdTe Solar Cell With 11.2% Efficiency. *IEEE J Photovolt* **8**, 581–6.

107. Campbell CM, Tsai C-Y, Ding J, McCarthy TT, Seredyński B, Pacuski W, Zhang Y-H (2018) Lift-off technology using water soluble MgTe layer for high-efficiency CdTe and MgCdTe solar cells. In: *45th IEEE Photovoltaics Special Conference (Oral Presentation)*, Hawaii.

108. Ding J, Tsai C-Y, Ju Z, Zhang Y-H (2021) Epitaxial lift-off CdTe/MgCdTe double heterostructures for thin-film and flexible solar cells applications. *Appl Phys Lett* **118**, 181101.

109. Green MA, Emery K, Hishikawa Y, Warta W, Dunlop ED (2015) Solar cell efficiency tables (Version 45): Solar cell efficiency tables. *Prog Photovolt Res Appl* **23**, 1–9.

110. Matsuura H, Okuno T, Okushi H, Tanaka K (1984) Electrical properties of *n* -amorphous/ *p* -crystalline silicon heterojunctions. *J Appl Phys* **55**, 1012–9.

111. Mikolášek M, Jakaboviš J, Řeháček V, Harmatha L, Andok R (2014) Capacitance Analysis of the Structures with the a-Si:H(i)/c-Si(p) Heterojunction for Solar-Cell Applications. *J Electr Eng* **65**, 254–8.

112. Fukutani K, Kanbe M, Futako W, Kaplan B, Kamiya T, Fortmann CM, Shimizu I (1998) Band gap tuning of a-Si:H from 1.55 eV to 2.10 eV by intentionally promoting structural relaxation. *J Non-Cryst Solids* **227–230**, 63–7.

113. Bourgoin JC, de Angelis N (2001) Radiation-induced defects in solar cell materials. *Sol Energy Mater Sol Cells* **66**, 467–77.

114. Lamb DA, Underwood CI, Barrioz V, Gwilliam R, Hall J, Baker MA, Irvine SJC (2017) Proton irradiation of CdTe thin film photovoltaics deposited on cerium-doped space glass. *Prog Photovolt Res Appl* **25**, 1059–67.

115. Batzner DL, Romeo A, Dobeli M, Weinert K, Zogg H, Tiwari AN (2002) High energy irradiation properties of CdTe/CdS solar cells. In: *Conference Record of the Twenty-Ninth IEEE Photovoltaic Specialists Conference, 2002.*, IEEE, New Orleans, LA, USA, pp 982–5.

116. Fraboni B, Cavallini A, Dusi W (2004) Damage induced by ionizing radiation on CdZnTe and CdTe detectors. *IEEE Trans Nucl Sci* **51**, 1209–15.

117. Ding J, Webster PT, Qi X, Zhao Y, Zhang Y-H (2021) Epitaxial lift-off monocrystalline CdTe/MgCdTe double heterostructures and proton radiation study for space applications. In: *2021 IEEE 48th Photovoltaic Specialists Conference (PVSC)*, IEEE, Fort Lauderdale, FL, USA, pp 1213–6.

118. Prins AD, Lewis MK, Bushell ZL, Sweeney SJ, Liu S, Zhang Y-H (2015) Evidence for a defect level above the conduction band edge of InAs/InAsSb type-II superlattices for applications in efficient infrared photodetectors. *Appl Phys Lett* **106**, 171111.